75-21,327

GROSSMAN, Mark William, 1945-
EXPERIMENTAL STUDY OF RUNAWAY ELECTRONS AND PLASMA RESISTIVITY IN A PLASMA BETATRON.

The City University of New York, Ph.D., 1975
Physics, plasma

Xerox University Microfilms, Ann Arbor, Michigan 48106

EXPERIMENTAL STUDY OF RUNAWAY ELECTRONS AND PLASMA RESISTIVITY IN A PLASMA BETATRON

by

MARK WILLIAM GROSSMAN

A dissertation submitted to the Graduate Faculty in Physics in partial fulfillment of the requirements for the degree of Doctor of Philosophy, The City University of New York.

1975

This manuscript has been read and accepted for the Graduate Faculty in Physics in satisfaction of the dissertation requirement for the degree of Doctor of Philosophy.

5/15/75
date

L. G. Ferrari
Chairman of Examining Committee

5/19/75
date

Myriam P. Sarachik
Executive Officer

M. S. Zucker
Robert A. Main
Roy Rosenfeld
Supervisory Committee

The City University of New York

Abstract

EXPERIMENTAL STUDY OF RUNAWAY ELECTRONS AND PLASMA RESISTIVITY IN A PLASMA BETATRON

by

Mark W. Grossman

Advisor: Professor Lawrence A. Ferrari

A plasma betatron has been constructed to study runaway electrons and plasma electrical resistivity in a magnetized toroidal plasma. The 40KHz betatron induction field has a maximum amplitude which can be varied from 1.5v/cm to 12.5v/cm. The azimuthal magnetic field has an amplitude in the range of 300 gauss to 2000 gauss and is essentially constant during the time of plasma formation and application of the betatron field.

Argon and hydrogen discharges are formed with the use of a small co-axial plasma gun. The plasma gun was developed for use in the betatron. In both types of plasmas the typical temperature and density are 15ev and $8 \times 10^{12} cc^{-1}$ respectively. Discharges with current maxima as high as 2.5 kiloamps and as low as 5×10^{-2} kiloamps (for the same cycle of the betatron field) have been studied in hydrogen

discharges. The current range in argon discharges is restricted to values of around 1 kiloamp for rapid plasma formation.

Energetic X-rays, 75 Kev, are observed before the end of the initial acceleration cycle in hydrogen and argon plasmas. At low enough currents in hydrogen, energetic X-rays appear at every cycle. The calculated energy of freely accelerated electrons, so called runaways, would be 79 Kev. Thus the energetic X-rays are Bremstrellung emitted by runaways hitting the vacuum chamber wall. To within the experimental error, the X-ray emission time depends inversely on the maximum electric field strength and is independent of the azimuthal magnetic field strength. This corresponds to a, so called, resistive instability in which the equilibrium orbit of the runaways is displaced into the vacuum chamber wall due to the presence of a large conduction current. When X-rays are not detected the equilibrium orbit lies initially out of the vacuum chamber. Calculations show that when this is the case, the runaways reach the vacuum chamber wall with energies of about 2 Kev. The X-rays which are emitted by these runaways are too low in energy to be detected with our X-ray equipment.

The measured plasma conductivity in hydrogen and argon is about 100 times smaller than predicted by the Fokker-Planck $T^{3/2}$ law (T is the electron plasma temperature). It is shown that this anomolous conductivity may be due to the growth of ion acoustic waves with wavenumbers less than an inverse Debye length. The plasma conduction current has, typically, a non-linear form, which becomes more non-linear as the conduction current is lowered. Different computer models were developed to try to predict the current amplitude, current column size, plasma temperature, phase between the electric field and current, and the overall non-linear wave form. For large currents, where the wave forms are near linear in appearance, a linear circuit model of the plasma betatron gave good quantitative estimates for the plasma temperature and column size corresponding to measured phase difference and current amplitude. A non-linear circuit model using a phenomenological time dependent plasma resistance term, qualitatively predicts the observed non-linear current forms.

Ionization rates by runaways were studied by the direct summation of the number of electrons produced in an ionizing cascade. Also, certain parametric relations among the external fields and the total runaway current are found.

ACKNOWLEDGEMENTS

I would like to thank my advisor, Professor Lawrence A. Ferrari, for suggesting this research topic and helping me with the various aspects of the thesis research. His guidance is most appreciated. Also the following individuals helped make the completion of this thesis possible: Paul Schaedler and Charles Spiteri who constructed some of the major components of the plasma betatron, Walter Koch and Charles Fries who facilitated the purchasing of equipment and Edward Kuhner who helped in the construction of some of the diagnostic equipment.

Finally, my wife, Amy, deserves much thanks for the patience and understanding she showed me during the years of my graduate study.

TABLE OF CONTENTS

CHAPTER I

INTRODUCTION

The toroidal magnetic field configuration is one of the classic magnetic field shapes used for fusion research. Experiments related to fusion research such as turbulent heating,[1,2,3] anomolous resistivity,[4,5] and Tokamak experiments[5] utilize toroidal magnetic fields in order to prevent the plasma from coming into contact with the vacuum chamber walls. However, this configuration is inherently a non-equilibrium one due to the fact that the magnetic field pressure will be larger on the inner surface of the toroidal plasma than the outer surface.[7] Also, particle drifts will cause plasma loss. To provide for plasma column stability the toroidal magnetic field must be twisted into a helical configuration. This is accomplished in the Stellarator class of devices by a suitable arrangement of external conductors which provide the helical magnetic field. In Tokamak devices large toroidal currents provide a poloidal field which in addition to the toroidal field results in a helical magnetic field. From the point of view of a single particle, the gradient in the toroidal magnetic field produces a particle drift across the lines into the vacuum chamber walls. The additional

twisting of the magnetic field lines, as measured by the rotational transform, causes the drift motion for a certain portion of the plasma particles to be directed toward the center of the vacuum chamber rather than in a constant vertical direction.

In order to heat the plasma large currents are employed in Tokamak devices. To provide for stable equilibrium of the current column two schemes have been employed. The first method uses good conducting walls surrounding the toroidal vacuum chamber. Image currents produced in these walls provide the needed restoring forces to maintain the current ring within the vacuum chamber. A second equivalent method employs a vertical magnetic field with the proper magnitude and field index for stable equilibrium. For stability in the vertical direction the field index, n, defined by $n = -\frac{\partial \ln B}{\partial \ln R}$ must be greater than 0 and for stability in the horizontal direction the field index must be less than 3/2.[8]

As Tokamak studies have progressed a standard region of stable operation has been established.[9] This region is bounded by a maximum and minimum toroidal current region and an upper and lower plasma density region. The first three regions are related to the Kruskal-Shafranov limit. This limit defines the maximum possible toroidal current for a given toroidal magnetic field.

Beyond this maximum the plasma column becomes kink unstable. To avoid this limit the q-factor must be greater than 1. This factor is the ratio of the toroidal minor diameter to the toroidal major diameter times the ratio of the toroidal field to the poloidal field. At the lower plasma density limit very energetic electrons are produced. These runaway electrons carry most of the longitudinal current. Associated with the runaway electrons is a disruptive instablity which may be related to the runaway electron production.

The experimental device employed in this study resembles a Tokamak. It has been designed to provide suitable conditions for plasma confinement and production of runaway electrons. A Pyrex toroidal vacuum chamber is used and conducting coils encircle the vacuum chamber minor circumference in order to provide the toroidal magnetic field. Pairs of co-axial conducting loops whose planes are parallel to the toroidal plane are located above and below the toroidal plane. These loops produce a betatron-type field. The induced voltage is in the toroidal direction while the associated vertical magnetic field provides stable equilibrium orbits for freely accelerated electrons. The position of the coils is adjusted as is the coil current distribution so that the betatron equilibrium condition is satisfied and so that

the field index is between 0 and 1 over a large portion of the vacuum chamber. The basic difference between the plasma betatron and the Tokamak is that in Tokamaks the vertical stabilizing field and the toroidal ohmic heating electric field are independent of each other while in the plasma betatron they are not independent. The Tokamak fields are designed to stablize the conduction current column while the betatron is designed to stablize the runaway current in phase with the betatron magnetic field.

The "classical" plasma resistivity found from an analysis of the Fokker-Planck equations yields the well known $T^{-3/2}$ formula.[10] This formula has been used to predict electron plasma temperatures from measured resistivity. Experimental and theoretical studies[11,12,13] have shown that for large enough electric fields applied to the plasma, the plasma resistivity can be much higher than predicted by the $T^{-3/2}$ Fokker-Planck formula.[14,15] In addition other experimental conditions give[16,17] resistivity values which do not follow the $T^{-3/2}$ law. This anomolous resistivity is caused by the enhanced scattering of electrons from excited plasma waves produced in an unstable plasma. Our experimental studies suggest the existence of anomolous resistivity under certain experimental conditions due to the existence of ion acoustic waves. Some aspects of the experimental resistivity

results agree with known theoretical results.

Runaway electrons can be produced when a large enough electric field is applied to the plasma. Above a critical electric field strength the plasma resistance is drastically reduced due to the inverse velocity cubed dependence of the electron Coulomb collision frequency. In this regime the Fokker-Planck equation is no longer obeyed since the dynamical friction does not balance the electric force. The critical field, E_c, needed for this runaway condition is proportional to the ratio of plasma density to electron plasma temperature, that is, $E_c \cong 10^{-12} \frac{n_{ec}}{T_{ev}}$. Due to Joule heating, electric fields much less than the critical field may eventually produce runaway electrons.

Previous runaway electron experiments have shown the disruption of the runaway beam before the end of the acceleration cycle even though the vacuum fields should have provided for stable equilibrium orbits. In our study of runaway electrons we have observed a particular dependence of runaway disruption time on experimental parameters. This dependence has not been previously reported.

In summary, this study deals with an experimental investigation of plasma resistivity and runaway electron production in a low beta toroidal plasma. The major

experimental findings are discussed within the framework of existing theories and with respect to previous experimental results. Certain experimental data are expressed and discussed in terms of typical Tokamak fusion reactor parameters. Chapter II discusses the theories which are relevent to this experimental study. They include the single particle theory, the guiding center theory, magnetohydrodynamic theory, and kinetic theory. In chapter III a description of the experimental apparatus is given as well as some of the fabrication details. Chapter Iv describes the measurements of the external fields and the results of these measurements. Also a description of the technique used to shape the betatron field is included. Chapter V covers the various plasma diagnostics used and the basic mathematical relations needed for the use of these plasma diagnostics. In some cases a detailed description of the construction of the diagnostic instruments is given. Chapter VI reviews the results of the diagnostic measurements and in chapter VII two theoretical models are developed. The first model deals with ionization by runaway electrons while the second deals with the plasma conduction current. In chapter VIII the measurements are discussed and the principal findings are summarized.

REFERENCES

CHAPTER I

1. S. M. Hamberger and J. Jancarik, The Physics of Fluids 15,825 (1972).
2. S. Q. Mah, H. M. Skarsgard, and A. R. Strilchuk, Physical Review Letters 25, 1409 (1970).
3. A. Hirose,et al., Physical Review Letters 28, 1185 (1972).
4. Ibid.
5. L. A. Ferrari and K. C. Rogers, The Physics of Fluids 10, 1319 (1967).
6. L. A. Artsimovich, Nuclear Fusion 12, 215 (1972)
7. G. Schmidt, Physics of High Temperature Plasmas (Academic Press, New York, 1966).
8. V. S. Mukhovatov and V. D. Shafranov, Nuclear Fusion 11, 605 (1971).
9. United States Atomic Energy Commission, Status and Objectives of Tokamak Systems For Fusion Research, Wash-1295,UC-20(Washington, D. C.:Government Printing Office).
10. L. Spitzer Jr., Physics of Fully Ionized Gases, Second Edition (Interscience, New York, 1962).

11. S. M. Hamberger and M. Friedman, Physical Review Letters 21, 674 (1968).

12. B. A. Demidov, et al., Soviet Physics-Doklady 12, 467 (1967).

13. J. E. Robin and M. R. MacKenzie, The Physics of Fluids 14, 1171 (1971).

14. S. Q. Mah, et al., Physical Review Letters 25, 1409 (1970).

15. O. Buneman, Physical Review 115, 503 (1959).

16. B Coppi and E. Mazzucato, The Physics of Fluids 14, 139 (1971).

17. B. Coppi, Physical Review Letters 32, 530 (1974).

CHAPTER II

THEORY

In this chapter different descriptions of the plasma state will be applied to the phenomena relevent to this study. In particular, the single particle theory and guiding center theory are used to predict runaway electron orbits in the plasma betatron. The guiding center theory is also used to discuss particle trapping. A one component fluid theory is used to discuss plasma stability and some reference is made to parameters important in Tokamak stability. The Vlasov equation, i. e., kinetic theory, is used to derive the ion acoustic wave dispersion relation and growth rates. In a more general way kinetic theory is used to describe previous results of theoretical and experimental investigations of plasma resistivity. In chapter VII a two-component plasma is studied by taking moments of the Fokker-Planck equation for ions and the Fokker-Planck equation for electrons.

Consider the motion of a single charged particle in a combined betatron magnetic field $(B_R, 0, B_z)$ and azimuthal field $(0, B_\phi, 0)$ as shown in figure 1.[1,2] Both fields are cylinderically symmetric and symmetric with respect to the

$Z=0$ plane, or median plane. The particle motion is considered in a region in which the sources of these fields are absent so that the relevent Maxwell's equations are:

$$\nabla \times \underset{\sim}{B} = 0$$
$$\nabla \cdot \underset{\sim}{B} = 0$$

The non-relativistic equations of motion are

$$\ddot{R} - \frac{v_\phi^2}{R} - \frac{e}{mc} v_\phi B_z = -\frac{e}{mc} \dot{z} B_\phi$$
$$\ddot{z} + \frac{e}{mc} v_\phi B_R = \frac{e}{mc} \dot{R} B_\phi$$
$$v_\phi \equiv R\dot{\phi}$$

where a dot indicates differentiation with respect to time, m is the mass of the particle, c is the speed of light. At $z=0$ and $R=R_0$ B_z satisfies the equilibrium equation:

$$\frac{m v_\phi^2}{R_0} = -\frac{e}{c} v_\phi B_{z0}$$

These equations are relativistically correct when m is the relativistic mass and one considers small energy per turn gains. Let $x = R - R_0$. We expand the components of the magnetic field about the points $z=0$ and $x=0$:

$$B_R = B_{R_0} + \frac{\partial B_R}{\partial x}\Big)_0 x + \frac{\partial B_R}{\partial z}\Big)_0 z$$
$$B_\phi = B_{\phi 0} + \frac{\partial B_\phi}{\partial x}\Big)_0 x + \frac{\partial B_\phi}{\partial z}\Big)_0 z$$
$$B_z = B_{z0} + \frac{\partial B_z}{\partial x}\Big)_0 x + \frac{\partial B_z}{\partial z}\Big)_0 z$$

Using Maxwell's equations and symmetry conditions we have

$$B_R = \frac{\partial B_z}{\partial x}\Big)_0 x + \frac{\partial B_z}{\partial x}\Big)_0 z$$
$$B_\phi = B_{\phi 0} - \frac{B_{\phi 0}}{R_0} x$$
$$B_z = B_{z0} + \frac{\partial B_z}{\partial x}\Big)_0 z$$

Using the following definitions

$$n = -\frac{R_0}{B_{z0}} \cdot \frac{\partial B_z}{\partial x}\Big|_0 \qquad \text{Field Index}$$

$$\omega_0 = \frac{eB_{z0}}{mc}$$

$$\omega_c = \frac{eB_{\phi 0}}{mc} \qquad \text{Cyclotron Frequencies}$$

we may write the external fields and the equations of motion near the $z=0$, $R=R_0$ region as follows:

$$B_R = -\frac{n}{R} B_{z0} z$$

$$B_z = B_{z0}\left(\frac{R_0}{R}\right)^n$$

It is noted that Ampere's law is not satisfied by the betatron fields in the approximation used, but the form is a good approximation.

$$B_\phi = B_{\phi 0}\frac{R_0}{R}$$

$$\ddot{x} + \omega_0^2 x(1-n) = -\omega_c \dot{z}$$

$$\ddot{z} + n z \omega_0^2 = \omega_c \dot{x}$$

Assuming solutions to these equations of motion of the form $Ke^{i\omega t}$, the two possible values of ω are

$$\left(\frac{\omega}{\omega_0}\right)^2 = \frac{1}{2}\left\{1 + \frac{\omega_c^2}{\omega_0^2} \pm \sqrt{\left(1+\frac{\omega_c^2}{\omega_0^2}\right) + 4n(n-1)}\right\}$$

We see from the linearized equations of motion that the B_ϕ field has the effect of coupling motion in the x and z directions. For strong enough values of B_ϕ the motion about the equilibrium position ($z=0$, $R=R_0$) is composed of a rapid gyration about the guiding center superimposed on a slower elliptical drift of the guiding center as shown in figure 2. The ratio of the length of the major axis to the length of the minor axis is $\sqrt{\frac{n}{1-n}}$. We note that the solutions to the equations of motion are harmonic if n satisfies the condition $0 < n < 1$.

Whether the orbit of an electron is stable or not can be investigated by considering the equation of motion expressed in terms of the vector potential $\underset{\sim}{A}(A_r, A_\phi, A_z)$. The equations of motion can be written as[3]

$$\ddot{x} + \frac{q^2}{2m}\frac{\partial A_\phi^2}{\partial x} = -\omega_c \dot{z}$$

$$\ddot{z} + \frac{q^2}{2m}\frac{\partial A_\phi^2}{\partial z} = \omega_c \dot{x}$$

For $B_\phi = 0$ the condition for stability, to first order in X, is that A_ϕ has a minimum at $x=0$ and $z=0$. When B_ϕ is not equal to zero, the condition for stability is that the vector potential has an extremum. The above equations are relativistically correct as long as the energy gained per revolution is small and m is replaced by the relativistic mass.

Runaway electron experiments using a toroidal device[5] have indicated a parametric dependence of beam disruption time t_x on external fields. The following mechanisms are dependent on the external fields and have been considered responsible for runaway beam disruption:

Negative mass instability[6] $t_x = \frac{1}{\omega}\, 0.059\, T_{ev}^{1/2}\, \frac{B_\phi^{1/2}\ \text{gauss}}{E_\phi\ \text{v/cm}}$

Loss of vector potential minimum[7] $t_x = \left(\frac{2 r_0^3 b m}{n e^2 T}\right)^{1/4} \left(\frac{B_\phi}{E_\phi}\right)^{1/2}$

Resistive current instability[3] $t_x = \frac{L I_m}{2\pi r_0 b B_{em} (1-n)\omega}$

Field-Fried ion acoustic wave instability[8] $t_x = (125\, E_\phi^{-1} \log \frac{23 E_0}{E_R})^{1/2}$

where

ω= frequency of the betatron field

B_ϕ= azimuthal magnetic field

E_ϕ= azimuthal electric field

I_m= maximum azimuthal current

B_{om}= maximum betatron magnetic field at the equilibrium orbit

n= field index

b= minor radius of the vacuum chamber

R_o= major toroidal radius of the equilibrium orbit

L= plasma current inductance

T= plasma temperature

m= electron mass

The resistive current instability appears to play an important role in the observed absence of runaway electrons during the large current discharges; therefore, the details of this effect will now be given. In addition to the runaway current, there will be current due to electrons out of phase with the betatron magnetic field. This conduction current produces a shift in the position of the equilibrium orbit.

The displacement of the equilibrium orbit due to the conduction current can be found in the following way:[3]

$$B_z = \frac{1}{r}\frac{\partial (r A_\phi)}{\partial r}$$

or

$$\frac{\partial A_\phi}{\partial r} = B_z - \frac{A_\phi}{r}$$

and $B_z = B_{z0}\left(\frac{r_0}{r}\right)^n = B_{z0}\left(1-\frac{nx}{r_0}\right)$

so that $\frac{\partial A_\phi}{\partial r} = B_{z0}\left(1-\frac{nx}{r_0}\right) - \frac{A_\phi}{r}$

A_ϕ can be expanded about the equilibrium orbit

$$A_\phi^{(r)} = A_\phi(r_0) + \frac{1}{2}\left.\frac{\partial^2 A_\phi}{\partial r^2}\right)_0 x^2$$

where $\left.\frac{\partial A_\phi}{\partial r}\right)_0 = 0$

The term $\left.\frac{\partial^2 A_\phi}{\partial r^2}\right)_0$ can be evaluated by considering

$$\frac{\partial}{\partial r}\left\{\frac{\partial A_\phi}{\partial r} = B_z - \frac{A_\phi}{r}\right\}_0$$

$$\left.\frac{\partial^2 A_\phi}{\partial r^2}\right)_0 = \left.\frac{\partial B_z}{\partial r}\right)_0 + \left.\frac{1}{r^2} A_\phi\right)_0$$

$$= -\frac{nB_{z0}}{r_0} + \frac{B_{z0}}{r_0}$$

$$= \frac{B_{z0}}{r_0}(1-n)$$

where one uses $\left.A_\phi\right)_0 = \left.r B_z\right)_0 - \left.r\frac{\partial A_\phi}{\partial r}\right)_0 = B_{z0} r_0$

Thus $$A_\phi(r) = r_0 B_{z0} + \frac{1}{2}\frac{B_{z0}}{r_0}(1-n)x^2$$

to second order in X.

To first order in X $\quad A_\phi^{(r)} = r_0 B_{z0}$

and $$\frac{\partial A_\phi}{\partial r} = B_{z0}\left(1-\frac{nx}{r_0}\right) - B_{z0}\left(1-\frac{x}{r_0}\right)$$

or $$\frac{\partial A_\phi}{\partial r} = B_{z0}\frac{x}{r_0}(1-n)$$

For the vacuum fields $\frac{\partial A_\phi^b}{\partial r} = B_{z0}(1-n)\frac{x}{r_0}$

while for the fields created by the current flow

$$A_\phi^s = \frac{\phi^s}{2\pi r}$$

where $\phi^s = LI$, I = total current flow, L = inductance of the current column.

Thus $$\frac{\partial A_\phi^s}{\partial r} = \frac{-\phi^s}{2\pi r^2} + \frac{1}{2\pi r}\frac{\partial \phi^s}{\partial r}$$

The runaways experience a vector potential given by

$$A_\phi = A_\phi^b + A_\phi^s$$

where $\frac{\partial A_\phi}{\partial r}\Big)_o = 0$ for stable orbits. At the equilibrium orbit the self field will be zero provided that the current is uniformly distributed about the equilibrium orbit and toroidal corrections are neglected.

$$B'_{z0} = \frac{1}{2\pi r_0}\left(\frac{\partial \phi'}{\partial r}\right)_0 \cong 0$$

Thus near the equilibrium orbit $\frac{\partial A'_\phi}{\partial r} \cong -\frac{LI}{2\pi r^2}$

and $$0 = B_{z0}(1-n)\frac{x}{r_0} - \frac{LI}{2\pi r^2}$$

or $$x = \frac{LI}{2\pi r_0 B_{z0}(1-n)}$$

which represents the displacement of the equilibrium orbit.

The vector potential well depth, δ, allows one to fix the values of x and n.[9] Since n must be between 0 and 1, an estimate of δ for stable orbits within the vacuum chamber walls can be made.

$$\delta \equiv \frac{A_\phi(r) - A_\phi(r_0)}{A_\phi(r_0)}$$

Thus from the expression for $A_\phi(r)$ derived above

$$\delta = \frac{\frac{1}{2}x^2\frac{B_0}{r_0}(1-n)}{r_0 B_0} = \frac{1}{2}x^2\frac{(1-n)}{r_0^2}$$

In this experiment

$x = 2.5$ cm
$r_0 = 19$ cm

and we wish n to be $n \cong 0.5$

Thus $\delta \cong \frac{1}{2}\%$.

The measurement of δ is discussed in chapter IV.

In the presence of a strong toroidal field, the guiding center approximation predicts the same motion as

does the single particle theory. The guiding center approximation considers particle motion to be made up of a rapid gyration about the magnetic field lines plus a slower drifting of the center of gyration. The velocity of the guiding center perpendicular to the magnetic field is given by $\underset{\sim}{w}_\perp = \frac{1}{q} \frac{\underset{\sim}{F}_\perp \times \underset{\sim}{B}}{B^2}$ where $\underset{\sim}{F}_\perp$ is the force perpendicular to $\underset{\sim}{B}$. Motion parallel to the magnetic field is

$$\frac{d\underset{\sim}{w}_\parallel}{dt} = \frac{1}{m} \underset{\sim}{F}_\parallel$$

For freely accelerated particles in a combined betatron plus azimuthal field the drift velocity is given by

$$\dot{x} = \frac{\omega_\beta^2}{\omega_c} n \, z$$

$$\dot{z} = -\frac{\omega_\beta^2}{\omega_c}(1-n)x + \frac{1}{2}\frac{v_\perp^2}{r_0 \omega_c}$$

The x drift and the term linear in x in the z drift are due to the betatron restoring forces. The second term in the z drift is due to the gradient B-drift. The characteristic length of the guiding center, the cyclotron radius, is the distance between the center of gyration and the charged particles; the cyclotron radius is $R_c = \frac{mv_\perp}{qB}$

The characteristic time scale is one over the cyclotron frequency $\omega_c = \frac{eB}{mc}$

The magnetic moment of the gyrating charged particle is

$$|\mu_m| = \frac{1}{2}\frac{mv_\perp^2}{B}$$

With respect to slow changes in the magnetic field, the magnetic moment is constant, i.e., an adiabatic invariant.

Plasma particles in the same external fields may have very different modes of motion due to the trapping of particles in external magnetic field wells. In the toroidal configurations of this study one can distinguish between trapped particles and untrapped particles. Particle trapping occurs along the longitudinal direction. This can be due to wells caused by the finite number of azimuthal field coils or by the gradient in the helical field lines which are produced by the azimuthal field plus the poloidal field generated by the plasma current flow.

A toroidal field can be viewed as consisting of two regions.[15] The inner region is composed of continuous magnetic field lines which do not branch and which may be followed along the toroidal axis for an unbounded number of turns. These lines do not intersect the chamber walls. The external region, not having these properties, is separated from the internal region by the separatrix surface. Since in magnetohydrodynamic equilibrium the pressure is constant along magnetic field lines, the inner region of a toroidal field is important for plasma confinement. This is the region to be considered in the following discussion.

Figure 3 shows a plane P perpendicular to the toroidal axis inside the toroidal volume. A field line intersects the plane P at a point which is called an image point. A

field line may close on itself after n circuits about the torus producing n image points or never close on itself producing an infinite number of image points. For symmetric fields the image points lie on a closed curve in the P plane. A magnetic surface is that surface where a magnetic line of force passes arbitrarily close to any point on the surface. For small perturbations of the symmetry only part of the lines of force form a magnetic surface. The magnetic axis is that line of force which is surrounded by a magnetic surface and transforms into itself each time around the torus. A given magnetic field configuration can have more than one magnetic axis.

The rotational transform, ι , is the angle of rotation of an image point after one toroidal rotation. A given magnetic surface is seen to be composed of closed field lines if $\frac{\iota}{2\pi}$ is a rational number. One defines the longitudinal flux Φ and the azimuthal flux χ as the magnetic flux through a toroidal section transverse to the major plane (constant ϕ) and the magnetic flux through the region bounded by the magnetic axis and the line θ = constant (θ is the poloidal angle) respectively. The rotational transform may be written in terms of the longitudinal flux and the azimuthal flux $\iota = 2\pi \frac{d\chi}{d\Phi}$. For the ratio of the toroidal minor axis to toroidal major axis much less than 1, a cylindrical geometry is often

used to approximate the toroidal geometry. For the case of a straight circular cylindrical conductor of length L carrying a uniform current along a uniform axial magnetic field, B_o, ℓ can be easily evaluated. The azimuthal magnetic field is $B_\phi = B_a \frac{r}{a}$, where B_a is the magnetic field at the outer edge of the current column. Integrating over the azimuthal flux between $r=0$ to $r=a$ and $z=0$ to $z=L$ for a fixed ϕ we have the azimuthal flux given by $\chi = B_a \frac{r^2}{2a} L$

The longitudinal flux is given by $\Phi = \pi r^2 B_o$

Thus $$\ell = \frac{L}{a} \frac{B_a}{B_o}$$

For $L = 2\pi R$, R is the major radius of the toroidal field, for $a/R \ll 1$, and for a uniform current flowing parallel to a uniform toroidal field we have that

$$\ell = 2\pi \frac{R}{a} \frac{B_a}{B_o}$$

Since the circular azimuthal magnetic field lines and the longitudinal magnetic field lines must lie on magnetic surfaces, these surfaces will be coaxial and circular in cross section. Thus one expects a toroidal field to be of this nature. The effect of a/R being greater than 0 is to shift the centers of these surfaces.[19]

The existence of particle trapping by a corrugated magnetic field represented by $B = B_o(1 - \varepsilon \cos k_o s)$ is easily shown. For no electric field, the guiding center motion parallel to B is $\frac{mv_{\parallel}^2}{2} + \mu B_o(1 - \varepsilon \cos k_o s) = E$.

Here E is the constant energy along the field line, $\frac{2\pi}{k_0}$ is the wavelength of corrugation, ϵ is the depth of corrugation, and S is the distance traveled along the field line. Particles are trapped if their parallel velocity is zero at any magnetic field strength up to the maximum value. This gives a relationship between the depth of corrugation and the maximum velocities in the parallel and perpendicular direction for trapping to occur, i.e.,

$$\frac{V_{\parallel}(0)}{V_{\perp}(0)} \leq \sqrt{\frac{2\epsilon}{1-\epsilon}}$$

A toroidal field, composed of a longitudinal field plus a weak poloidal field, has the approximate form

$$B = B_0\left(1-\frac{x}{R}\right) = B_0\left(1-\frac{a}{R}\cos\theta\right) = B_0(1-\epsilon\cos\theta)$$

provided that $\frac{x}{R}$ is much less than 1. Let the z-axis be along a toroidal magnetic field line. After one circuit the angle the field line rotates is denoted by ℓ, the rotational transform. Let δ denote the angle the field line rotates after traveling a distance S. Then one obtains the equation $\delta = \frac{\ell S}{2\pi R}$

ℓ has been evaluated for this situation. Thus

$$\delta = \frac{S}{R_0} q$$

where $q = \frac{a}{R}\frac{B_0}{B_\theta}$ is the safety factor. So when B is viewed along the z-axis one may write $B = B_0(1-\epsilon\cos\delta) = B_0(1-\epsilon\cos k_0 z)$

where $k_0 = \frac{1}{qR}$ This means a toroidal field of the type being discussed is corrugated

and therefore particle trapping can occur. The projection of these trapped orbits on a plane transverse to the toroidal plane has a banana shape, explaining why these are called banana orbits. These trapped particles diffuse at a different rate than untrapped particles due to the different step sizes in their motion, that is, the difference between the width of a banana orbit and the width of a cyclotron rotation.

The second method of describing a plasma is through a fluid or macroscopic model. The plasma is considered to be a conducting fluid. The first and second moments of the Maxwell-Boltzmann equation give rise to fluid-like equations for the plasma[4] of the form

$$\frac{\partial \rho}{\partial t} + \nabla \cdot (\rho \underset{\sim}{v}) = 0$$

$$\rho \frac{d\underset{\sim}{v}}{dt} = -\nabla p + \underset{\sim}{f}$$

ρ is the fluid density, $\underset{\sim}{v}$ the velocity, p the pressure, and $\underset{\sim}{f}$ the external force acting on the fluid. Since plasmas generally have very high electrical conductivities, it is a common approximation to neglect the displacement current with repect to the plasma conduction current and assume that the space charge inside the plasma is zero. The additional equations used to describe the plasma fluid are

$$\nabla \times \underset{\sim}{B} = \frac{4\pi}{c} \underset{\sim}{J} \qquad \nabla \cdot \underset{\sim}{E} = 0$$

$$\nabla \times \underset{\sim}{E} = -\frac{1}{c} \frac{\partial \underset{\sim}{B}}{\partial t} \qquad \underset{\sim}{J} = \sigma \left(\underset{\sim}{E} + \frac{\underset{\sim}{v}}{c} \times \underset{\sim}{B} \right)$$

$\nabla \cdot \underset{\sim}{B} = 0 \qquad \underset{\sim}{f} = \frac{1}{c} \underset{\sim}{J} \times \underset{\sim}{B}$

For an infinitely conductive plasma and an isolated plasma one can show that the energy of the plasma fluid, E, is

$$\int \left(\frac{1}{2} \rho v^2 + \frac{p}{\gamma - 1} + \frac{B^2}{8\pi} \right) d\tau = E$$

and E is a constant. Here one assumes an adiabatic equation of state given by $p\rho^{-\gamma} = \text{constant}$.

For plasma fluid equilibrium $\rho \frac{dv}{dt} = 0$

or $$\frac{1}{c} \underset{\sim}{J} \times \underset{\sim}{B} = \nabla p$$

In a region in which $\underset{\sim}{B} = 0$, $\nabla p = 0$ or p is a constant. If ∇p is not equal to zero than for systems in equilibrium

$$\underset{\sim}{J} \cdot \nabla p = 0$$

$$\underset{\sim}{B} \cdot \nabla p = 0$$

which means that the constant p surfaces are also surfaces of constant magnetic field. Using Ampere's law and the relationship between $\underset{\sim}{J}$, $\underset{\sim}{B}$ and p in equilibrium one obtains $\nabla \left(p + \frac{B^2}{8\pi} \right) = \frac{1}{4\pi} (\underset{\sim}{B} \cdot \nabla) \underset{\sim}{B}$.

One can easily show that a toroidal plasma of infinite conductivity cannot be in equilibrium in the presence of only a longitudinal $\frac{1}{R}$ magnetic field. For this case the magnetic field vanishes inside the plasma so that $\nabla p = 0$ for equilibrium everywhere inside the plasma. In particular, on the inner surface where R is smaller and on the outer surface, where R is larger, p is the same. The term $(\underset{\sim}{B} \cdot \nabla) \underset{\sim}{B}$ is zero since we assume $\underset{\sim}{B}$ is cylindrically symmetric. Thus $\nabla \left(p + \frac{B^2}{4\pi} \right) = 0$

along the plasma surface if it is in equilibrium. Since ∇p is zero the gradient of $\frac{B^2}{4\pi}$ must be zero, but B varies as $\frac{1}{R}$ so that equilibrium is not possible with a longitudinal field alone.

A toroidal plasma which is conducting a current cannot be in equilibrium unless a magnetic field perpendicular to the plane of the current ring is present.[16] The magnitude of the required field is

$$B_{\perp 0} = \frac{I_p}{c R_p}\left(\ln \frac{8R_p}{a} + \Lambda - \frac{1}{2}\right)$$

where

$$\Lambda = 4\pi \frac{\left(\langle p_\parallel \rangle + \langle p_\perp \rangle\right)}{B_a^2} + \frac{\ell_i}{2} - 1$$

$$B_a = \frac{2I_p}{ca}$$

a = minor plasma radius

R_p = major plasma radius

I_p = longitudinal current flow

ℓ_i = internal inductance per unit length = $\frac{\overline{B_\theta^2}}{B_a^2}$

B_θ = poloidal magnetic field = $B_a\left(1 + \frac{a}{R}\Lambda\cos\phi\right)$

If one knows the azimuthal magnetic field, an estimate of the plasma pressure is seen to be possible.

The radial force acting on the current ring is given by

$$F_R = -\frac{2\pi}{c} R_p I_p \left(B_\perp - B_{\perp 0}\right)$$

Knowing $B_\perp$ as a function of time, one can compute the distance as a function of time that the plasma ring moves due to the mismatch between $B_\perp$ and $B_{\perp 0}$.

In order for the plasma column to be stable against displacement in the vertical and radial direction the

field index n must have a value $0 < n < 3/2$. In order to maintain the proper shape of the magnetic field surfaces[17] the poloidal β , β_θ , must satisfy the condition

$$\beta_\theta \equiv \frac{8\pi n (T_e + T_i)}{B_\theta^2} \lesssim R/a$$

To avoid kink instabilities (and other magnetohydrodynamic instabilities) the so-called safety factor, q, must be greater than one for all values of the poloidal r

$$q(r) \equiv \frac{B_\phi}{B_\theta(r)} \frac{r}{R} > 1$$

The particular minimum value of $q(r)$ depends on the exact nature of the current distribution.[17]

Kinetic theory is a microscopic approach to plasma phenomena which is very suitable for studying collective effects. Here a brief outline of the linear theory of the growth of ion-acoustic waves is presented. The linearized Vlasov equation for electrostatic perturbations in the absence of magnetic fields may be written as[18]

$$\frac{\partial f_{\alpha 1}}{\partial t} + \underset{\sim}{v} \cdot \underset{\sim}{\nabla} f_{\alpha 1} = -\frac{q_\alpha}{m_\alpha} \underset{\sim}{E}_1 \cdot \underset{\sim}{\nabla}_v f_{\alpha 0}$$

Each charged particle species in the plasma (represented by a different α) obeys the Vlasov equation. The distribution function is $f = f_0 + f_1$. f_0 is the initial equilibrium distribution function and f_1 is a small departure from f_0 . E_1 is the electric field produced by the perturbation in the plasma. One notes that

$$\underset{\sim}{E}_1 = -\underset{\sim}{\nabla} \phi_1$$

and

$$\nabla^2 \phi_1 = -4\pi \sum_\alpha \bar{n}_\alpha q_\alpha \int f_{\alpha 1} \, d\underset{\sim}{v}$$

The plasma waves that are generated are periodic variations in ϕ_1 . By taking the Laplace transform and Fourier transform of the Vlasov equation one arrives at the condition that the dielectric function, $D(\underset{\sim}{k}, \omega)$, must be zero for solutions. This gives a relationship between ω and $\underset{\sim}{k}$. For a one dimensional plasma composed of a stationary ion background on which is superimposed a drifting Maxwellian distribution of electrons, one finds that the normal modes of oscillation are ion sound waves and electron plasma waves. These modes will grow provided that $u_0/\bar{v}_e$ and T_e/T_i are large enough. The sufficient condition for growth of ion acoustic waves is $T_e \gg T_i$ and $u_0 > c_s$. For $u_0 > \bar{v}_e$ electron plasma waves are unstable over a wide range of temperatures. The equilibrium distribution functions are of the form

$$f_{oi} = \left(\frac{m_i}{2\pi k T_i}\right)^{1/2} \exp\left\{-\frac{m_i v^2}{2kT_i}\right\}$$

$$f_{oe} = \left(\frac{m_e}{2\pi k T_e}\right)^{1/2} \exp\left\{-\frac{m_e (u-u_0)^2}{2kT_e}\right\}$$

In order to be able to analytically evaluate the dielectric function $D(k,\omega) = 1 + \sum_\alpha \frac{\omega_{p\alpha}^2}{k^2} \int_{-\infty}^{\infty} \frac{k \frac{\partial F_{\alpha 0}}{\partial u}}{\omega - ku} du$ one must consider waves of frequencies such that

$$\frac{\omega_r}{k} \gg \sqrt{\frac{kT_i}{m_i}} \quad \text{and} \quad \left|u_0 - \frac{\omega_r}{k}\right| \ll \sqrt{\frac{kT_e}{m_e}} \; .$$

The effect of these conditions, as seen by inspection of figure 4, is as follows: For ions $\frac{\partial f_{io}}{\partial u} \cong 0$ when $u \geq \frac{\omega_r}{k}$ so that $\frac{1}{\omega - uk} \cong \frac{1}{\omega/k}\left(1 + \frac{u}{\omega/k}\right)$ and for the electrons $\frac{\partial f_{eo}}{\partial u} \cong 0$ when $u \leq \frac{\omega_r}{k}$ so that $\frac{1}{\omega - uk} \cong \frac{1}{uk}\left(1 + \frac{\omega}{ku}\right)$. This gives the

following expressions for ω_r and ω_i :

$$\omega_r = \frac{k^2 c_s^2}{1+k^2\lambda_{De}^2}$$

and $$\omega_i = -|\omega_r|\sqrt{\frac{\pi}{8}}\frac{1}{(1+k^2\lambda_{De}^2)^{3/2}}\left\{\left(\frac{T_e}{T_i}\right)^{3/2}\times \exp\left(-\frac{T_e}{T_i}\frac{1}{(1+k^2\lambda_{De}^2)}\right)+\sqrt{\frac{m_e}{m_i}}\left(1-\frac{u_0}{c_s}\sqrt{1+k^2\lambda_{De}^2}\right)\right\}$$

where $\lambda_{De} = \frac{\sqrt{2}}{2}\lambda_D$. ω_i represents the imaginary part of the wave frequency. The $\frac{u_0}{c_s}\sqrt{1+k^2\lambda_{De}^2}$ term represents a wave growth term. This competes with the other terms which cause wave damping. The application of this analytic result to experimental findings of this study will be made in chapter VII.

In a very weakly ionized plasma, the plasma electrical resistivity is due primarily to electron neutral collisions. Runaway electrons do not occur since the scattering cross section, σ_x , is independent of the electron velocity. In this case the collision frequency, ν , is given by

$$\nu = n\sigma_x v$$

where n is the plasma density and v is the electron velocity. Assuming hard sphere scattering in hydrogen with a neutral density of 1×10^{14} cc' and a plasma temperature of 20 ev, one obtains a collision frequency of $\nu \cong 4\times10^{3}$. For a fully ionized plasma a Fokker-Planck collision term[1,2] is used to evaluate the resistivity due to electron-ion encounters. Since the Coulomb scattering cross section decreases as $1/v^4$, the Coulomb collision frequency will decrease as $1/v^3$. Thus for strong enough electric fields the drift velocity is not

balanced by collisions and the collision frequency approaches zero. The Fokker-Planck treatment of electrical conductvity including effects for electron-electron interactions yields the following expression for electrical conductivity $\sigma_{class} = \frac{1.4 \times 10^8 \, T_{(K^\circ)}^{3/2}}{\ln \Lambda}$ esu

provided that $\Gamma \ll 1$ where $\Gamma = \frac{6.6 \times 10^8 \, T \, E_{(v/cm)}}{Z \, n_e \ln \Lambda}$

and $\Lambda = \frac{3}{2 Z Z_f e^2} \left(\frac{k^3 T^3}{\pi n_e} \right)^{1/2}$

The condition that Γ is much less than one allows the definition of a critical field strength, $E_{CRITICAL}$. For electric field strengths close to the critical field strength, the classical conductivity formula is invalid due to the generation of runaway electrons.[3] Setting Γ equal to one gives the definition of the critical field strength $E_{\substack{CRITICAL \\ (V/cm)}} = \frac{Z \ln \Lambda}{6.6 \times 10^8} \frac{n_e \, (cc^{-1})}{T_{(K^\circ)}}$

Only for electric field strengths well below the critical field strength does one expect the value of the classical conductivity to agree with observed conductivity. (See reference 15 in chapter I.) For electric field strengths near or above the critical field one expects free electron acceleration and a resulting increase of plasma current with time. It is noted that in a partially ionized gas one must take into account electron-neutral interactions in order to compute the classical resistivity correctly.[4]

Plasma resistivity has been studied in devices in which plasma currents are formed by external electric field strengths in excess of the critical field strength. The resistivity is observed to be one or more orders of magnitude higher than predicted by the classical $T^{-3/2}$ law. Consistant with this is the apparant lack of runaway electrons and observed disruption of runaway streams in some experiments. The decrease in conductivity is due to an enhancement of the electron momentum loss through wave-particle interactions as, for example, in the generation of ion acoustic waves.[5]

Anomolously low electrical conductivity has been observed in various toroidal devices in which the applied electric field is greater than the critical field. In these cases a longitudinal magnetic field is used to restrict plasma transport to the vacuum chamber walls. Demidov, et al.,[6] showed the presence of an anomolously low conductivity plateau for a one electron volt plasma electron temperature, a density of 1×10^{12} cc^{-1}, and an electric field strength between 0.4v/cm and 20v/cm. For an electric field larger than 20v/cm a continued fall off of conductivity was observed. These measurements were performed in a hydrogen plasma formed by plasma gun injectors. Hamberger and Friedman[7] studied the variation of conductivity for field strengths from 0.4v/cm to

300v/cm. Their results did not show the Demidov, et al., plateau though their conductivity values appeared to agree, within a factor of two or three, with the Demidov, et al., value near the plateau region. The Hamberger and Friedman conductivity decreased monotonically with electric field strength until the electric field strength reached 100v/cm and then a second plateau was reached. Hamberger and Friedman claimed that the conductivity scaled as $\left(\frac{m_i}{m_e}\right)^{1/3} n^{1/2}$, where m_i = ion mass, m_e = electron mass, and n = plasma density. This agrees with the conductivity that would result from a two stream electron-ion interaction.[8] Mah, et al.,[9] studied anomolous resistivity for electric field strengths in the range of 38v/cm to 71v/cm. They found values which decreased with increasing field strength, as did Hamberger and Friedman, but their numerical values seemed to agree best with the theory of Dupree[10] provided they chose the inverse of the ion acoustic wave number to be equal to one Debye length. The dependence of the observed resistivity on the applied electric field strength was not explained. In the experiment of Hamberger and Jancarik[11] conductivity for field strengths from 100v/cm to 500v/cm were studied. Here regimes corresponding to two stream instability and ion acoustic instability were found depending on the ratio of

electron drift velocity to ion acoustic speed $\frac{u_o}{c_s}$ and the ratio of electron drift velocity to the average thermal velocity $\frac{u_o}{\bar{v}_e}$. For $u_o/c_s > 1$ and $u_o/\bar{v}_e < 1$ ion acoustic waves were believed responsible for the measured resistivity. For $u_o/\bar{v}_e > 1$ the conductivity was found to agree with the results of Hamberger and Friedman. Table 1 summarizes these experimental results.

Theoretical estimates of plasma resistivity have been made for electric fields greater than the critical field. The electron-plasma wave regime, or two stream instability regime, has been investigated by Buneman[12] and Sizenenko and Stepanov[13]. Their expressions for conductivity are

Buneman: $\sigma = \omega_{pe} \frac{1}{2} \left(\frac{m_i}{m_e}\right)^{1/3}$

Sizenenko and Stepanov: $\sigma = \frac{\omega_{pe}^2}{2\pi \omega_{pi}}$

where ω_{pe} and ω_{pi} are the electron plasma frequency and ion plasma frequency, respectively. The electron-ion acoustic wave interaction has been investigated by Sagdeev,[11] Dupree,[10] and Sizenenko and Stepanov[14]. The expressions for conductivity in these cases are given by

Sagdeev: $\sigma = 10^{12} \frac{T_i}{T_e} \frac{\bar{v}_e}{u_o} \frac{\omega_{pe}}{4\pi}$

Sizenenko and Stepanov: $\sigma = \frac{\omega_{pe}}{8\pi} \frac{m_i}{m_e}$

Dupree: $\sigma = (32)^{1/2} \frac{\omega_{pe}}{k \lambda_D}$

where λ_D is the Debye length and k is the ion acoustic wave number of greatest growth rate.

CHAPTER II

FIGURE AND TABLE CAPTIONS

TABLE I

EXPERIMENTAL RESULTS OF OTHER RESEARCHERS

	Demidov et al. 1967	Hamberger and Friedman 1968	Mah et al. 1970	Hamberger and Jancarik 1972
E_{ϕ} v/cm	0.4 to40	0.7 to200	38,50,71	100to500
$n_{cc^{-1}}$	10^{12}	10^{11} to10^{13}	$3x10^{11}$	10^{11} to10^{13}
Other reported measurements	10^{2}MHz	plasma column size	*T_e, T_i for first part of trial	wave spectrum using high frequency probe
σ_{argon} esu	not measurable	$7.5x10^{11}$at plateau	$1.1x10^{12}$, $5.4x10^{11}$, $1.1x10^{11}$,	$\frac{\sigma}{\omega_{pe}}$ =25to5
$\sigma_{Hydrogen}$ esu	$2.8x10^{12}$ at plateau	$5x10^{12}$to $3x10^{11}$at plateau	not reported	not reported
Assumed theory to fit data	electron-ion acoustic	Buneman 2-stream	Dupree	Different regimes found

*Hirose, et al.,(1970)[20] measured plasma fluctuations near 200 MHz.

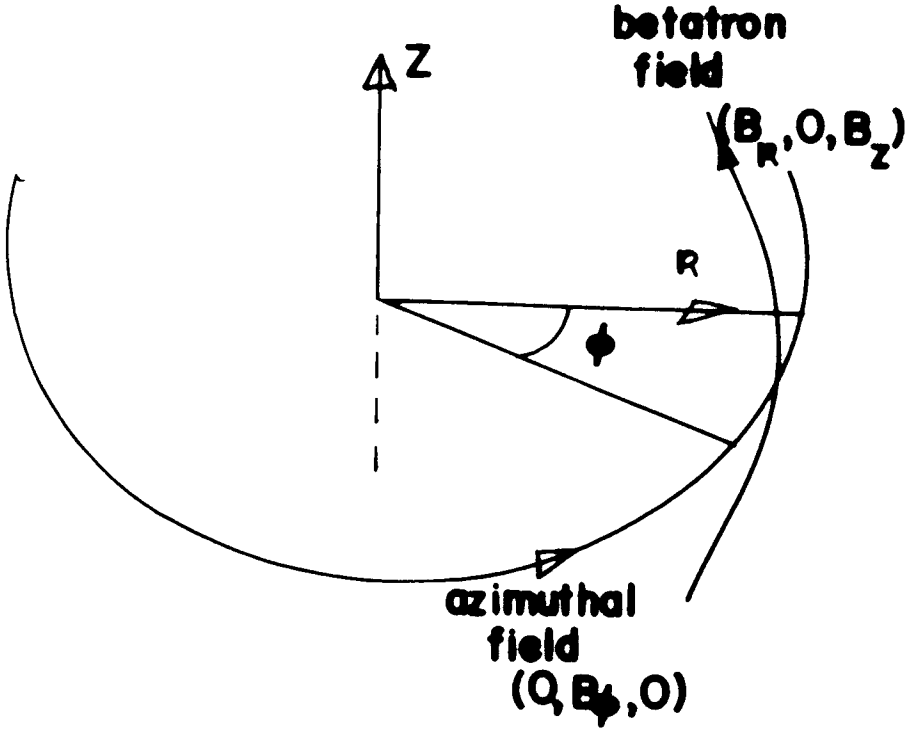

FIG. 1

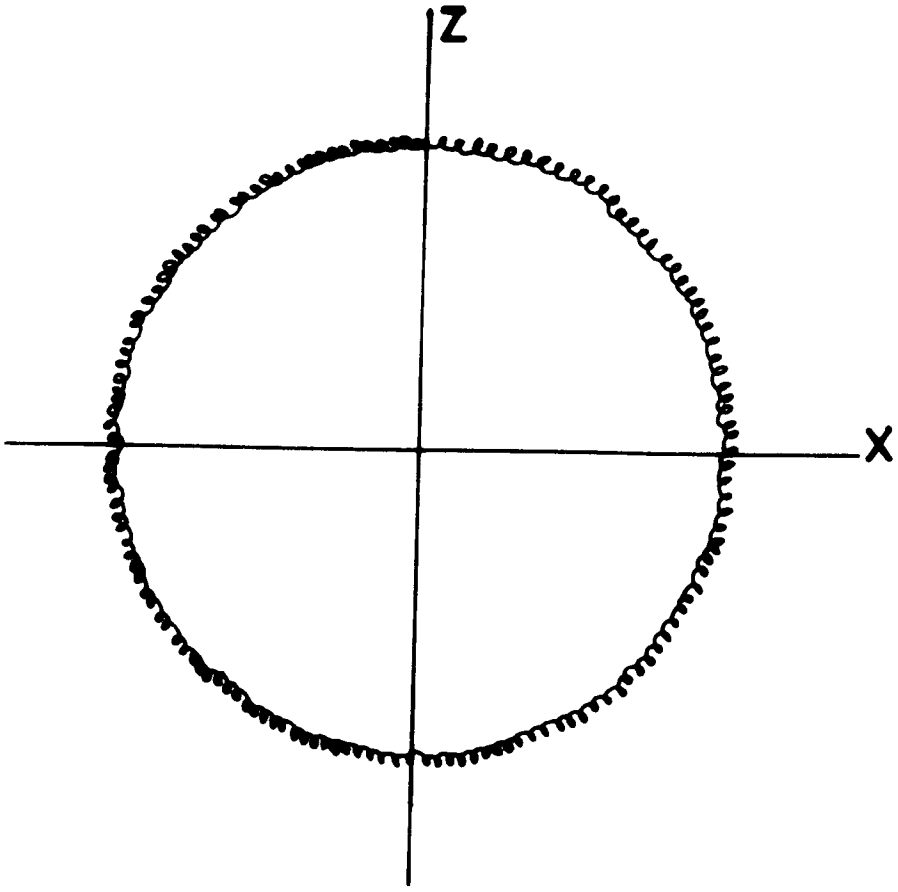

FIG.2

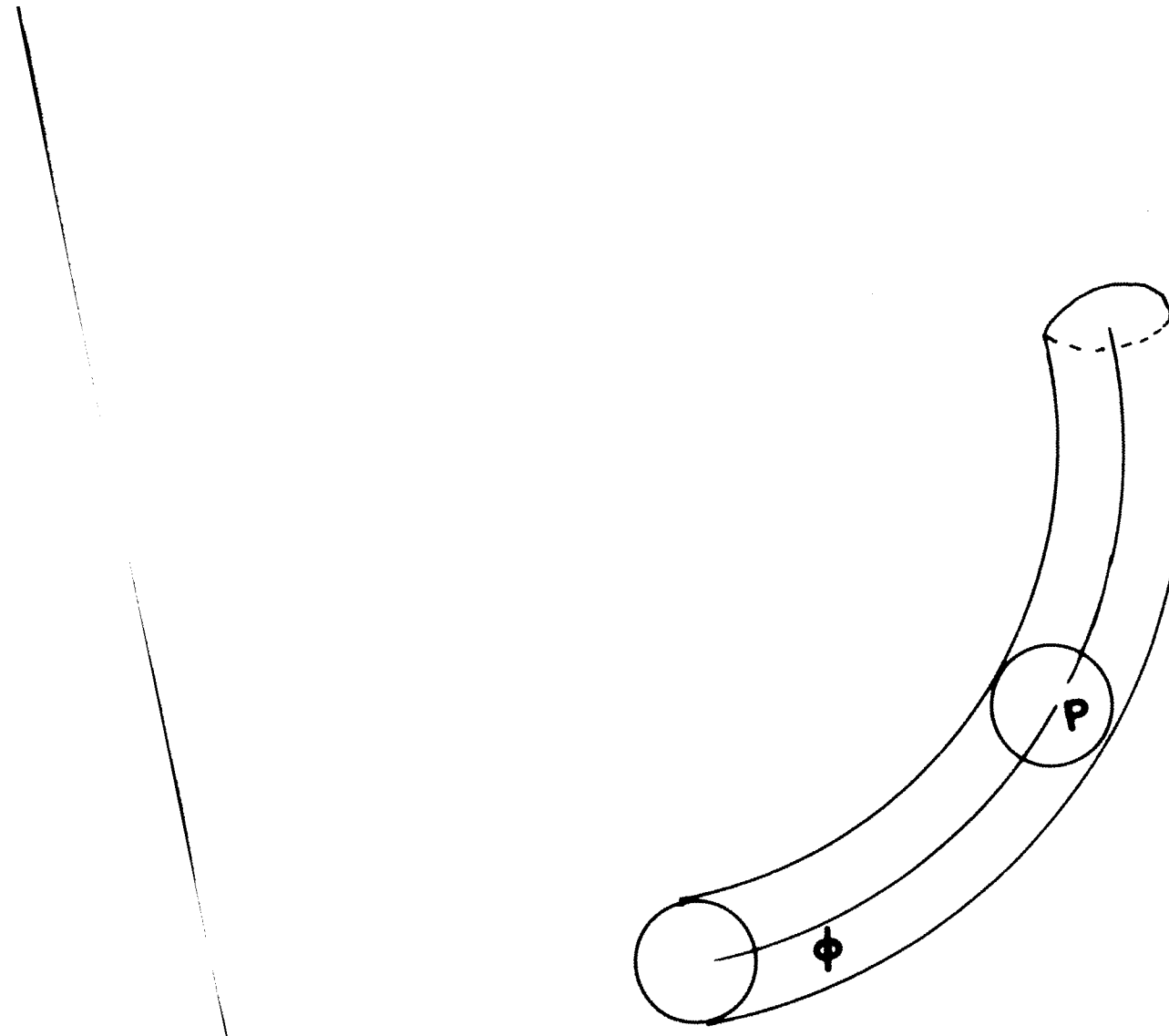

FIG. 3

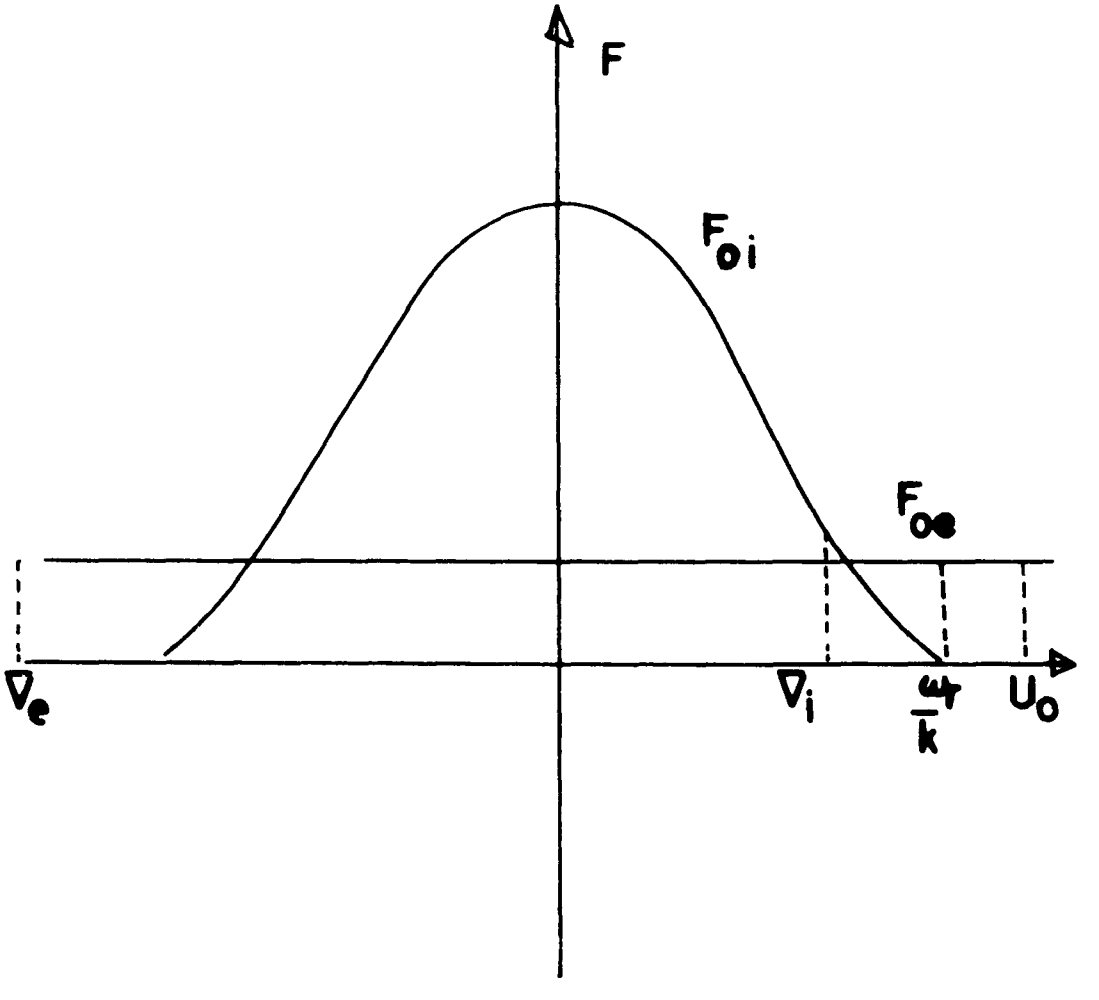

FIG.4

REFERENCES

CHAPTER II

1. L. A. Ferrari and M. S. Zucker, Particle Accelerators 2, 121 (1971).
2. J. G. Linhart, Plasma Physics (North Holland Publishing Company, Amsterdam, 1960).
3. L. A. Ferrari and M. S. Zucker, The Physics of Fluids 12, 1312 (1969).
4. G. Schmidt, Physics of High Temperature Plasmas (Academic Press, New York, 1966).
5. L. A. Ferrari and K. C. Rogers, The Physics of Fluids 10, 1319 (1967).
6. R. W. Landau, The Physics of Fluids 11, 205 (1968).
7. L. A. Ferrari, The Physics of Fluids 12, 2203 (1969).
8. E. C. Field and B. D. Fried, The Physics of Fluids 7, 1937 (1964).
9. L. A. Ferrari, Ph. D. Thesis, 1965 Stevens Institute of Technology, Hoboken, New Jersey.
10. T. H. Dupree, Physical Review Letters 25, 789 (1970).
11. S. M. Hamberger and J. Jancarik, The Physics of Fluids 15, 825 (1972).
12. O. Buneman, Physical Review 115, 503 (1959).

13. V. L. Sizenenko and K. N. Stepanov, Plasma Physics 13, 1033 (1971).

14. V. L. Sizenenko and K. N. Stepanov, J.E.T.P. Letters, 9, 282 (1969).

15. A. L. Morozov and L. S. Solov'ev, Reviews of Plasma Physics, M. A. Leontovich, Editor, (Consultants Bureau, New York, 1966). Volume 2.

16. V. D. Shafranov, Reviews of Plasma Physics, M. A. Leontovich, Editor,(Consultants Bureau, New York, 1966). Volume 2.

17. L. A. Artsimovich, Nuclear Fusion 12, 215 (1972).

18. N. A. Krall and A. W. Trivelpiece, Principles of Plasma Physics (McGraw-Hill Book Company, New York, 1973).

19. J. M. Greene, J. L. Johnson, and K. E. Weimer, The Physics of Fluids 14, 671 (1971).

20. A. Hirose, et al., Physical Review Letters 28, 1185 (1972).

CHAPTER III

EXPERIMENTAL APPARATUS

The apparatus used[1] is shown in figure 1 and consists of a toroidal vacuum chamber made from two Pyrex semicircles. These sections were bent from standard 5.08cm inner diameter Pyrex tubing. The major diameter is thirty-eight centimeters. Two 3.81cm inner diameter straight sections of Pyrex tubing are connected through the walls of the torus and serve as access ports. The semicircular construction was necessary in order to allow for twelve coils, six on each semicircle, to be placed around the minor circumference of the torus. The coils of 15.2cm outer diameter, 10.0cm inner diameter and 3.40cm thickness have a 2.87 microhenry inductance and supply an approximately six millisecond wide longitudinal magnetic field pulse. Field strengths in excess of two kilogauss have easily been obtained.

The coils were constructed by first winding 160 turns of number 12 A. W. G. single cotton, single polythermalize copper magnet wire on a spindle. The wound coil was then placed on a form which was filled with epoxy. This was placed into a vacuum oven which was slowly evacuated to

allow any air bubbles to escape from the epoxy. Heating the epoxy decreased its viscosity helping it to flow between the wire layers and decreasing the curing time.

The longitudinal magnetic field coils are held in place by two sheets of Benelex (61.0cm x 61.0cm x 2.54cm) with concave wells machined into the sheets. The plane of the sheets are parallel to the toroidal plane and are held in place by twelve 2.54cm plastic rods, twelve tubular spacers and nuts. The toroidal glass chamber was sealed by wrapping the joints in fiberglass cloth and applying successive layers of epoxy.

Two coaxial loops of Litz wire are embedded into each sheet of Benelex. The inner loop has a major diameter of 24.0cm and the outer loop has a major diameter of 52.0cm. The inner loop is made up of seven bundles of fifty-nine loops of number 36 wire wound 80.5 times around a quarter-inch Teflon rod in the form of a helix. The outer loop is composed of seven bundles of sixty loops, each of number 40 copper wire. With these coils we expected a current division of 1.000 to 0.775 between the current in the inner turn and the outer turn.

Using the analytic form for the magnetic field due to a circular loop of wire[2]

$$B_z = \frac{2\mu_0 I}{\{(R_0+r)^2+z^2\}^{1/2}}\left[K(k^2)+\frac{R_0^2-r^2-z^2}{(R_0-r)^2+z^2}E(k^2)\right]$$

$k^2 = \frac{4R_0 r}{(R_0+r)^2+z^2}$; R_0 = loop radius

and using the polynomial approximation formulas for elliptical integrals[3] one can calculate the magnetic field, vector potential, and field index n at any point within the toroidal vacuum chamber. Figures 2 and 3 show the calculated variation of the vector potential as a function of position and the calculated variation of the betatron magnetic field as a function of position. The computed value of the field index n near the vector potential minimum is 0.36. The coil dimensions were originally computed by Skarsganrd and Gore[1] for a similar experimental device.

The plasma is formed by the use of a plasma gun. Several types of plasma injection devices were investigated. The first type studied is a single element gun as shown in figure 4. A number 18 copper wire is placed through a lavite cylinder placed in the center of a brass plate. The plate fits onto a three inch Pyrex pipe assembly which is evacuated by a diffusion pump. Background pressures in the 10^{-6} Torr region are attained. A spark forms between the copper wire and brass plate when a capacitor is discharged through the gun. This causes a plasma to be ejected down the Pyrex pipe. A double Langmuir probe[3] was built to try to measure the plasma

density and temperature but could not be succesfully used. A possible cause of difficulty was the lack of D. C. isolation between the gun and probe circuits. This apparently resulted in direct conduction of charge from the capacitor to the ground of the probe circuit.

A second type of gun that was built is a button gun.[4] Parallel wires were inserted into a cylinder of Lavite as shown in figure 5. Again the Lavite was mounted into a flange and attached to a Pyrex tube assembly. A spark forms between the two wires ionizing some of the wire and propelling plasma forward. Both tungsten and copper electrodes were used. Designs having different wire diameters and different spacings of the wires were tested. All designs lasted not more than 50 to 100 discharges. A different design was required which would last for many more discharges.

A third type of plasma gun that was built was a small coaxial gun. Figure 6 shows the final gun design used. The gun is similar to that of Fuentes and Forsen.[5] A major difference is that instead of using an occluded hydrogen electrode a copper electrode was first used. It was found that gun breakdown would not occur with background pressures below 10×10^{-3} Torr of argon. Feeding gas through the gun into the vacuum chamber did not improve

this performance appreciably. However, when a stainless steel screw is inserted through the outer copper tube and placed 0.013cm from the inner electrode regular breakdown occurs at neutral pressures as low as $3x10^{-6}$ Torr. (The limit of the diffusion pump.) With the first working model only about 500 discharges were created before the center electrode came loose due to insulation failure of the epoxy seal. The coaxial gun design was modified to prevent the ejection of the center electrode. The gun cable was also bent about 45 degrees so that the injected plasma would be traveling parallel to the longitudinal axis rather than perpendicular to it as in the first coaxial design. Both copper and hydrogen occluded titanium center electrodes are used. The useful gun life is very long. After several thousand discharges the starting screw may be reset, the gun cleaned out with a solvent, and reused.

The hydrogen occluded titanium gun injected large amounts of plasma into the toroidal vacuum chamber for the first several hundred discharges. Two guns mounted in each access port were initially used to try to inject a uniform amount of plasma into the vacuum chamber. Observing microwave transmission cutoff we could estimate the speed and density of the injected plasma. The injected plasma traveled with a longitudinal speed of about

2×10^6 cm/s and diffused to the vacuum chamber walls after 30 microseconds. The rapid diffusion may be explained by an analysis of the guiding center motion of the ions.[8] Due to the drift motion of the injected plasma's electrons and ions in the curved longitudinal magnetic field the ions travel to the vacuum chamber walls with a radial velocity given by

$$\frac{dv_R}{dt} = \frac{v_{\parallel}^2 + v_{\perp}^2/2}{R}$$

where R is the major toroidal diameter, $v_{\parallel}$ is the longitudinal ion speed, v_R is the radial ion speed, and $v_{\perp}$ is the ion motion perpendicular to the longitudinal magnetic field. If $v_{\perp} \ll v_{\parallel}$ than $\frac{dv_R}{dt} = \frac{v_{\parallel}^2}{R}$ and the plasmoid is confined to circular motion. However, if $\frac{v_{\perp}^2}{2}$ is comparable to $v_{\parallel}^2$, then the plasmoid has an acceleration which is greater than $\frac{v_{\parallel}^2}{R}$ and will move toward the vacuum chamber wall across the magnetic field lines. The radial acceleration is given by

$$\frac{dv_R}{dt} - \frac{v_{\parallel}^2}{R} = \frac{v_{\perp}^2}{2R}$$

and

$$\frac{1}{2} m v_{\perp}^2 = kT$$

Thus we can estimate the required ion temperature needed to produce the observed diffusion time. This turns out to be of the order of 0.5 electron volts. So one would expect the rapid diffusion of the injected plasma to occur for an ion temperature of about 0.5ev.

Capacitors were discharged at different times in order

to provide the betatron field, azimuthal magnetic field, and gun discharge. The timing of the discharges is shown in figure 7. Ignitron switches are used to activate the capacitor discharges. In order to provide the several hundred volt pulse needed to close these switches, amplifying networks were used consisting of a pulse generator, a Schmidt trigger circuit, and a hydrogen thyratron circuit. Figure 8 shows a schematic diagram of the triggering network. There was considerable difficulty in obtaining a consistent sequence of firing of these circuits. Isolating the individual circuits as much as possible rather than using a common ground seemed to provide a more reliable firing sequence. Isolation transformers were used between the pulse generators and Schmidt trigger circuits and between the thyratrons and ignitrons. The particular choice of 120v a. c. outlets used and whether the a. c. grounds were floating or not affected the sequence of firings. Also the reliability was variable from day to day even though no changes were made in the system. After the equipment hookups were arranged to minimize incorrect sequences of discharges it was found that by building more efficient transformers between the thyratrons and ignitrons a reduction in the thyratron capacitor voltage was possible. This appeared to reduce errors in the timing of the discharges.

CHAPTER III

FIGURE CAPTIONS

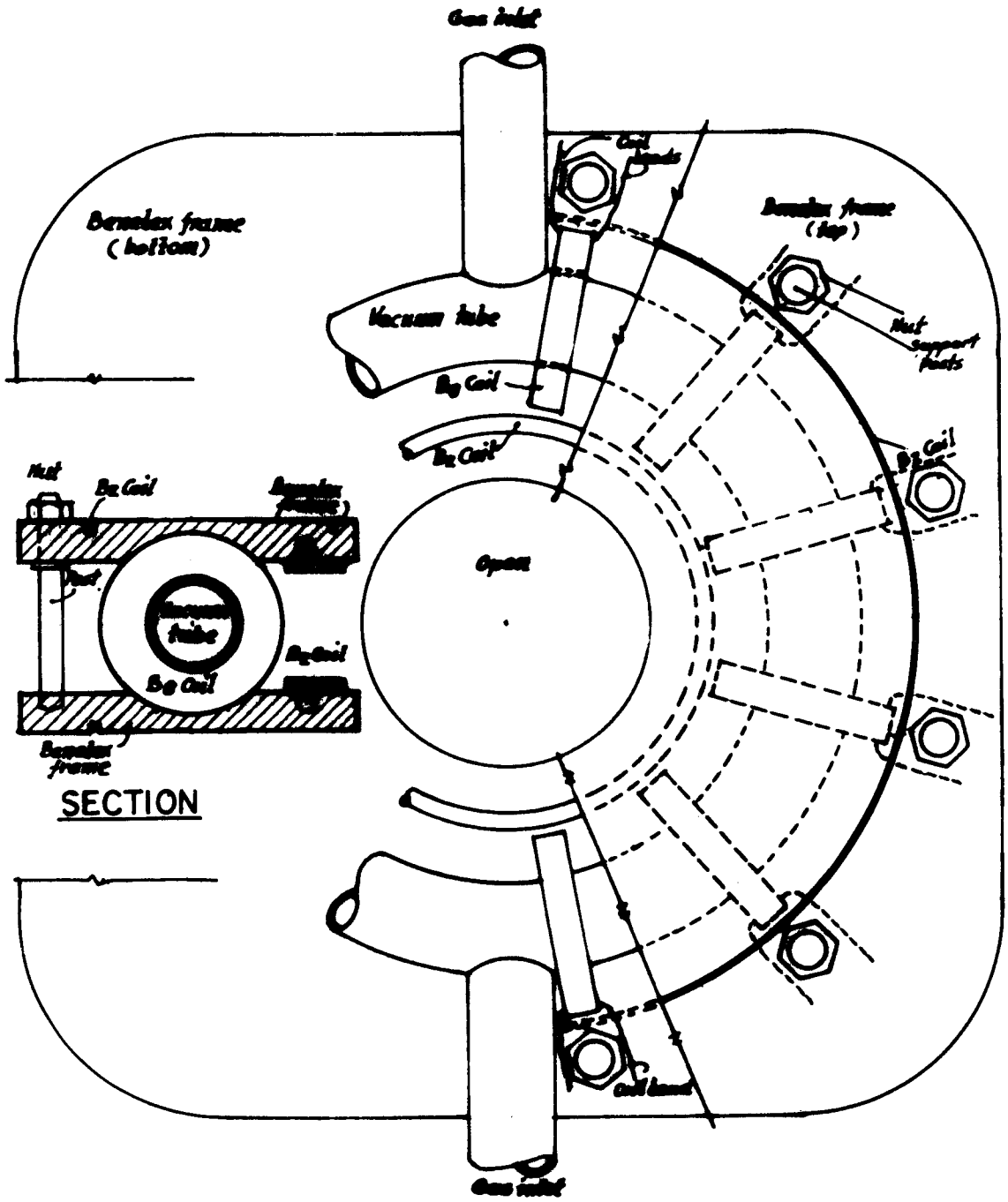

SECTION

PLAN

1/4 FULL SIZE

PLASMA BETATRON FIG. 1

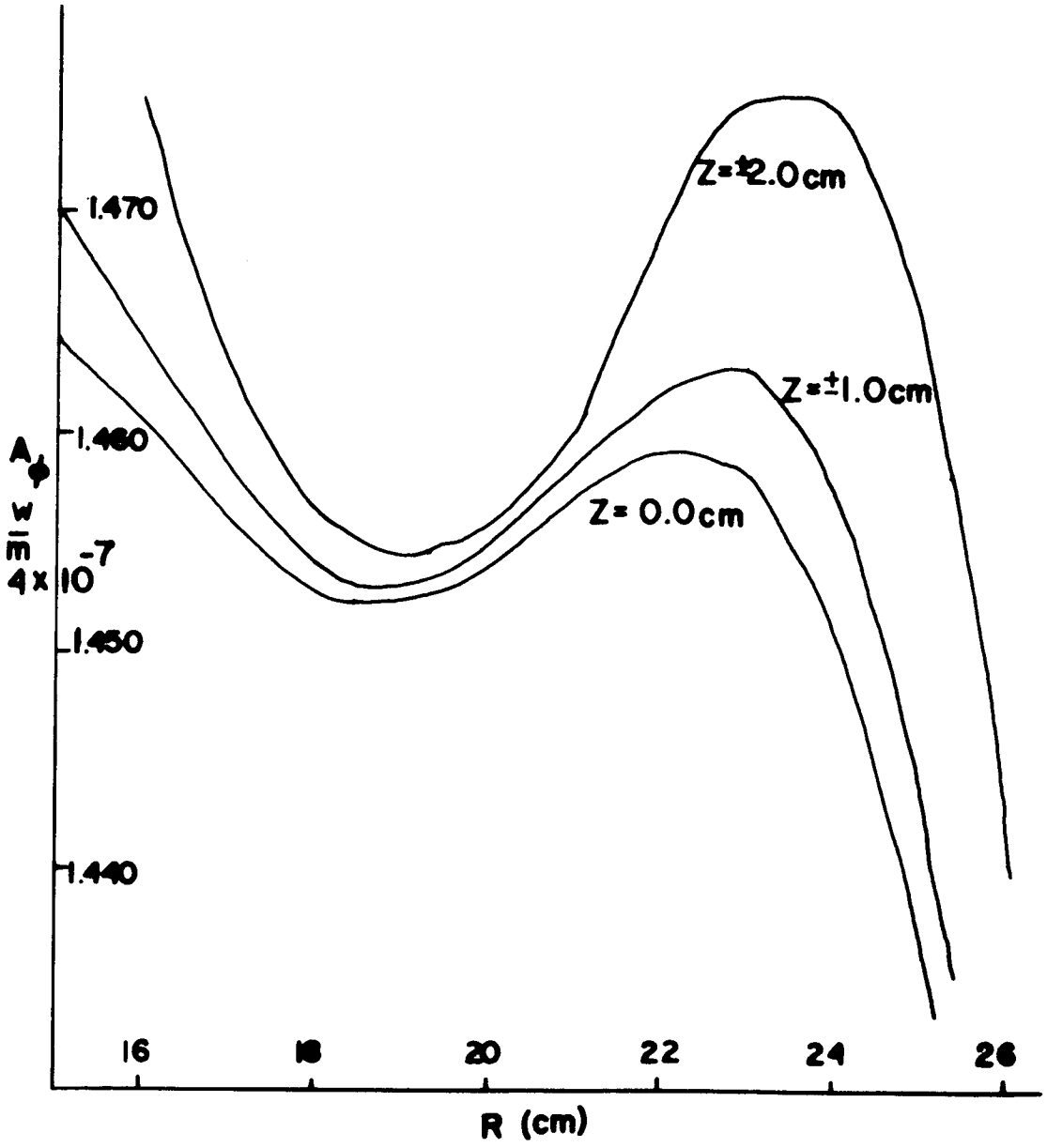
Z=±2.0cm
Z=±1.0cm
Z= 0.0cm
1.470
1.460
1.450
1.440
A_ϕ
$\bar{w}$
$\bar{m}$
4×10^{-7}
16
18
20
22
24
26
R (cm)

FIG. 2

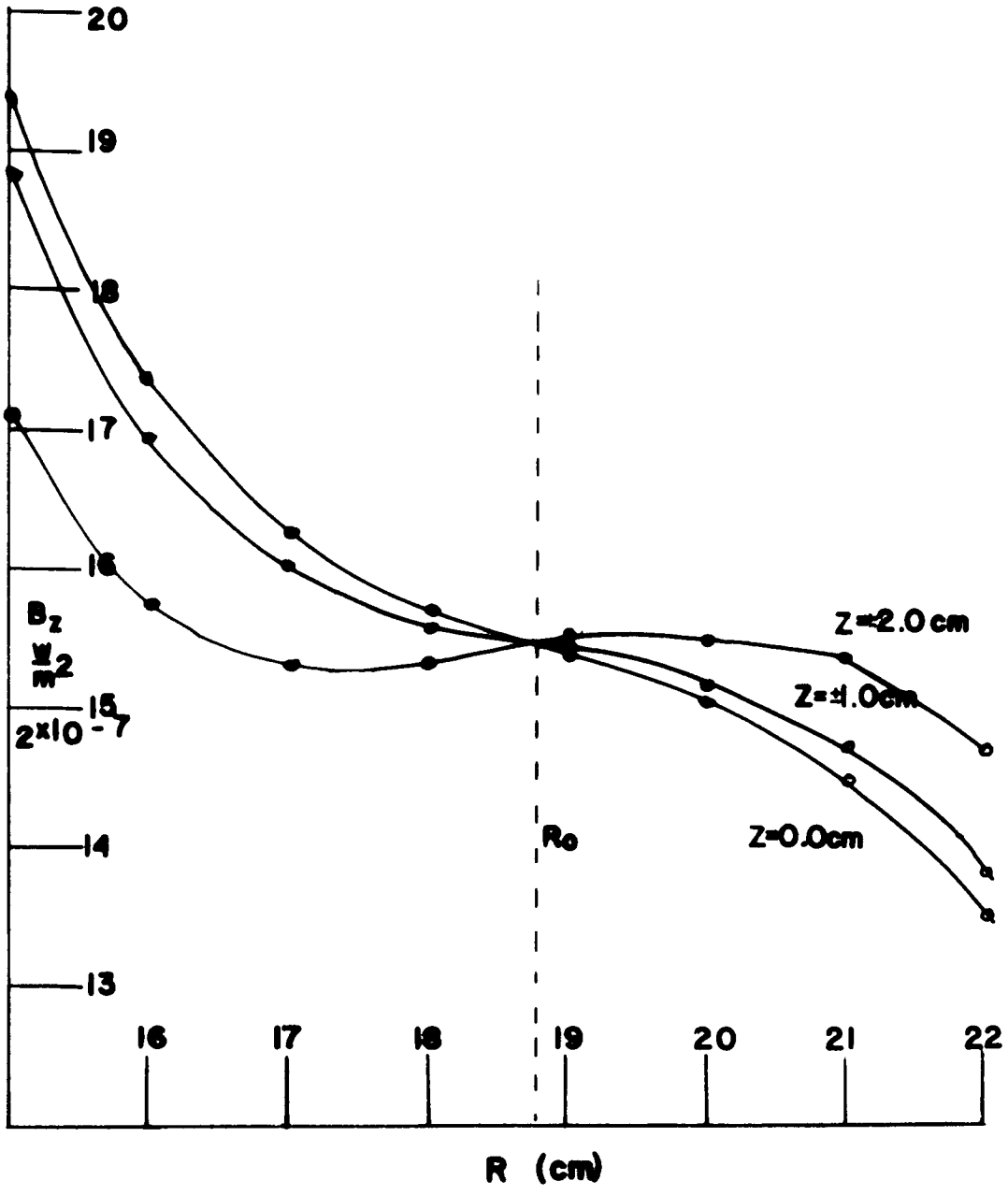
20
19
18
17
16
15
14
13
B_z
$\frac{w}{m^2}$
2×10^{-7}
Z=±2.0 cm
Z=±1.0cm
Z=0.0cm
R_o
16
17
18
19
20
21
22
R (cm)

FIG. 3

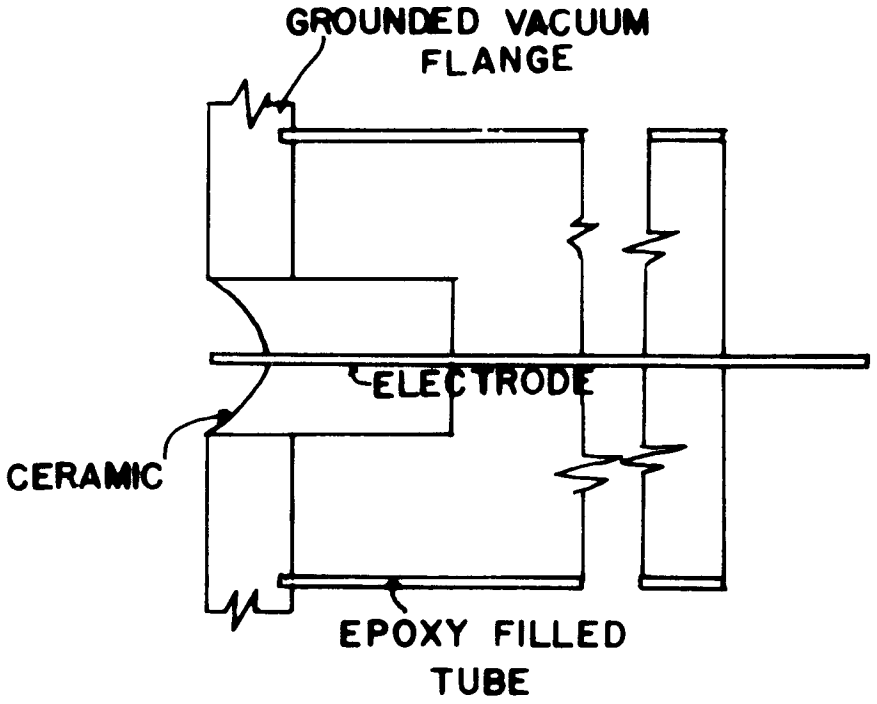
GROUNDED VACUUM
FLANGE
ELECTRODE
CERAMIC
EPOXY FILLED
TUBE

FIG.4

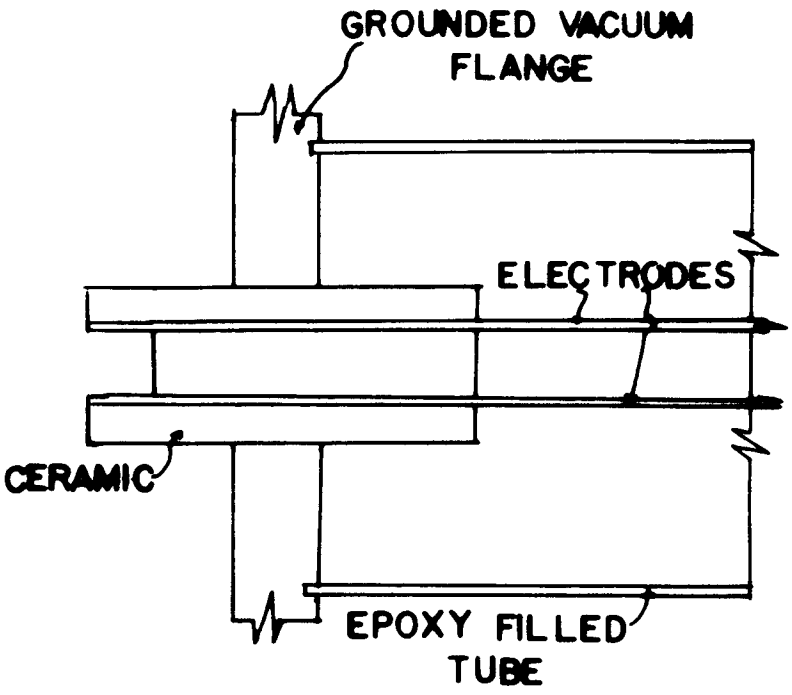
GROUNDED VACUUM
FLANGE
ELECTRODES
CERAMIC
EPOXY FILLED
TUBE

FIG. 5

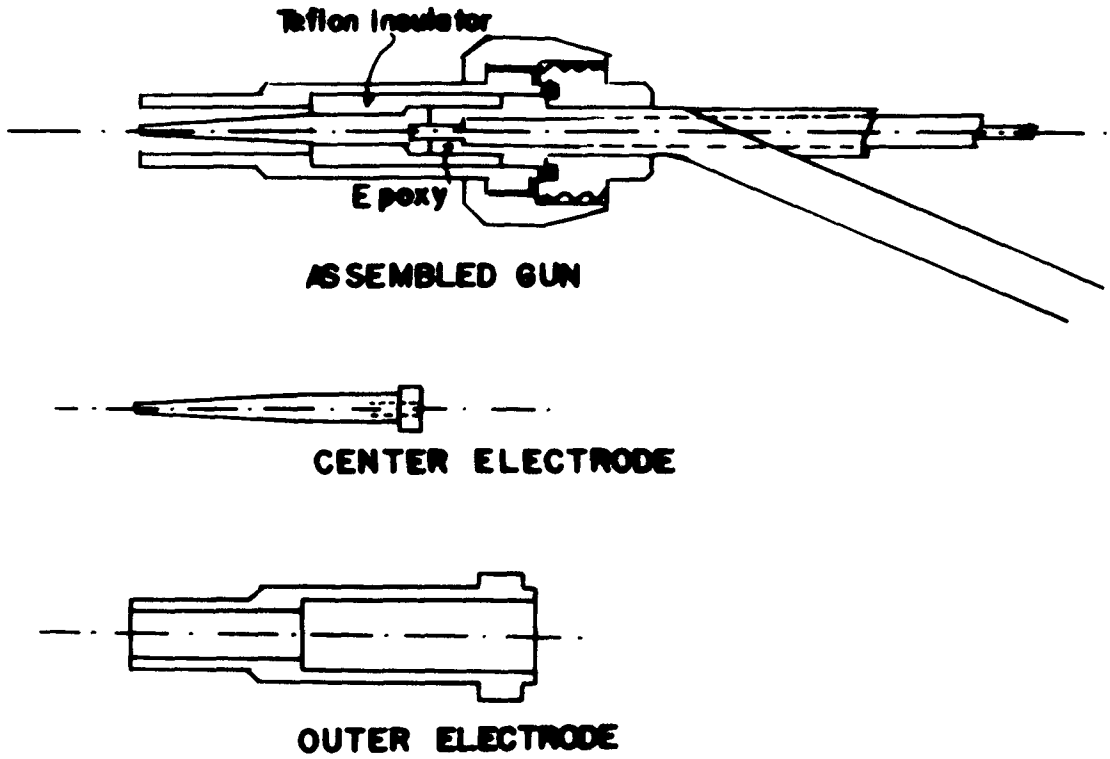
Teflon Insulator
Epoxy
ASSEMBLED GUN
CENTER ELECTRODE
OUTER ELECTRODE

FIG. 6

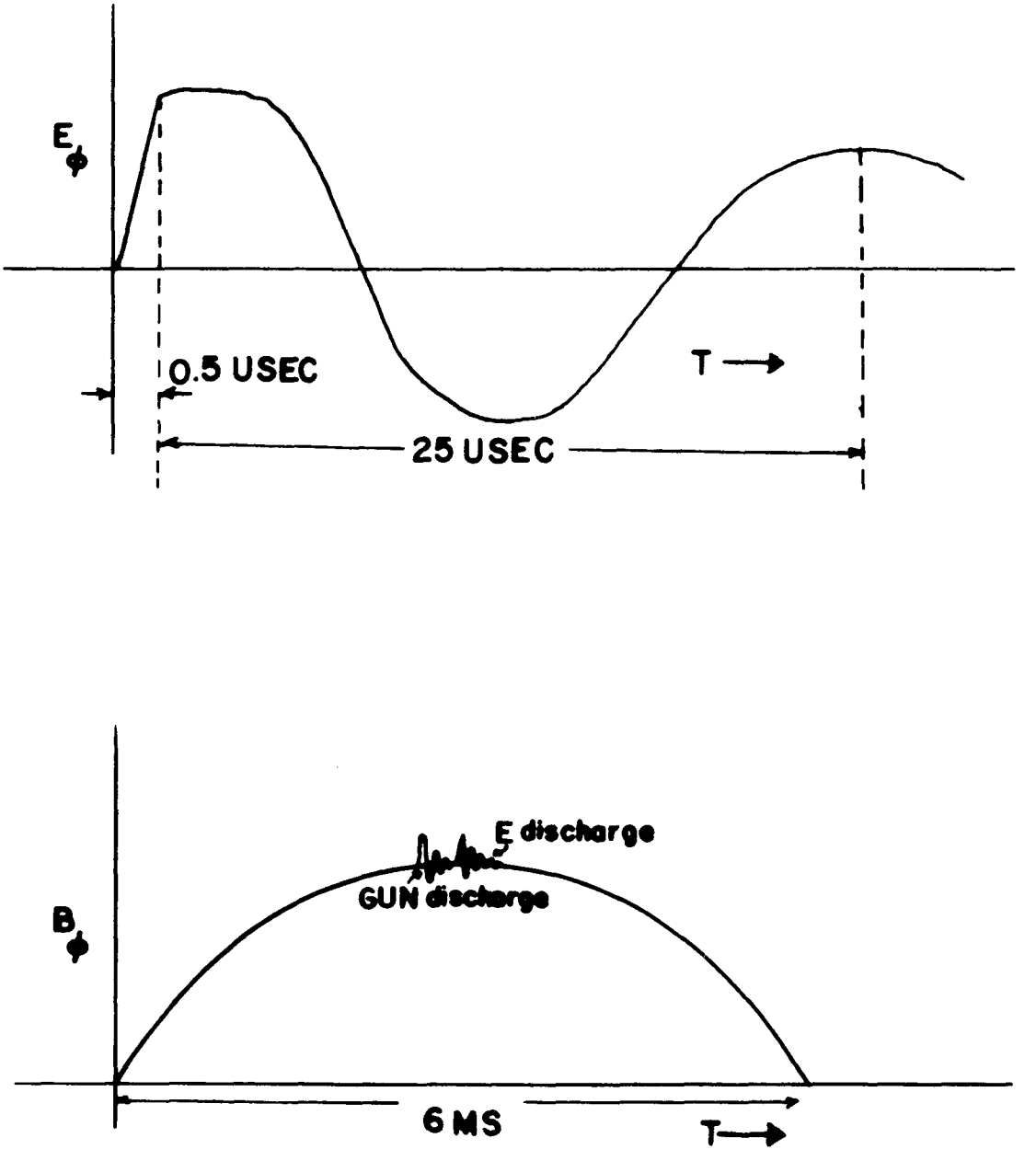

FIG. 7

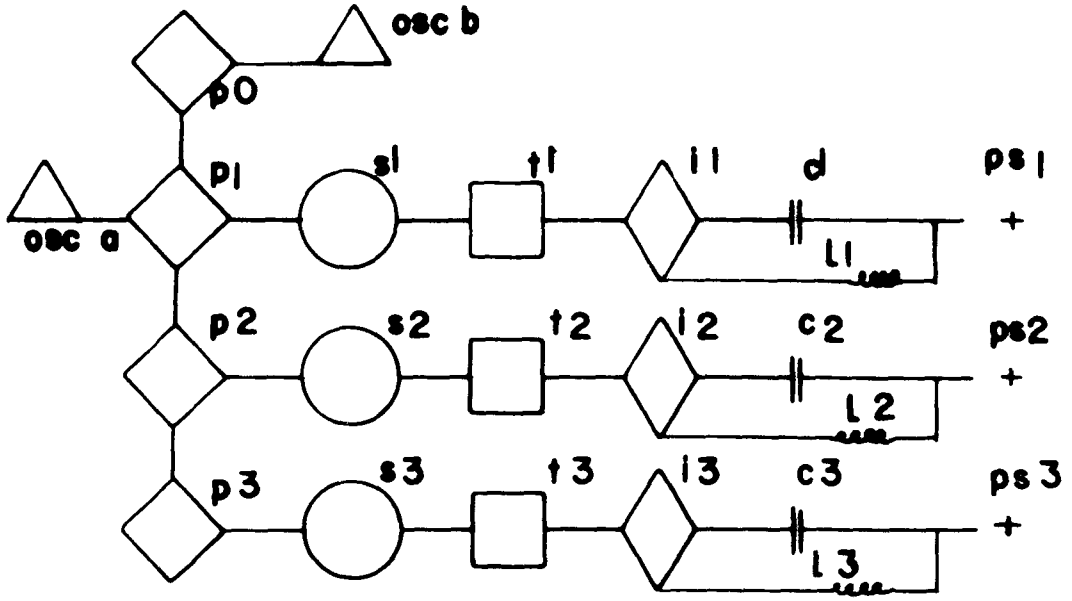
osc b
p0
p1
osc a
s1
t1
i1
d
ps1
+
L1
p2
s2
t2
i2
c2
ps2
+
L2
p3
s3
t3
i3
c3
ps3
+
L3

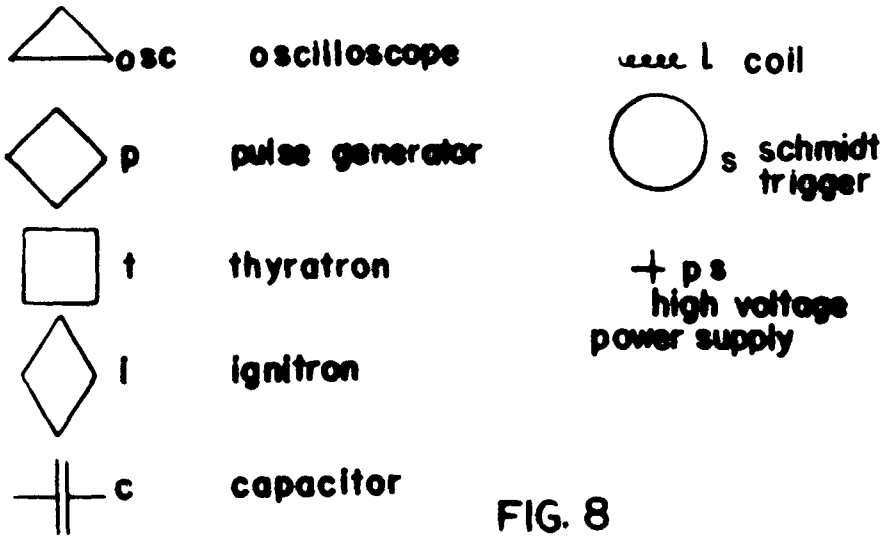
osc
oscilloscope
p
pulse generator
t
thyratron
i
ignitron
c
capacitor
l coil
s schmidt trigger
+ ps
high voltage power supply

FIG. 8

REFERENCES

CHAPTER III

1. H. M. Skarsgard and J. V. Gore, The Review of Scientific Instruments 36, 1807 (1965).
2. J. P. Blewett, Journal of Applied Physics 18, 968 (1947).
3. M. Abramowitz and I. A. Stegun, Editors, Handbook of Mathematical Functions (National Bureau of Standards, Applied Mathematics Series: 55, Ninth Printing, Nov. 1970, page 591).
4. R. H. Huddlestone and S. L. Leonard, Editors, Plasma Diagnostic Techniques (Academic Press, New York, 1965).
5. W. H. Bostick, Physical Review 104, 292 (1957).
6. H. de la Feunte and H. K. Forsen, The Review of Scientific Instruments 42,1453 (1971).
7. H. J. Goldschmidt, Interstitial Alloys (Plenum Publishing Corporation, New York, 1957, Chapter 9).
8. G. Schmidt, Physics of High Temperature Plasmas (Academic Press, New York, 1966).

CHAPTER IV

MEASUREMENT OF EXTERNAL FIELDS

From the calculations discussed in chapter III, it is known that in order to attain the properly shaped betatron field the current division between the inner coils and outer coils should be 1.000 to 0.775. Figure 1 shows the circuit used to try to determine the current distribution between the inner coils and outer coils. An external resistance, R_o, is placed in series with the outer coil, L_o. Similarly R_i, another external resistance, is placed in series with the inner coil, L_i. Using an approximately 100 KHz oscillator signal and measuring the voltage drops across R_i and R_o one obtains

$$\frac{I_i}{I_o} = \frac{V_i}{V_o} \frac{R_o}{R_i}$$

From this measurement it is found that

$$\frac{I_i}{I_o} = \frac{1.000}{0.7000}$$

This is in agreement with the apparant lack of a vector potential minimum as measured by a radial probe(to be discussed later in this chapter). In order to redistribute the current, small inductive coils are placed in series with the outer loops. The needed coil induction size is estimated to be approximately 0.1 microhenries.

The correction coil dimensions are 1.27cm long and 0.64cm in radius. Coils with four turns, six turns, and eight turns are constructed and tested with respect to achieving a vector potential minimum. Figure 2 shows the circuit used to measure the coil inductance. A known resistance, R, is placed in series with a variable frequency sine-wave generator and the coil to be tested. The coil impedance is given by $Z_{coil} = \frac{V_{coil}}{V_R} R$. By plotting Z^2_{coil} against the oscillator frequency squared (or Z_{coil} versus frequency) and determining the slope of this straight line, the coil inductance can be found. Frequencies from 0.1MHz to 2.0MHz are used. It is noted that any change in amplitude of the oscillator voltage is compensated for in this measurement. The measured inductance of the eight- and six-turn coils are approximately 0.42uh and 0.17uh. From this we can estimate the four-turn coils to have an inductance of about 0.1uh. The inductance of a single coil making up the betatron primary is approximately 1uh.

The experimental determination of $A_\phi(R)$ and $B_z(R)$ is carried out by two methods. The first method uses a radial probe. The ϕ (azimuthal) coordinate and Z (vertical) coordinate are fixed ($Z^{=0}$ is taken to be at the median plane, while ϕ is varied for different sets of radial measurements). The radial probe is composed of a .64cm

square nylon form wound with 100 turns of number 40 wire. This is mounted on a plexiglass ruled rod, which slides on a wood track. The assembly is designed so that the center of the pick-up loop is in the median plane.

In order to measure the field configuration, a large enough current must be sent through the betatron coils. Both a variable frequency oscillator and a power amplifier are used to produce a high frequency (50 KHz and 116 KHz) current of suitable amplitude. The probe voltage was first measured by means of Techtronix 551 oscilloscope using a Differential Comparator Amplifier-Type W plug-in unit. B_z was sampled at 1.00cm intervals from the common axis of the betatron coils and in the median plane. The value of B_z averaged over the area of the pickup loop, $\bar{B}_z$, is $\bar{B}_z = \frac{\mathcal{E}}{\omega A N}$ where $\mathcal{E}$ is the induced probe voltage, ω is the driving frequency, A is the probe loop area, and N is the number of turns in the probe. A_ϕ and B_z are related as follows:

$$\nabla \times \underset{\sim}{A} = \underset{\sim}{B}$$

Integrating this equation over the area of the median plane of radius R, $\int \nabla \times \underset{\sim}{A} \cdot d\underset{\sim}{A} = \int \underset{\sim}{B} \cdot d\underset{\sim}{A}$

or $\int \underset{\sim}{A} \cdot d\underset{\sim}{\ell} = \int B_z \, dA$

Since $\underset{\sim}{A}$ is azimuthaly symmetric and the total flux is Φ, we have that $A_\phi = \frac{\Phi}{2\pi R}$

One can calculate Φ from the $\bar{B}_z$ measurements by

dividing the area πR^2 into circular strips and calculating the average flux through each strip. The average flux through each strip is proportional to

$$(B_i + B_{i+1})(R^2_{i+1} - R^2_i)$$

and the total flux up to radius R_j is

$$\Phi(R_j) = \frac{\pi}{2} \sum_{i=0}^{j} (B_i + B_{i+1})(R^2_{i+1} - R^2_i)$$

and

$$A_\phi(R_j) = \frac{1}{4R_j} \sum_{i=0}^{j} (B_i + B_{i+1})(R^2_{i+1} - R^2_i)$$

When this was first attempted it was found that B_i could not be determined precisely enough using the differential comparator. This was due to the drift of the oscilloscope trace and amplitude fluctuations of the signal oscillator. The amplitude fluctuations were, in practical terms, eliminated by the use of a voltage line regulator connected between the power amplifier and the 120 volt a. c. line. The oscilloscope drift could not be eliminated, therefore two vacuum tube volt meters (V.T.M.) were used instead. One V.T.M. measures the induced voltage on a probe coil fixed near the center of the betatron, thereby monitoring any changes in the power amplifier output. The other V.T.M. is connected to the radial probe. These measurements allow determination of changes in A_ϕ to several tenths of a percent. It is found that the presence of the B_ϕ coils affect the shape of A_ϕ. Figure 3 shows the radial probe measurements of A_ϕ with all the B_ϕ coils in place for different size correction coils and at

two frequencies of the betatron field. Several different azimuthal positions are selected and the vector potential is remeasured. The vector potential dependence is found to be very similar. Using the radial probe measurements, the n values for the eight-turn correction coil are shown as a function of radial position in figure 4. One shortcoming of the radial probe technique is the fact that only regions between the azimuthal field coils can be sampled.

One can measure A_ϕ more directly by constructing circular loops of wire which lie in the median plane. The loops enclose magnetic flux, Φ, in an area of πR^2 and $A_\phi = \frac{\Phi}{2\pi R}$. The circular probe is constructed by milling out seven circular concentric grooves in a sheet of plexiglass and placing five turns of number 40 wire in each groove. The radii are 16cm, 17cm, 18cm, 19cm, 20cm, 21cm and 22cm. Using a V.T.M. and a high gain differential amplifier, the shape of the vector potential can be found by the following procedure: The voltage across one loop is used as a reference potential. The potentials across the other loops are subtracted from this reference potential, and from these differences and the reference potential value the shape of $A_\phi(R)$ can be determined. One has $A_\phi(R_i) = \frac{\Phi(R_i)}{2\pi R_i} = \frac{\mathcal{E}_i}{2\pi\omega R_i}$ and $A_\phi(R_o) = \frac{\mathcal{E}_o}{2\pi\omega R_o}$ where the subcript o refers to the reference potential, ω

is the signal frequency, $\mathcal{E}$ is the induced probe voltage, and R is the radial position. The change in A_ϕ from R_o to R_i is $\Delta A(R_i) = A_\phi(R_o) - A_\phi(R_i) = \frac{1}{2\pi\omega R_i}\left(\mathcal{E}_o - \mathcal{E}_i + \frac{i}{R_o}\mathcal{E}_o\right)$ The relative changes in A_ϕ, as measured with respect to the reference value, $\frac{\Delta A(R_i)}{A_\phi(R_o)}$, are plotted in figure 5. Data for the eight-turn and four-turn correction coil taken at 116KHz with the circular probe are shown. It is noted that the vector potential measurements using the eight-turn correction coil when carried out with the radial probe agree, qualitatively, with those done with the circular probe. The four-turn correction coil measurements appear to be in disagreement in that the radial probe measurements indicate a lack of vector potential minimum, while the circular probe indicates the presence of a minimum. This disagreement may be due to the changes in the vector potential created by the presence of the azimuthal coils and by the measurement error in the circular probe method.

The value of the azimuthal magnetic field at the equilibrium orbit is determined by using the same radial probe as in the vector potential measurement. The center of the probe is positioned at the equilibrium orbit position (assumed to be 19.0cm) with all the B_ϕ coils in place and connected to a 54uf capacitor. The capacitor is charged by a high voltage power supply and then dis-

charged by means of an ignitron switch. The induced probe voltage is integrated and displayed on the Techtronix 551 oscilloscope. The oscilloscope trace is photographed and from the measured voltage and probe dimensions it is determined that the B_ϕ value is

$$|B_\phi| = 0.68 \text{ kgauss/Kvolt}$$

so that a 1.0kilovolt voltage across the capacitor gives an equilibrium orbit B_ϕ of 0.68 kilogauss. The measured half period of the B_ϕ field is apprcximately 6 ms.

In a similar fashion the betatron magnetic field strength in the z-direction is found. Here a 10 uf capacitor is used. Utilizing the same 100-turn radial probe as above, it is found that the peak value of B_z at the equilibrium orbit is

$$|B_z| = 25.0 \text{ gauss/kvolt}$$

to within about ten percent. A ten-turn loop gives the value of 23.1 gauss/Kv, but this determination is not considered to be as precise as the above value due to the relatively large area subtended by the probe leads in the ten-turn loop compared to the 100-turn loop. A single loop of wire parallel to the azimuthal direction is also used. In this case the integrated induced voltage is proportional to the average magnetic field over the entire area of the equilibrium orbit. Half of this value is equal to the value of the betatron magnetic field at

the equilibrium orbit. These results are in approximate agreement with the radial probe results.

The time dependence of the vertical betatron field can be obtained by analyzing the induced voltage across the radial probe. One assumes that the primary circuit of the betatron (figure 6) is composed of a capacitor, C ; charged to an initial voltage, V_o ; a resistor, R ; and an inductance, L . When the switch, S , is closed, a current, I , flows in the primary. The mutual inductance, M , links the primary circuit to the secondary circuit which consists of the total plasma inductance, ℓ , and the total plasma resistance, r . The total plasma current is i . The coupled circuit equations are (figure 6)

primary $Q/C + IR + L\, dI/dt + M\, di/dt = 0$

secondary $ir + \ell\, di/dt + M\, dI/dt = 0$

where $Q = CV$ is the charge on the primary capacitor. The coupling constant, k is defined as

$$k \equiv \frac{M}{\sqrt{\ell L}}$$

and is a measure of how much of the primary flux passes through the secondary circuit. For two overlapping circuits occupying the same region of space k would be 1. We see that the $M \frac{dI}{dt}$ term in the secondary circuit equation is equivalent to a driving voltage term. By determining the electric field in the region of the equilibrium plane, as is described above, one can calculate the

the mutual inductance of the circuit by knowing dI/dt. From the L of the entire betatron circuit and the calculated l of the plasma column the coupling constant can be estimated. When no plasma is present the primary circuit obeys the equation[1]

$$\frac{d^2Q}{dt^2} + \frac{R}{L}\frac{dQ}{dt} + \frac{Q}{C} = 0$$

Assuming $Q = Q_0 e^{pt}$ one finds that $p = -\gamma \pm i\omega$

where $\gamma = R/2L$ and $\omega = \sqrt{\frac{1}{LC} - \left(\frac{R}{2L}\right)^2}$

Thus $Q = Ke^{-\gamma t}\cos(\omega t - \phi)$ where $K = CV_0\frac{\sqrt{\gamma^2+\omega^2}}{\omega}$ and $\tan\phi = \gamma/\omega$

This gives $dI/dt = K' e^{-\gamma t}\cos(\omega t - \phi')$

where $K' = (\omega^2+\gamma^2)K$ and $\phi' \cong \phi - \frac{2\gamma}{\omega} \cong -\frac{3\gamma}{\omega}$

The expression for ϕ' uses the fact that $\gamma << \omega$, as will be shown.

As mentioned above, the integrated induced voltage across the radial probe is proportional to E_ϕ, which in turn is proportional to dI/dt. Therefore, by plotting log E_ϕ as a function of time for the peak E_ϕ values ($\frac{d}{dt}(\frac{dI}{dt}) = 0$), one can determine γ. The frequency is obtained by averaging the zero crossing times. From this one gets $\omega = 2.52\times10^5 \pm 0.05\times10^5 \frac{rad}{s}$ and $\gamma = 1.15\times10^4 \pm 0.05\times10^4 s^{-1}$. Thus one computes L and R to be

$L = 3.2\times10^{-6}$ henries and $R = 0.077$ ohms.

Using a bridge circuit it is found that the d.c. resistance of the four betatron coils alone is 0.052 ohms. To estimate the mutual inductance it is assumed that

$V = M\frac{dI}{dt} \cong V_o \cos\omega t$ where $V_o = I_o \omega M$

Referring back to figure 6, one sees that when S is closed, C can be considered as a voltage source for L and R. In general, the current and voltage in the circuit can be represented as Fourier integrals[2]

$I(t) = \frac{1}{2\pi}\int I_\omega e^{i\omega t} d\omega$ and $V(t) = \frac{1}{2\pi}\int V_\omega e^{i\omega t} d\omega$

Fourier analysing the circuit equation

$$V = IR + L\frac{dI}{dt}$$

and noting that $I = 0$ at $t = 0$ one finds that

$$V_\omega = Z_\omega I_\omega \quad \text{where} \quad Z_\omega = R + i\omega L .$$

In this case it is assumed that $I(t)$ and $V(t)$ are composed of one Fourier component, that is, the primary circuit is nearly sinusoidal. For $V_o = 6.05\times10^3$ volts and $Z = \sqrt{\omega^2 L^2 + R^2} = 0.81$ ohms one gets $I_o = \frac{V_o}{Z}$ $= 7.4\times10^3$ amps. The measured electric field strength is 7.0 volts/cm. Thus the induced voltage in the secondary is

$$V_s = \oint \underset{\sim}{E}\cdot d\underset{\sim}{\ell} = 2\pi R_o E = 8.4\times10^2 \text{ volts}$$

The mutual inductance is found to be $M = 4.5\times10^{-7}$ henry and the coupling constant is $k = 0.34$. The value of the secondary inductance is found from the expression[2] $\ell_{emu} = 4\pi b\left(\log\frac{8b}{a} - \frac{7}{4}\right)$. Assuming that the secondary current column has the following dimensions:

b = major radius = 19.0 cm and a = minor radius = 2.50 cm. It also must be assumed that the current is uniformly distributed through the vacuum chamber.

CHAPTER IV

FIGURE CAPTIONS

Figure	Page	Caption
1	67	Circuit Used for Current Distribution Measurements
2	68	Circuit Used for Coil Inductance Measurement
3	69	Measured Variation of $A\phi$ Versus Radial Position via Radial Probe
4	70	Field Index in Median Plane as a Function of Radial Position
5	71	Relative Vector Potential Versus Radial Position via Circular Probe
6	72	Equivalent Circuit For Plasma Betatron

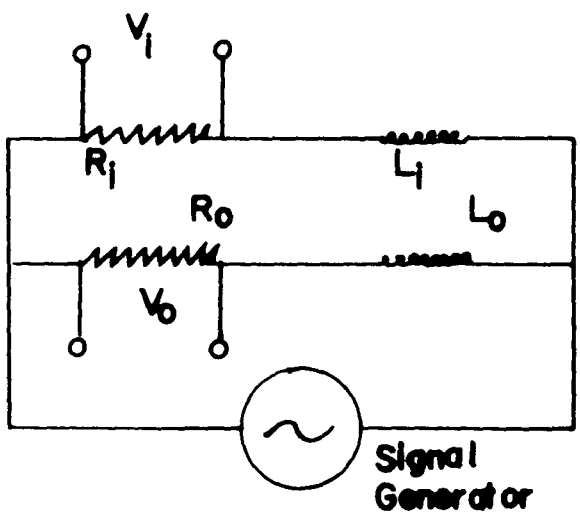

FIG. 1

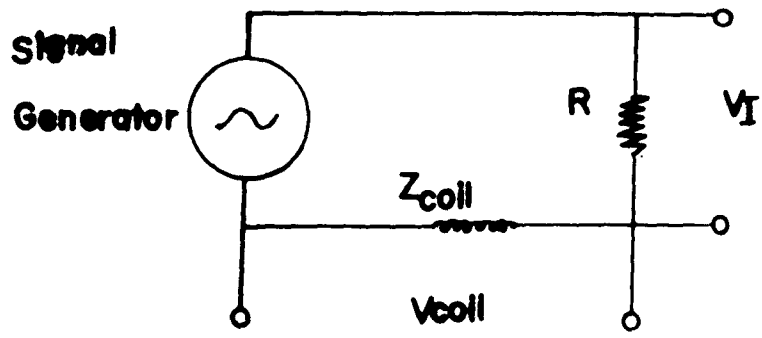

FIG. 2

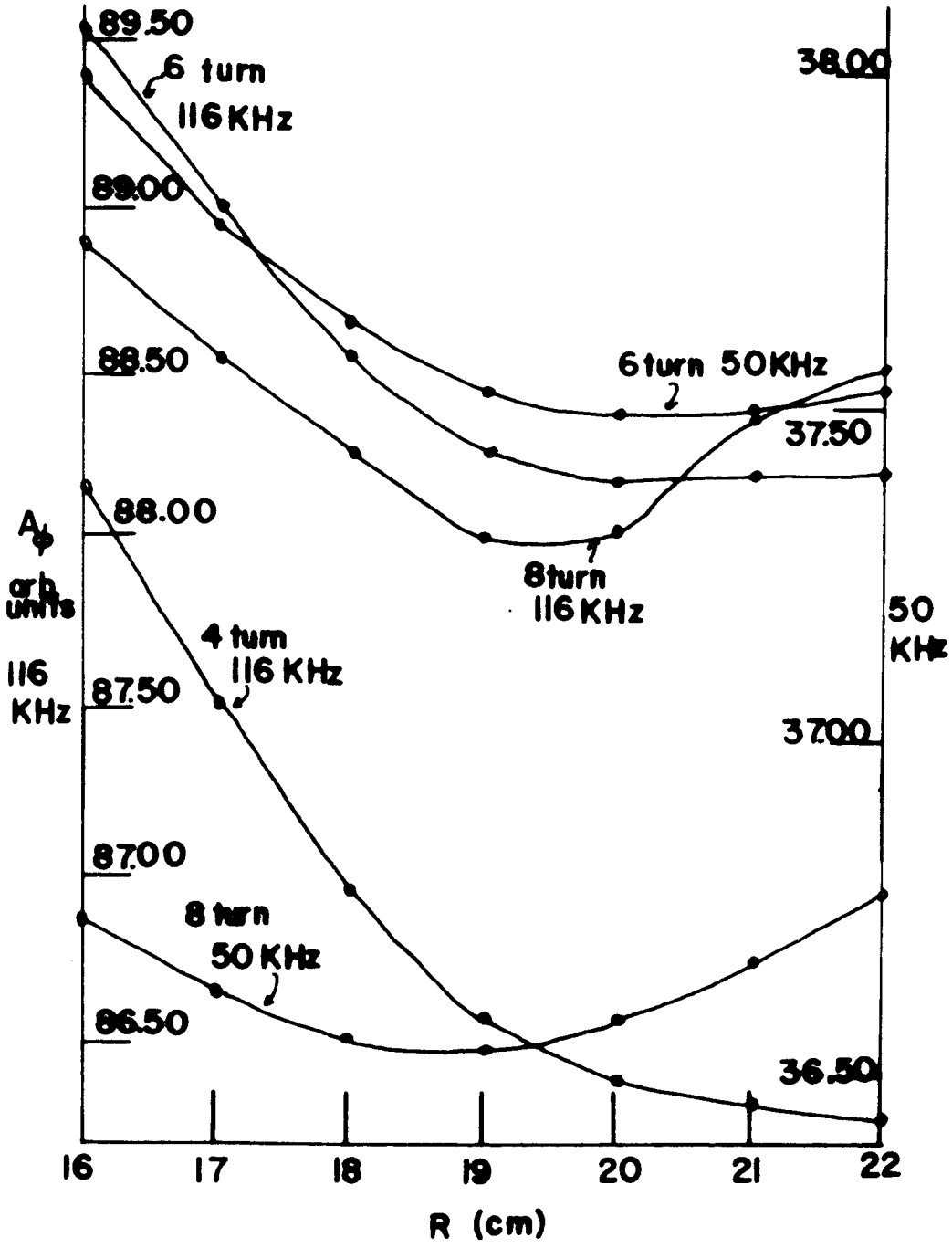
89.50
6 turn
116 KHz
38.00
89.00
88.50
6 turn 50 KHz
37.50
88.00
8 turn
116 KHz
A_ϕ
arb units
116 KHz
4 turn
116 KHz
87.50
50 KHz
37.00
87.00
8 turn
50 KHz
86.50
36.50
16
17
18
19
20
21
22
R (cm)

FIG. 3

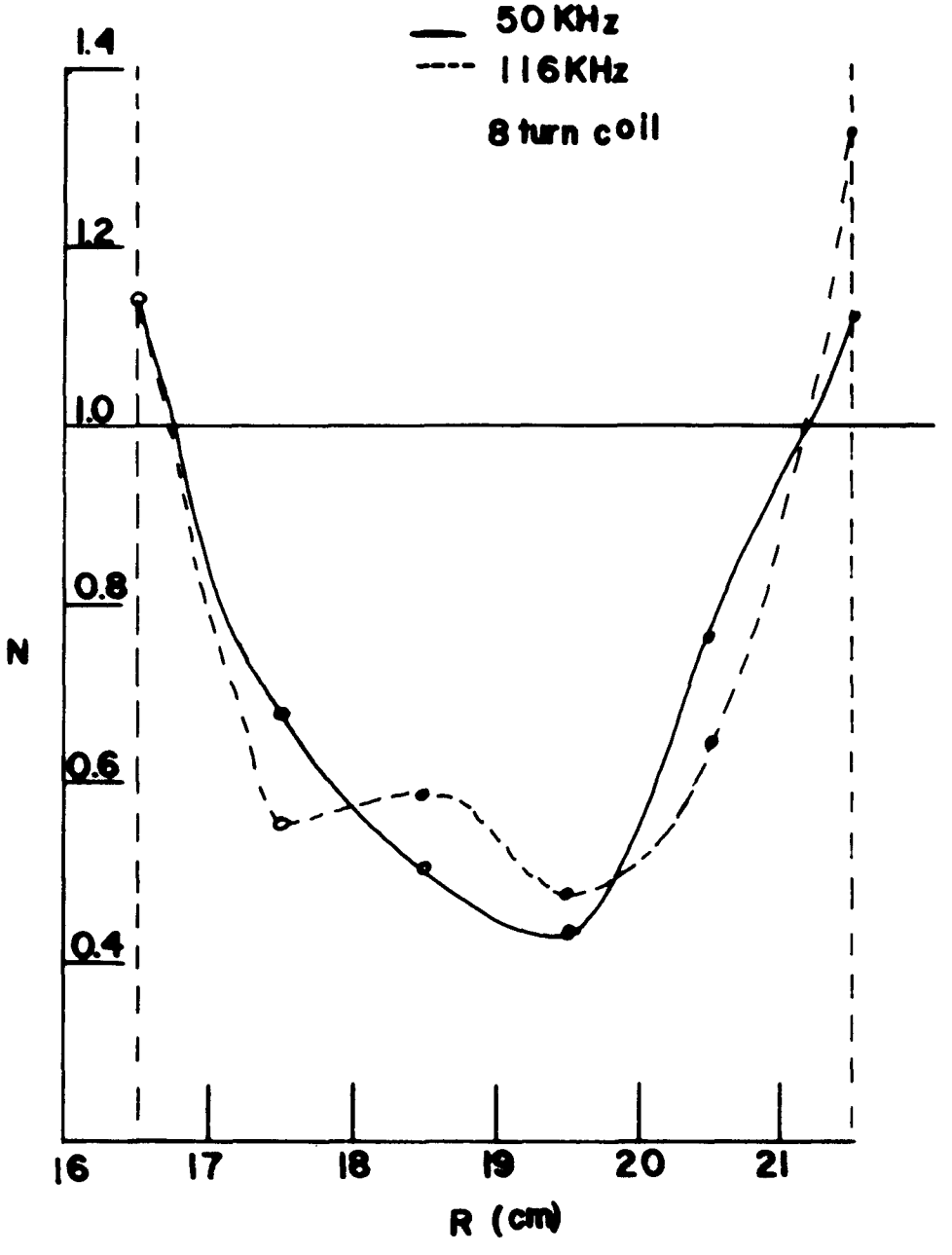

FIG. 4

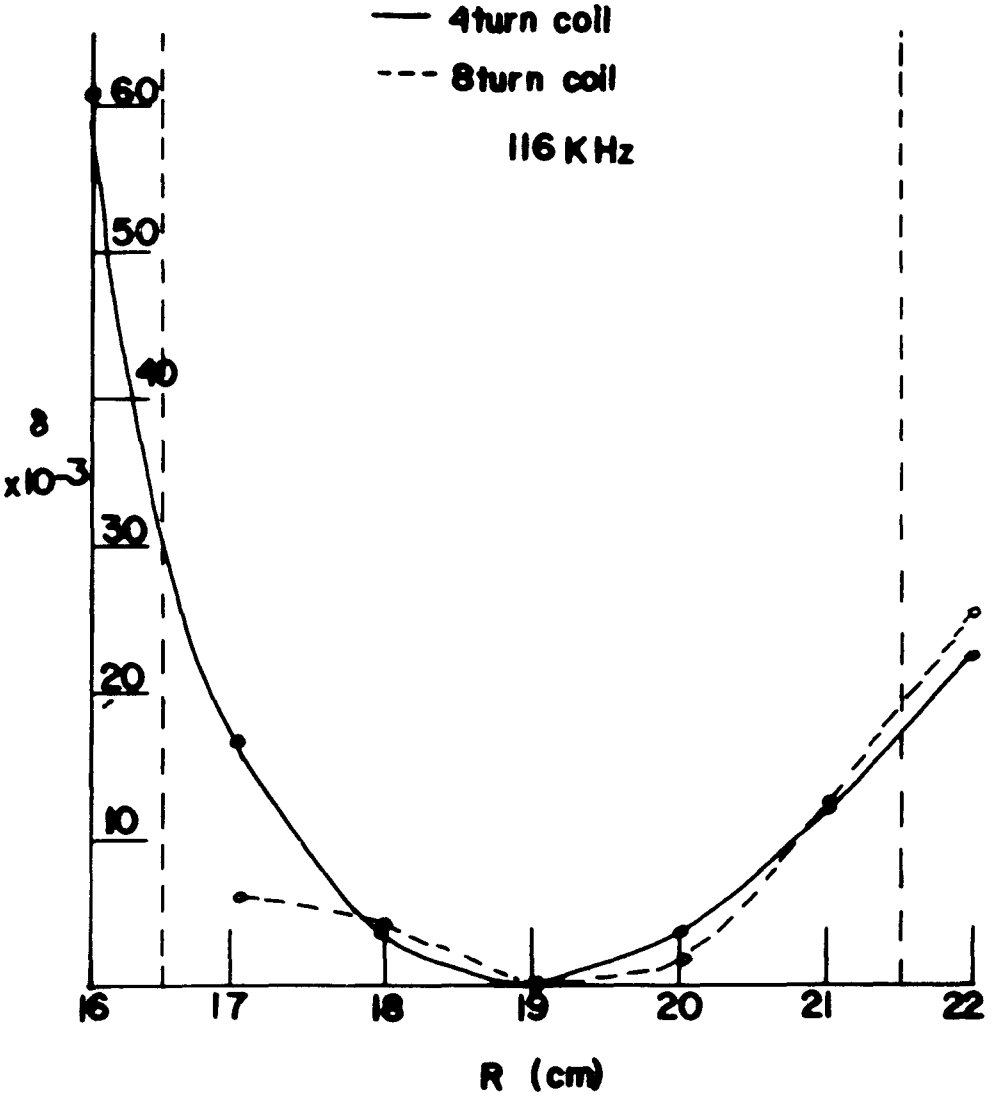
4turn coil
8turn coil
116 KHz
60
50
40
δ
x10-3
30
20
10
16
17
18
19
20
21
22
R (cm)

FIG. 5

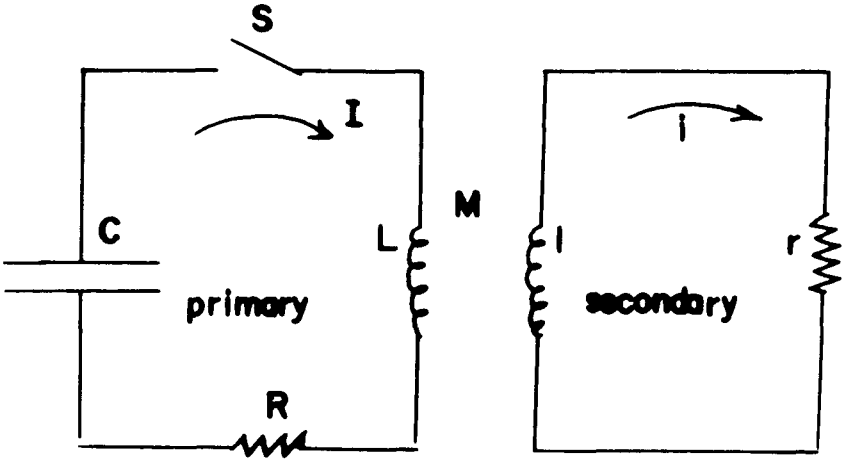

FIG.6

REFERENCES

CHAPTER IV

1. E. M. Pugh and E. W. Pugh, Principles of Electricity and Magnetism (Addison-Wsley Publishing Company, Inc., Massachusetts,1962)
2. L. D. Landau and E. M. Lifshitz, Electrodynamics of Continuous Media (Pergamon Press, New York, 1966)

CHAPTER V

PLASMA DIAGNOSTICS

In this section those techniques used to measure plasma parameters are discussed. Langmuir probes[1] have been designed and constructed to measure the density and temperature of the plasma formed in the toroidal vacuum chamber. The probes are also used to find the plasma density as a function of radial position, that is, the density profile. These measurements are averaged over several cycles. This is necessitated by the shot-to-shot variation in the discharges. Because the betatron uses a glass vacuum chamber, the chamber wall does not act as a good reference potential; therefore, instead of using a single element Langmuir probe, a floating Langmuir probe is used in which two electrodes are placed into the plasma. A potential difference is placed between the two electrodes and current is drawn through the probe. The current drawn depends on the applied voltage and the number of charged particles approaching the electrode surface. The latter depends on the probe area, the plasma density and the plasma temperature. Figure 1 shows a cutaway view of a

typical Langmuir probe used. Both Nichrome and tungsten wires are used for the electrodes. Double bore alumina (re-cyrstalized aluminum oxide) is used to hold the electrodes in place. The electrode area exposed to the plasma is approximately $0.01cm^2$. The smallest electrode separation used is 0.013cm while the largest is approximately 0.076cm.

In order to measure the current drawn by the probe when a voltage, V_o, is applied between the electrodes, a resistor is placed in series with the probe electrodes as shown in figure 2. The voltage, V_o, is supplied by a 5uf capacitor, C, charged from -200v to +200v by means of a 240 volt Eveready number 241 dry cell. The voltage across the $2.2x10^2$ ohm resistor is determined by the use of a one-to-one isolation transformer and an oscilloscope terminated by a 1000 ohm resistor. The purpose of the isolation transformer and the battery is to avoid direct conduction from the gun discharge through the probe ciruit. Several pulse transformers[2] were designed and tested. The response to a square wave pulse of height, V, has been observed in testing the different transformers that were built. Little droop is required for about a 100usec pulse width, while rise times of 1 usec or less with little overshoot is also required. A 5.04cm by 3.49cm lamenated core

(Arnold Engineering number A12) is used. Eighty turns of number 40 copper wire in both the secondary and the primary are first wound onto a paper form (a section of a computer punch card) which than fits snuggly onto the core. It is found that the turns should be as close to each other as possible and that each turn has to be placed adjacent to the next turn rather than wound in an overlapping manner. This technique permits the construction of a fast rise time (1 usec) and efficient (greater then 90 percent efficiency for 160 usec wide pulses) pulse transformer. The overall distortion of the calibration square wave is small.

The 1000 ohm terminator is found to give the best performance characteristic of the transformer circuit with respect to the square wave calibration pulse. The relation between the voltage across the probe, V , and the probe circuit current, I , is $V = V_o - IR$ where V_o is the voltage applied by the battery. The voltage drop, IR, is measured by the oscilloscope and shown as V_s in figure 2. A less than ten percent correction must be made for the transformer efficiency. By plotting I versus V , a so-called I-V characteristic is obtained. The electron temperature is found from

$$kT_e = \frac{1}{2}\frac{eI_+}{(dI/dV)_o}$$

where kT_e is the electron temperature, e is the electronic charge, I_+ is the ion saturation current, and $\left(\frac{dI}{dV}\right)_o$

is the slope of the I-V characteristic at the origin. The plasma density is given by

$$n \cong \frac{I_+}{0.4\,A\left(\frac{2kT_e}{m_+}\right)^{1/2}}$$

where A is the electrode area and m_+ is the ion mass. If one assumes that the plasma temperature is approximately constant, than $n = KI_+$ where K is a constant. For large enough probe voltage, V_o, which is about 150v for these experiments, the measured I is just I_+ which is proportional to n. Thus by maintaining V_o at one value and placing the probe at different radial positions, a relative density profile can be obtained. In a similar manner the Langmuir probe ion saturation current signal can give a picture of the relative density as a function of time at one point in the plasma. When using one probe for this type of measurement it must be assumed that the plasma column is stationary (or that it is moving in a known way) and that the temperature is constant (or that it is changing in a known way). Chapter 6 shows typical ion saturation curves. It is noted that a low frequency band pass filter is used to clarify the low frequency time dependence of the ion saturation curve. Higher freqency components can also be observed.

The plasma density averaged over the radial cross section of the plasma column can be determined by means of

a microwave interferometer[3]. A microwave beam, transported by a rectangular waveguide, is split into two beams. One beam passes through the vacuum chamber and recombines with the other beam, called the reference beam. When no plasma is in the vacuum chamber the phase of the two beams is adjusted so that they recombine and produce a minimum intensity at the detector position. The introduction of a plasma, with density $n(r)$, into the vacuum chamber produces a phase shift, $\Delta\phi$, between the two beams given by

$$\Delta\phi = \int_0^{2a} \left\{ 1 - \left(1 - \frac{n(r)}{n_c}\right)^{1/2} \right\} \frac{2\pi}{\lambda} dr$$

This neglects refraction and reflection effects.

Consider a plane wave of frequency ω, with wave vector $\underset{\sim}{k}$ perpendicular to the external field, $B\phi$. The wave passes through a plasma in which the collision frequency is small compared to ω and the electron thermal velocity is small compared to $\omega/|\underset{\sim}{k}|$. Then the index of refraction, $\mu(r)$, is given by

$$\mu(r) = \sqrt{1 - \frac{\omega_p^2(r)}{\omega^2}}$$

where ω_p is the electron plasma frequency given by

$$\omega_p = \sqrt{\frac{4\pi n e^2}{m_e}} \quad \text{(c.g.s)}$$

The critical density, n_c, occurs when n increases to such a value that $\omega = \omega_p$ or $n = n_c = \frac{\omega^2 m_e}{4\pi e^2}$.

The total phase shift, $\Delta\phi$, depends on the signal

free space wave length, λ , the length of the plasma traversed by the microwave beam, L , and the density distribution. By assuming certain functional forms for $n(x)$, one can predict the maximum phase shift that can be observed. If $n_0(t)$ is the maximum density reached, for a symmetric distribution of rectangular, triangular, parabolic, and trapezoidal form, the phase shift is

$$\Delta\phi(x) = \frac{2\pi}{\lambda}\left(L - I(t)\right)$$

where $I(t)$ depends on the particular distribution. The values of $I(t)$ corresponding to these distributions are

rectangular $\quad I_R(t) = L\left(1 - n_0(t)/n_c\right)^{1/2}$

triangular $\quad I_t(t) = L\,\frac{2}{3}\frac{n_c}{n_0(t)}\left(1 - \left(1 - \frac{n_0(t)}{n_c}\right)^{3/2}\right)$

parabolic $\quad I_p(t) = \frac{L}{2}\left\{1 + \sqrt{\frac{n_0(t)}{n_c}}\left(\frac{n_c}{n_0(t)} - 1\right)\log\left[1 + \sqrt{\frac{n_0(t)}{n_c}}\right]\right\}$

trapezoidal $\quad I_{tr}(t) = L\,\frac{2}{3}\left(1 - \frac{a}{L}\right)\frac{n_c}{n_0(t)}\left[1 - \left(1 - \frac{n_0(t)}{n_c}\right)^{3/2}\right] + a\left(1 - \frac{n_0(t)}{n_c}\right)^{1/2}$

where a is the length of the flat top in the trapezoid distribution. At cutoff the phase shift is a maximum. The values of $\Delta\phi$ in that case are

rectangular $\quad \Delta\phi_R = 2\pi L/\lambda$

triangular $\quad \Delta\phi_t = 2\pi\,\frac{1}{3}L/\lambda$

parabolic $\quad \Delta\phi_p = 2\pi\,\frac{1}{2}L/\lambda$

trapezoidal $\quad \Delta\phi_{tr} = 2\pi\left[1 - \frac{2}{3}\left(1 - \frac{a}{L}\right)\right]L/\lambda$

When the two microwave beams are recombined and the initial phase is adjusted for a minimum, the relationship between the time average intensity of the combined beams,

$\langle I(t) \rangle$, the time average intensity of the transmitted beam, $\langle I_x(t) \rangle$, the time average intensity of the reference beam, $\langle I_R \rangle$ (which should be the value of $\langle I(t) \rangle$ at cut-off), and the phase shift $\Delta\phi(t)$, is

$$\langle I(t) \rangle = \langle I_R \rangle + \langle I_x(t) \rangle - 2\sqrt{\langle I_R \rangle \langle I_x(t) \rangle} \cos[\Delta\phi(t)]$$

The quantities $\langle I(t) \rangle$ and $\langle I_x(t) \rangle$ are measured as a function of time. $\langle I_R \rangle$ is found from the cut-off value of $\langle I(t) \rangle$. In order to determine the average intensities, silicon diodes are used. The voltage output of the diodes must be calibrated as a function of input power. A thermistor is used to measure the input power level.

The total azimuthal current is measured by means of a Rowgoski coil, which is a solenoid bent into the shape of a circle. The current to be measured passes through the inner part of the coil. The current size is related to the major cicumference,[4] the area of a single turn of the solenoid, A, the number of turns, n, and the flux passing through the windings, Φ, as

$$I = \frac{c}{4\pi} \frac{S\Phi}{nA}$$

It is assumed that the coils are evenly spaced and that the magnetic field strength variation across each coil is small. By using an integration network, the induced voltage across the Rogowski coil, which is proportional to $\frac{d\Phi}{dt}$, can be used to determine Φ. Knowing the coil dimensions, I, can then be found.

A seventy-turn Rogowski coil was constructed using number 36 copper wire. The major radius is 3.81cm while the minor radius is 0.081cm. The loops of wire are wound on thin tubing (wire insulation). The loops are formed into an evenly spaced helix by a second tube placed over the thin tube. The outer tube has a helical groove cut through it so that the loops of wire are held in place by the sides of the groove and the top surface of the thin tubing. The coil is mounted around the minor diameter of the Pyrex vacuum chamber and aligned to minimize pickup due to the B_z field. The sensitivity of this coil, with the integration network used, is

14 amps/mv

A second Rogowski coil was constructed to help subtract the betatron field pickup. Currents as small as 5 amperes can be readily measured by amplifying the operational amplifier output and enlarging the oscilloscope trace photographs. A limitation to the measureable output voltage has been due to the lack of a more precise location of the voltage null of the operational amplifier which is due to a drift in the operational amplifier output signal. The measured inductance and resistance of the Rogowski coil plus bucking coil were measured to be 1.6uh and 0.8ohms, respectively.

The measurement of the vacuum electric field was described in chapter IV. To follow the time dependence of E when an azimuthal current is present, a small Rogowski coil is placed around the cable which carries current to the betatron coils. This allows elimination of pickup due to the azimuthal current flow caused by the small size of the coil and its relative distance from the vacuum chamber.

The neutral pressure of the gas is measured by means of a Bayard-Alpert ion gauge tube[5] and a thermo-couple gauge tube. Since the pressure gauges are normally located near the vacuum pump, it is necessary to determine the pressure at other regions in the vacuum system. Gauges are placed on the opposite end of the vacuum chamber and from the combined measurements at each end of the vacuum chamber estimates of the neutral pressure in the region of plasma formation are determined. Correction for the gas molecule type, due to differences in ionization efficiencies, is also required. Using the thermocouple gauge is necessary for neutral pressure measurements when hydrogen discharges are being studied. This results in a less accurate neutral pressure determination (50percent versus 10 percent). Rather than relying on the thermo-couple gauge reading, a calibrated leak (a gas inlet with known aperature) is used to provide a constant neutral density for

hydrogen.

X-ray emission is detected by using a sodium iodide cyrstal as a scintillator and a photomultiplier as a scintillator detector and photon-to-voltage converter. The first photomultiplier tube used for X-ray emission time studies was a R.C.A. 6810-A which has a sensitivity of 2.4×10^6 amps/watt. The time between the start of the electric field and the start of the X-ray emission for the first quarter cycle in argon and hydrogen is measured. For hydrogen some measurements have been taken for X-ray emission occuring at different cycles. The energy of the X-rays is estimated by using different thicknesses of aluminum in front of the photomultiplier.[6] The X-ray intensity, I, attenuates as $I(x) = I_o e^{-\mu_o x}$ where I_o is the initial X-ray intensity at $x = 0$, x is the thickness of the absorber, and μ_o is the total linear attenuation coefficient. By plotting the $\log I$ versus x the value of μ_o can be found. Tables or graphs are available which show μ_o divided by the density of the absorber material as a function of the X-ray energy corresponding to the mass attenuation coefficient. A second photomultiplier tube, a R.C.A. 6342-A, having a sensitivity of 2.5×10^4 amp/watt is used as a reference to measure I_o for each measurement of $I(x)$.

This helps to take into account the shot-to-shot variation in I_o . Various arrangements of lead bricks are used to try to collimate the X-ray emission.

The radial distribution of the azimuthal current can be determined by the use of a magnetic field probe[4] inserted into the plasma current column. A small plexiglass form is wound with 20 turns of number 40 copper wire. The loop has a radius of 0.051cm. The coil fits snuggly, 0.25cm from the capped end of a quartz tube of 0.325cm outer diameter. A second coil is used to "buck out" the external B_z field. Additional corrections for stray pickup can be made by subtracting, point by point, the pickup signal from the observed signal. Again, the oscilloscope traces are photographed and these photographs are enlarged by use of an overhead projector. These enlargements are broken up into a rectangular grid to determine the value of the voltage at different times. A convenient way to do this is to superimpose the enlargements on millimeter graph paper by the use of a ground glass plate. A light is placed behind the glass and the curves to be superimposed on the other side of the glass. Using the light box and millimeter graph paper, it is easy to produce a 0.01cm resolution of the original oscilloscope scale.

The sensitivity of this probe and the integrating net-

where a is the radius of the current column and x is the distance from the center of the distribution. An estimate of the effect of the bending of the current column into a torus on the B_θ , x dependence, is obtained by assuming the following: The bending causes a fixed amount of magnetic flux, Φ_o , present in the cylindrical geometry to be compressed into a smaller area on the concave side of the bend and thinned out on the convex side of the bend. Figure 3 shows the geometry in the median plane. Consider the magnetic flux in a ring of area

$2\pi R\,dR$, $\Phi_o = 2\pi R\,dR\,B(R)$ or $B(R) = \frac{\Phi_o}{2\pi R\,dR}$

In particular, consider two points R_1 and R_2 , equidistant from the center of the current distribution, R_o . That is, $R_o - R_1 = R_2 - R_o \equiv |x|$

It is assumed that Φ_o is the same in these regions but the area is changed, i.e.,

$B(R_1) = \frac{\Phi_o}{2\pi R_1\,dR}$ and $B(R_2) = \frac{\Phi_o}{2\pi R_2\,dR}$

Thus $\frac{B(R_1)}{B(R_2)} = \frac{R_2}{R_1}$

Let B be the magnetic field strength in the straight cylinder geometry at the position $|x|$. It is further assumed that $B = \frac{1}{2}\left(B(R_1) + B(R_2)\right)$. Using this expression, and the previous ratio of the magnetic field strengths at R_1 and R_2 , one obtains

$$B(R_1) = \frac{2R_2}{R_1+R_2}B \; ; \quad B(R_2) = \frac{2R_1}{R_1+R_2}B$$

Letting $R = R_0 + x$ one has $B_\theta(x) = B_\theta(1 - x/R_0)$

where $$B_\theta = \frac{2I}{c}\left\{ \begin{array}{l} \frac{|x|}{a^2}, \; |x| \le a \\ \frac{1}{|x|}, \; |x| > a \end{array} \right\}$$

Here a is the minor radius of the current column. This approximation is close to that of other authors[7] who evaluate B_θ outside of the current column by solving for the magnetic potential ϕ_m, where $\underset{\sim}{B} = \nabla \phi_m$ and the equation $\nabla^2 \phi_m = 0$ is solved. In this case, for a uniform current distribution, one obtains the value of the poloidal field, $B'_\theta(a)$ at the current column boundary to be $B'_\theta(a) = B_\theta(1 \pm 3/4\, a/R)$ while in the approximation made above $B_\theta(a) = B_\theta(1 \pm a/R)$. Since a/R is 0.13 in this experiment, the difference between the two results is only three or four percent. It is noted that the approximation used neglects to include flux from other portions of the torus.

Because of the shot-to-shot variation in the voltage form induced across the single turn coil, it was not possible to obtain an estimate of whether changes in the current distribution occur as a function of time. To accomplish this a multiple coil probe is inserted into the plasma column so that each coil will simultaneously sample the poloidal flux at different radial positions. Each coil has a corresponding "bucking loop" to cancel out the

external betatron field. Because of the lack of oscilloscope traces, only three of the four coils in the probe could be used at one time. The individual coil sensitivities are calibrated with respect to each other by observing the induced voltage from the betatron field without the bucking coils. The three coils used in the probe have sensitivities differing by 8 percent or less and the overall induced voltage forms are very similar in appearance.

The multiple coil form is constructed from four computer punch cards glued together. The same column of each card is multipli-punched. The separation of the holes is 0.31cm while the hole length is 0.32cm. After the glue is dry, the column is cut from the rest of the card by use of a razor. Number 36 copper wire is wound six times around the punched hole partitions (figure 4) to form the different coils. The coils are wound in such a way that the turns do not overlap, but are adjacent to each other. The sixth turn joins the two coil leads and the leads are twisted, approximately, in the same manner. This form is then inserted into a capped quartz tube with the coil leads extending a few inches beyond the open end of the quartz tube. The lengths of the leads are staggered to allow for an even distribution of space taken up by the splices made to four Microdot co-axial cables. These

cables pass through a stainless steel tube which slides over the splices and open end of the quartz tube. Low vapor pressure epoxy is then applied to the joint between the quartz tube and stainless steel tube to form a vacuum seal. The quartz tube is long enough so that only the quartz is in contact with the plasma.

Assuming a uniform current distribution, and neglecting toroidal corrections, one can easily show that the center of the current distribution, r_0 , is given by $r_0(t) = \frac{1}{2}\left(r_1 + r_2 - \frac{V_1(t) + V_2(t)}{m(t)}\right)$ where $m(t) = \frac{V_2(t) - V_1(t)}{r_2 - r_1}$ r_1 and r_2 are the fixed positions of coils 1 and 2 located within the current column and $V_1(t)$ and $V_2(t)$ are the integrated induced probe voltages. The width of the distribution can be estimated when one of the coils is outside of the current distribution by $R_0(t) = \sqrt{\frac{r_3\, V_3(t)}{m(t)}}$ where $R_0(t)$ is the radius of the distribution measured from the center of the distribution and determined from the value of $r_0(t)$. Because of the lack of oscilloscope traces, one trace is not integrated electronically. The integration is carried out by Simpson's rule and by the Trapezoid rule[8] to check the accuracy of the numerical integration method. Both methods yield very similar results for the data analyzed.

Because a comparison is made among different probe

signals, one is interested in knowing the phase shift introduced in the probe-oscilloscope detecting system. More specifically, it is of interest to determine the phase shift, ϕ , between the voltage detected by the probe, V_g , and the voltage displayed by the oscilloscope V_{in} . Figure 5 shows the circuit considered to comprise the probe-oscilloscope system. One has the following relations:

$$I(Z_g + Z_{in}) = V_g$$

$$I Z_{in} = V_{in}$$

$$\frac{V_{in}}{V_g} = \frac{Z_{in}}{Z_g + Z_{in}} = \left[1 + \frac{Z_g}{Z_{in}}\right]^{-1} = \frac{|V_{in}|}{|V_g|} e^{-j\phi}$$

$$\frac{1}{Z_{in}} = \frac{X_C + j R_{in}}{R_{in} X_C} \quad ; \quad Z_g = R_g + j X_L$$

Thus $$\phi = \tan^{-1}\left\{\frac{X_L X_C + R_g X_{in}}{R_{in} X_C - X_L R_{in} + X_C R_g}\right\}$$

Typically $X_C \cong 100$ohms, $R_g \cong 1$ohm, $X_L \cong 0.5$ohms, $R_{in} \cong 10^3$ to 10^6ohms

Thus $$\phi \cong \tan^{-1}\left\{\frac{R_g}{X_C}\right\}$$

and is typically 1×10^{-2}radians. For a 40KHz signal this amounts to a 0.03usec time delay which can be neglected in comparison to the reproducibility of the waveforms observed.

CHAPTER V

FIGURE CAPTIONS

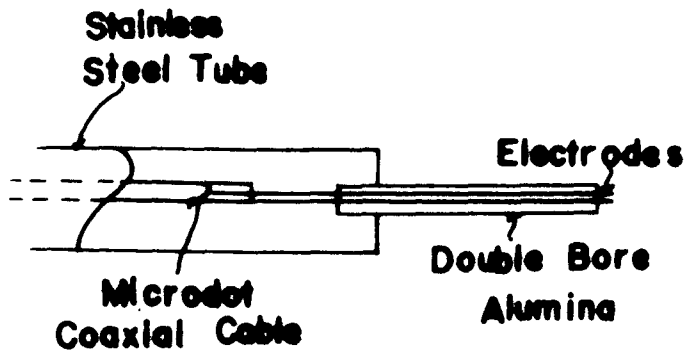
Stainless
Steel Tube
Electrodes
Double Bore
Alumina
Microdot
Coaxial Cable

FIG. 1

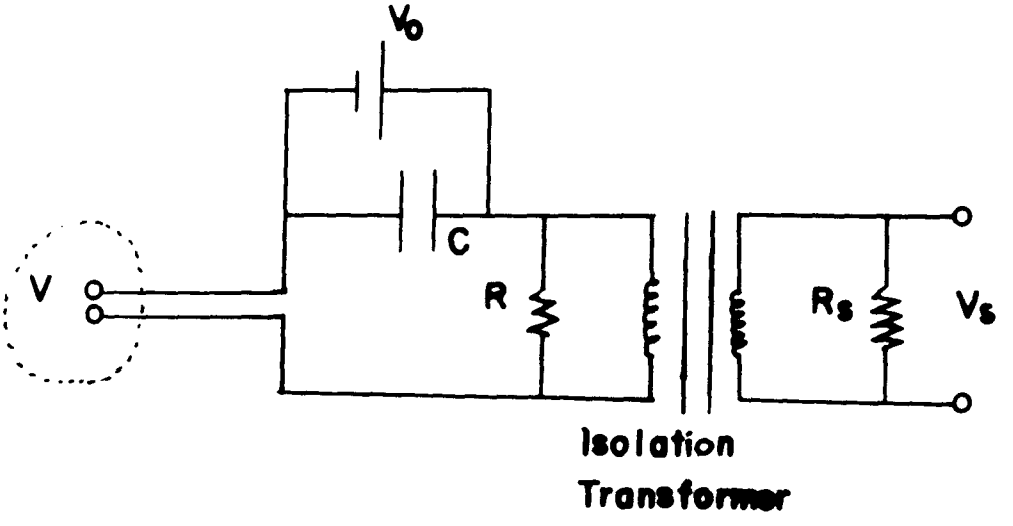

FIG. 2

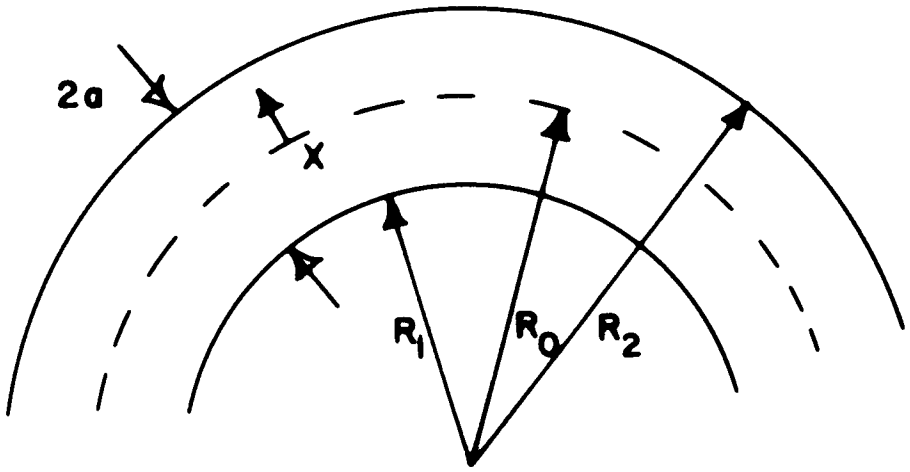

FIG.3

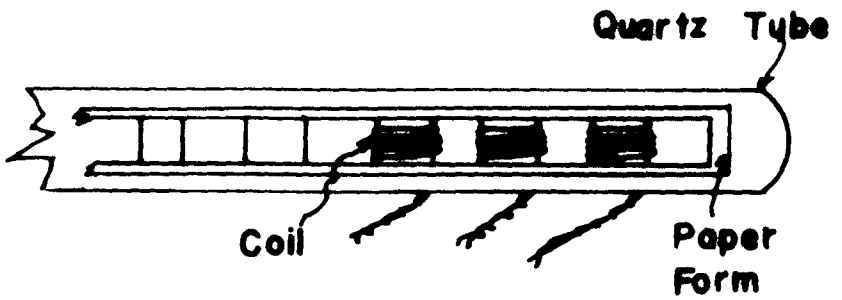

FIG. 4

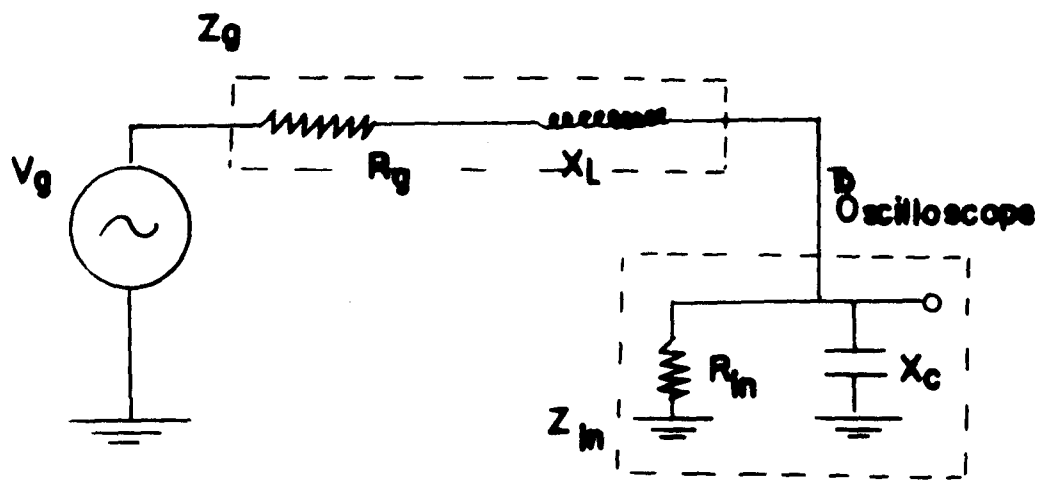

FIG.5

CHAPTER V

REFERENCES

1. R. H.Huddlestone and S.L. Leonard, Editors, Plasma Diagnostic Techniques (Academic Press, New York, 1965, Chapter 4).
2. R. Lee, Electronic Transformers and Circuits (John Wiley and Sons, Inc., New York, 1955, Second Edition).
3. M. A. Heald and C. B. Wharton, Plasma Diagnostics With Microwaves (John Wiley and Sons Inc., New York, 1965).
4. R. H. Huddlestone and S. L. Leonard, op. cit., Chapter 2.
5. G. Lewin, Fundamentals of Vacuum Science and Technology (McGraw-Hill Book Company, New York, 1965, Chapter 5).
6. R. D. Evans, The Atomic Nucleus (McGraw-Hill Book Company, New York, 1955, Chapter 25).
7. V. D. Shafranov, Reviews of Plasma Physics, M. A. Leontovich, Editor, (Consultants Bureau, New York, 1966, Volume 2).
8. E. Kreyszig, Advanced Engineering Mathematics (John Wiley and Sons, Inc., New York, 1965).

CHAPTER VI

EXPERIMENTAL RESULTS

In this chapter a brief overview of the experimental results is first given followed by a detailed description of the results of the measurements. Figure 1 shows the variation of the azimuthal field strength, E_ϕ, and the total azimuthal current, I, as a function of time. This is for a hydrogen discharge of initial neutral pressure of 4×10^{-3} Torr and peak E_ϕ, at the first maximum, equal to 6.9v/cm. The first large current peak is 970 amperes. The evident nonlinear form of $I(t)$ is characteristic, to some extent, of all the discharges that have been studied in this experiment. Figure 2 shows a superposition of the electric field wave form (third peak) and the corresponding current in an argon discharge for two different neutral densities (5.4×10^{-4}T and 8.2×10^{-4}T). Typically, as the neutral density is lowered the current form becomes more distorted. At high neutral densities (about 10×10^{-4}T in argon) the current form becomes a near sinusoidal wave form with an increased inductive component. Figure 3 is a superposition of the electric field wave form and the azimuthal current in hydrogen for two

different neutral densities. In the hydrogen discharges the neutral densities could be lowered enough so that very small peak currents are produced and yet the rapid density build-up occurs during the first cycle. Figure 4 shows the typical rate at which density build-up occurs during the first electric field cycle in argon. Figures 5 and 6 show $n T_e^{1/2}$ changes over the entire discharge in argon and hydrogen. Here n is the plasma density and T_e is the electron temperature.

X-ray emission (figures 21 to 27) is observed after the start of the first acceleration cycle for certain neutral densities of argon and hydrogen. At a low neutral density in hydrogen, X-ray emission is seen to occur after the start of the third acceleration cycle. As the neutral density is lowered, still further, additional X-ray emission is seen to occur after the start of every acceleration cycle.

Several Langmuir probes were constructed in order to determine the density and temperature of the plasma. The first probe which was constructed is composed of a wide alumina tube which supports the electrodes. This probe gave the following density and temperature values for different electric field strengths in argon:

E_ϕ (v/cm)	n ($\times 10^{12}$ cc^{-1})	T_e (ev)	% ionization
2.3	2.8	29	17
4.7	3.4	24	20
7.0	5.9	27	36
9.3	7.9	24	47

The percent ionization is found by comparing the initial neutral pressure, 5.44×10^{-4} T = 1.67×10^{13}cc^{-1} , to the measured plasma density. The K-band transmission cut-off occurs for all values of E_ϕ during the first cycle. For these measurements the cutoff density is 4×10^{12}cc^{-1}. Therefore, a difference of at least a factor of two is present in the Langmuir probe density determination and the microwave measurement. A higher frequency interferometer will provide more information about the average density as a function of time. Figure 7 shows the characteristic obtained for the E_ϕ =9.2v/cm case. The method of obtaining the characteristic is to average over several cycles of the electric field and to take an average of two or more discharges for each point plotted. It is noted that in figure 7 the characteristic does not appear symmetrical with respect to the V axis. This occurs for all of the characteristics taken with this probe. It is noted that more points near the charac-

teristic origin should be obtained for an accurate determination of $dI/dV)_o$.

A second Langmuir probe was constructed which uses two pieces of narrow diameter (0.094cm) double bore alumina tubing with each piece holding one electrode. Figure 8 is the corresponding $I-V$ curve for argon with a neutral density, $n_o = 2.15 \times 10^{13} cc^{-1}$, the peak $E\phi$ =7.0 cm and $B\phi$ = 1.1Kg. Figure 9 represents a plot of points near the origin for the $I-V$ curve shown in figure 8. One notes the symmetry of the entire characteristic curve. In determining $dI/dV)_o$ from figure 8 there appears to be at least a factor of two possible error due to the scatter of the points. The values of n_e, T_e and percent ionization obtained from this characteristic are $1.7 \times 10^{13} cc^{-1}$, 5.4ev and 77 percent repectively. Figure 10 is an $I-V$ curve for hydrogen, $E\phi = 9.3 v/cm$, $n_o = 40 \times 10^{12} cc^{-1}$ and $B\phi$ = 1.1Kg. For this characteristic an attempt was made to obtain more points near V =0. The values of n_e, T_e, and percent ionization are $n_e = 7.3 \times 10^{12} cc^{-1}$, T_e =14ev and 18 percent respectively.

Langmuir probes can also provide an estimate of the relative density as a function of radial position and of time, provided that the temperature does not vary appreciably over the major part of the discharge. Figures 11, 12, and 13 show different density profiles obtained with a

Langmuir probe averaged over several cycles and discharges. The extremes of the error bars along the density axis represent the maximum and minimum range of the ion saturation current measured. A trapezoid approximation to the density profile seems warranted.

Figures 5 and 6 show how the Langmuir probe can be used to estimate the product of $n_e T_e^{1/2}$. By maintaining the probe voltage at a fixed value in the ion saturation region one can record a voltage proportional to $n_e T_e^{1/2}$. If T_e is assumed approximately constant, then these curves represent density as a function of time. Generally, by the third or fourth electric field peak the ion saturation curve levels off.

If $n_e(t)$ could be measured by a method other than the ion saturation curve one could estimate the variation of T_e as a function of time from the ion saturation curve. To accomplish this a K-band (18.0GHz to 26.5GHz) interferometer is employed to measure $n_e(t)$ averaged over the plasma column. However, in all of the cases studied cutoff is reached before the end of the first acceleration cycle. Thus the K-band interferometer can only be used to indicate an average lower limit to the discharge and to show the growth and decay of the discharge. Figure 4 shows the growth rate of plasma density in argon for different values of the peak electric field strength. The micro-

wave frequency is 22GHz.

Shown below is the build-up time, τ_b , which represents the time it takes for the plasma density to reach 6×10^{12} cc^{-1} (microwave cutoff) in the initial cycle. As shown in figure 4, τ_b varies with the peak electric field, E_m . The width of the plasma column, L , is assumed constant in time. A uniform distribution is also assumed. The phase shift data implies a width, L , for the different cases shown in figure 4. E_m , τ_b , and L are shown below.

E_m (v/cm)	τ_b (μsec)	L (cm)
2.6	1.4	0.47
3.2	1.3	0.47
4.9	0.45	0.36
8.2	0.30	0.34

The neutral pressure in this case is 2.5×10^{13} cc^{-1}. The width of the distribution represents the minimum plasma width at cutoff since the curves are based on a rectangular distribution. A triangular distribution would give a width at cutoff three times as large, as indicated in chapter V.

The total azimuthal current flow is measured as a function of time by the use of a Rogowski coil. Figures 1, 2, and 3 show typical current forms in hydrogen and argon.

Figure 1 is an enlargement of an oscilloscope trace photograph. Figures 2 and 3 are enlargements that have been digitized. The numerical values are re-plotted in these figures. The time scales for the current forms and the electric field are accurate to within $\pm$ 1/4 usec. For clarity only one cycle is shown in figures 2 and 3. However, the same curves have been extended over three cycles and a fifth curve over five cycles. From the digital form, plasma conductivity and the position of the equilibrium orbit can be calculated as will be discussed in the eighth chapter. The precision of the relative current measurement is limited by the determination of the current zero level. The absolute value of current depends on the calculated sensitivity of the Rogowski coil and thus, the precision of this measured quantity depends on the calibration error of the Rogowski coil. It is expected that the calibration error is not more than 10 percent. The location of the zero level has a much smaller effect on the measurement of the current at all points in time except near the current zeroes (where the relative error is large). The determination of the relative phase between the electric field and the current is affected by the difficulty in determining the precise moment the electric field starts, when the current trace is measured, and, to a lesser extent,

when the electric field trace is measured. A rough check can be made by observing the pick-up on a poorly "bucked-out" current trace.

Figure 14 shows a magnetic field profile of the current column at peak values of the current for hydrogen discharges . A single coil probe plus a coil, to subtract out the betatron magnetic field, is used. The single coil is placed into the plasma at different radial positions for a fixed azimuthal position and in the median plane. The experimental points are represented by the error bars. The size of the error bars represent typical shot-to-shot variations in the relative magnitude of B_θ , the self-field of the current column. Each value of B_θ plotted is first normalized with respect to the total current flow which is typically 500 to 1000 amperes. The current form is shown in figure 1. The initial peak electric field is 6.9 v/cm. The peak studied for each discharge corresponds to the third electric field peak. Only the peak value of B_θ (and the value of the total current corresponding to the time of the B_θ peak) is used in the single probe experiment. When times other than the peak time are considered, the shot-to-shot variation in the current signals result in inconsistant profiles. Figures

15 and 16 show typical oscilloscope trace enlargements used in determining the magnetic field profile shown in figure 14. The top trace is the total current flow while the bottom trace is B_θ. A small amount of pick-up is present in the B_θ signal and total current signal. The vertical lines represent part of the grid used to digitize the wave forms. Each vertical line is separated by approximately 0.88 microseconds. It is noted that the total current wave form has a similar form on a shot-to-shot basis. For eleven traces the current peak occurs at 28.08 ± 0.27 usec after the start of E_ϕ. At least half of the error (mean absolute deviation from the average value) in the time measurement of the current peak can be attributed to the difficulty in determining the precise time the discharge begins and the exact time of the current peak. The variation in the peak current value is relatively much greater. The average current value for the same cases is $7.5 \times 10^2 \pm 1.2 \times 10^2$ amperes. This large variation in the current peak value cannot be attributed to measurement error but represents a shot-to-shot fluctuation in those plasma parameters which determine the current maximum. Referring back to figure 14, the solid curve represents a plot of the approximate analytic value of B_θ (see chapter V) as a function of X. Here the current column is assumed to

have a radius of 2.00cm. A second plot, in dashed lines, shows the analytic value of B_θ versus X for a current radius of 1.50cm. Because each experimental point is obtained from only one or two discharges, it is felt that on the average, the single probe coil measurements are consistent with the existence of a near uniform current distribution.

In order to better understand the shot-to-shot variation in the poloidal magnetic field and the time variation of the current form, the poloidal field is measured at several radial positions simultaneously. Figures 17 and 18 show the variation of B_θ as a function of time, in the median plane, at three different radial positions. Measured from the center of the minor diameter of the vacuum chamber to the center of each loop, the positions of the three loops are 0.89cm, 1.52cm, and 2.15cm, respectively. The experimental conditions for these measurements are the same as for the single coil measurements.

Figure 18 clearly shows the motion of the center of the current column across the 0.89cm loop. This is indicated by the change in direction of the magnetic field threading through the 0.89cm coil. The fact that the other loop signals do not reverse in direction places limits on the amount that the center of the column is

displaced in this particular discharge and the approximate velocity of displacement. In 10^{-6} seconds the center moves 0.5cm which corresponds to a velocity of about 5×10^5 cm/sec. Figure 17 shows a case in which the center of the distribution does not move far enough to produce a reversal in signal. The distortions observed in the signals, as compared to each other, for example, can be attributed to the motion of the plasma column. Figures 19 and 20 show the enlargements of the oscilloscope traces used in figure 17. The loop 1 coil signal has a good deal of pick-up while the loop 3 coil signal has a very small amount of pick-up and the loop 2 coil signal has a negligible amount of pick-up. The residual pick-up is fairly easily removed by superimposing the enlarged pick-up signal photograph onto the enlargement of the combined pick-up and B_θ signal photograph. The pick-up trace is then used as the new baseline.

From figure 17 one can compute the size of the current column and the position of the center of the current column as a function of time. Below are listed the values of the position of the center of the current column, r_o, with respect to the center of the vacuum chamber and the radius of the current column, R_o, as measured from r_o. It is assumed that the current is uniformly

distributed and the toroidal correction is neglected.

$t_{(\mu sec)}$	0.5	1.0	1.5	2.0	2.5	3.0	3.5	4.0	4.5	5.0
$r_{e(cm)}$	.86	.80	.65	.63	.55	.49	.51	.61	.52	.17
$R_{e(cm)}$	.66	.75	.94	1.02	1.10	1.11	1.15	1.20	1.33	2.01

These results are consistant with the values of the current column radius found from the signal coil probe measurements which were averaged over many discharges.

From the observed motion of the center of the plasma column (figure 18) one can hypothesise that the oscillations in the Langmuir probe ion saturation current traces (figures 5 and 6) are due partly to the relative motion of the current column with respect to the probe. Use of magnetic probes at more than one azimuthal position would be helpful in trying to determine whether the current column motion is due to a uniform radial motion or a traveling wave structure in the plasma column. In chapter VIII the possibility of a kink structure is discussed.

Figure 21 shows a log-log plot of the X-ray emission time as a function of peak electric field strength during the initial acceleration cycle in argon discharges. The neutral pressure is 7.7×10^{-4} Torr. 96 observations are used for this plot. The emission time is given by

$$t_x = k E_\phi^{-n}$$

and n is found to be $n = 0.94 \pm 0.06$. Figures 22 and 23 are additional trials taken with fewer data points.

The respective values of n in these cases are 1.04 ± 0.17 and 1.12 ± 0.15. The plasma gun used in the measurements shown in figures 21 and 22 employs a copper center electrode, while in figure 23 the center electrode is made of hydrogen occluded titanium. The initial neutral pressure in figure 23 is 5.4×10^{-4} Torr. A similar dependence of τ_x on E_ϕ was found when a co-axial gun was used which injected plasma perpendicular to B_ϕ rather than tangentially as in figures 21 to 23. For hydrogen discharges the same dependence of τ_x on E_ϕ is found as is shown in figure 24 ($n = 0.8\pm0.2$). Figure 25 is a plot of τ_x versus B_ϕ for E_ϕ fixed at 6.9v/cm. 19 discharges are analyzed. The error bars represent the maximum deviation from the mean.

From the above experimental data one can conclude the following concerning the dependence of τ_x on the external fields: First, τ_x does not obey a $E_\phi^{-1/2}$ behavior and second, τ_x does not follow a $B_\phi^{+1/2}$ dependence. These two points eliminate the Negative Mass Instability and the Loss-of-Vector-Potential-Minimum (see chapter II) as explanations of the τ_x dependence on E_ϕ and B_ϕ .

It is observed that X-rays appear only in the initial acceleration cycle except for the special cases studied in hydrogen discharges. This corresponds to the fact that the

current peaks are lowest during the first cycle. Only when the neutral density is decreased to such an extent in hydrogen, so that the current peaks are 50 amperes or less do X-rays occur on every cycle. These low currents are not attainable in argon discharges. Within the experimental uncertainty the resistive current instability yields the correct $E\phi$ dependence, i.e., $\tau_x = \kappa E\phi^{-1}$ and the correct dependence on $B\phi$, i.e., independent of $B\phi$. The dependence of X-ray emission on the peak current values is also consistant with the resistive instability in the following way. For large enough currents the equilibrium orbit lies outside of the vacuum chamber. Since the current is fairly resistive this means that at the start of the acceleration cycle the equilibrium orbit lies outside of the vacuum chamber. In this case the freely accelerated electrons strike the vacuum chamber walls before their energy reaches a few Kev due to the unbalanced mv^2/R drift across the azimuthal magnetic field. The energy of the X-rays produced by these electrons are too low to be recorded by our X-ray detectors. On the first cycle the current is always considerably out of phase with $E\phi$ so that this argument does not hold true and the equilibrium orbit lies within the vacuum chamber. In the very low current hydrogen discharges the

current is low enough so that the equilibrium orbit is not displaced out of the vacuum chamber. Thus the resistive instability consistantly predicts the observed beam disruption time dependence on E_ϕ and B_ϕ and it does explain the lack of runaway electrons in acceleration cycles other than the first cycle as well as the appearance of runaway electrons in the low current hydrogen discharges.

Figure 26 is a plot of X-ray pulse height versus aluminum absorber thickness for E_ϕ = 6.7v/cm and E_ϕ = 10.6v/cm in argon discharges. The least square fit value of the slope yields, from the absorption coefficient, the X-ray energy of 40 Kev (6.7v/cm) and 65 Kev (10.6). Figure 27 is the same type of plot for argon discharges and E_ϕ =5.5v/cm as in figure 26 but two photomultipliers are used. One photomultiplier is the reference and is used to help normalize the attenuated signal for variations in X-ray flux. This yields a least square fit of 75 Kev. Because of the $1/E_\phi$ dependence of t_x, the predicted runaway energy is 79Kev, independent of E_ϕ for $\omega t_x \ll 1$. For the E_ϕ values considered here this is essentially true. Thus the X-ray energy is consistant with the presence of freely accelerated electrons during the first acceleration cycle.

CHAPTER VI

FIGURE CAPTIONS

Figure	Page	Caption
1	115	Typical Temporal Current and Electric Field Oscilloscope Traces
2	116	Digitized Current and Electric Field in Argon
3	117	Digitized Current and Electric Field in Hydrogen
4	118	Plasma Density as a Function of Time
5	119	Ion Saturation Current as a Function of Time in Argon
6	120	Ion Saturation Current as a Function of Time in Hydrogen
7-10	121-124	Langmuir Probe Characteristics
11-13	125-127	Density Profiles via Langmuir Probes
14	128	Poloidal Magnetic Field Profile Using Multiple Loop Probe

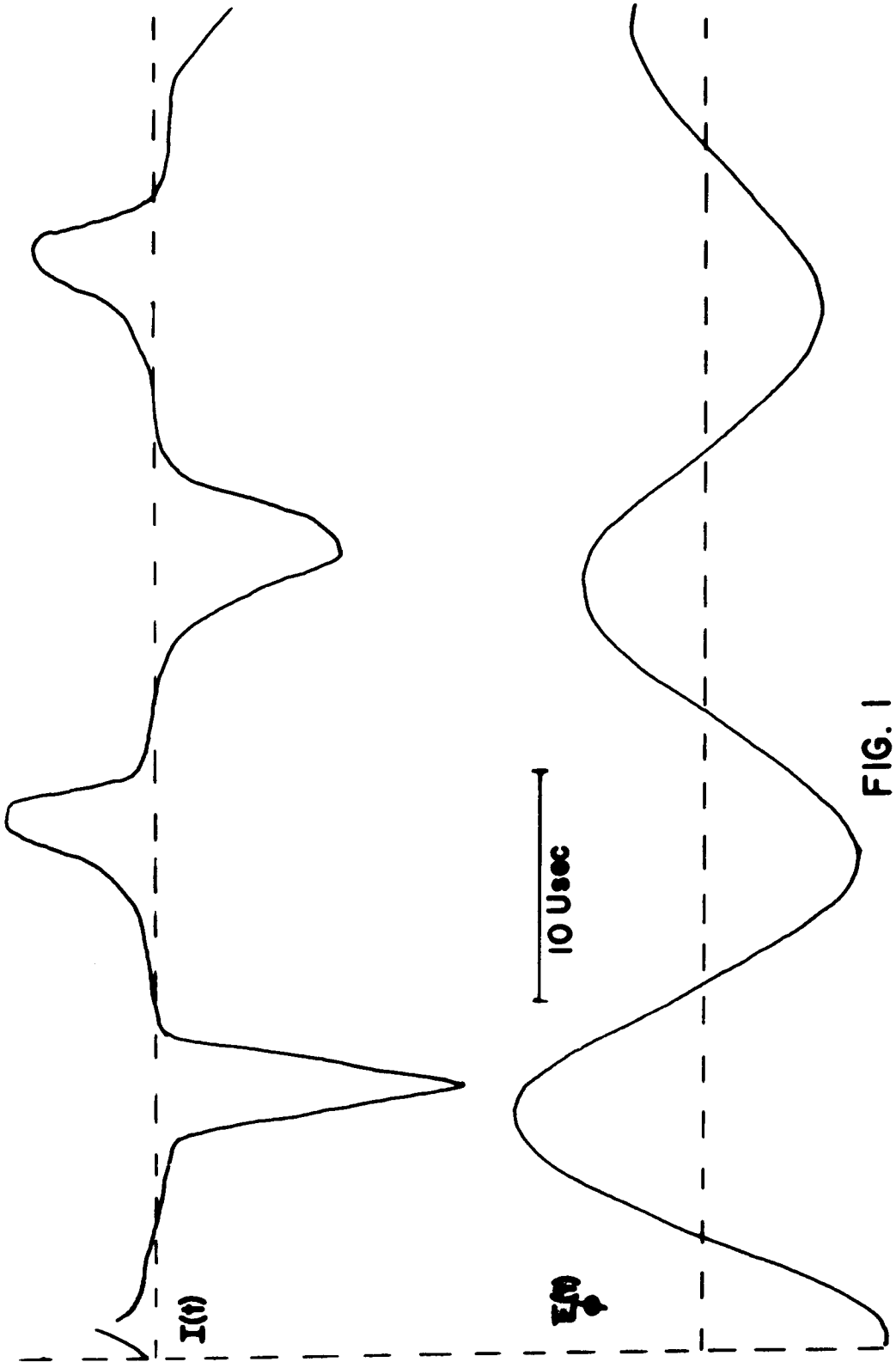

FIG. 1

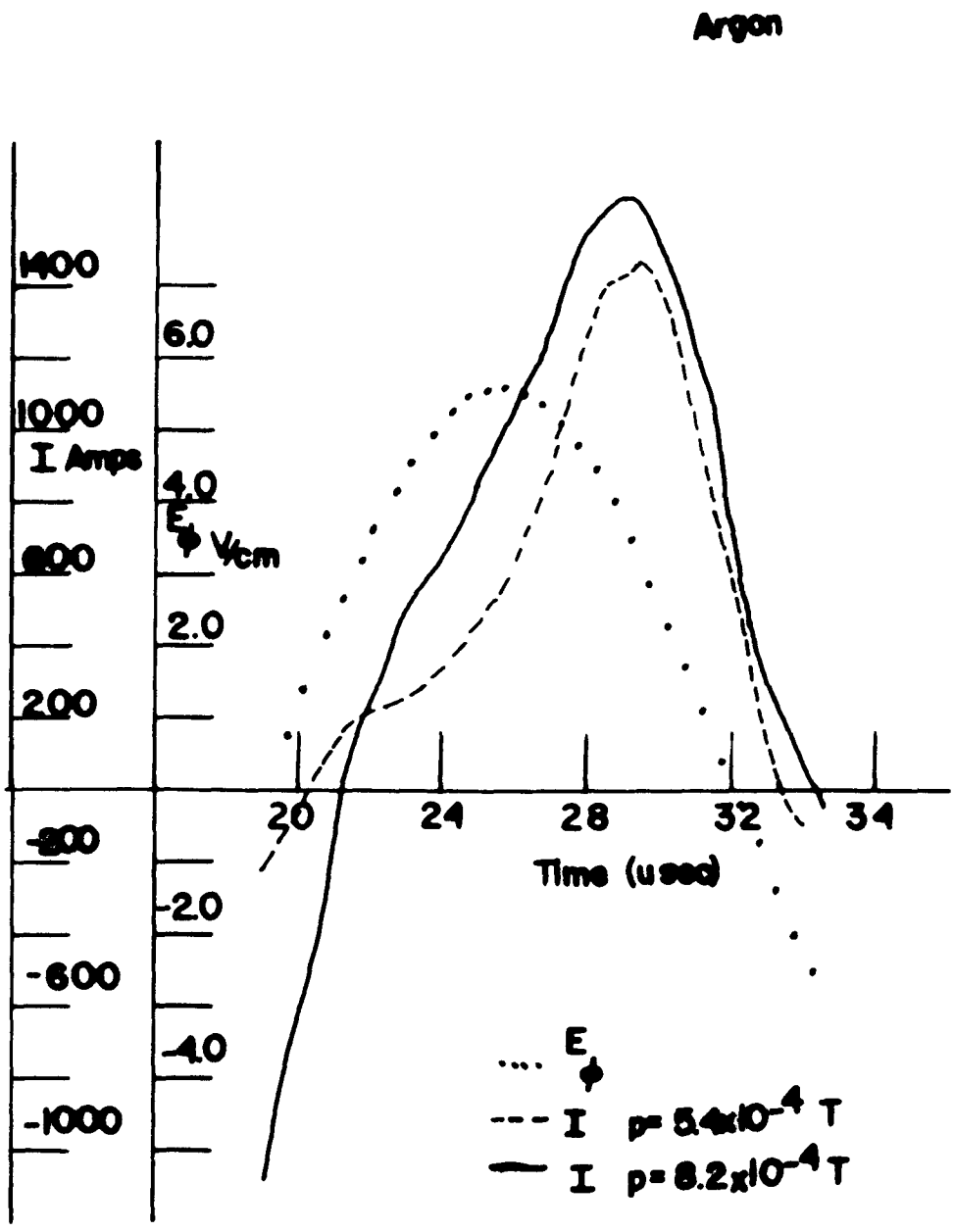
Argon
1400
1000
I Amps
800
200
-200
-600
-1000
6.0
4.0
E_ϕ V/cm
2.0
-2.0
-4.0
20
24
28
32
34
Time (u sec)
E_ϕ
I p= 5.4x10^{-4} T
I p= 8.2x10^{-4} T

FIG. 2

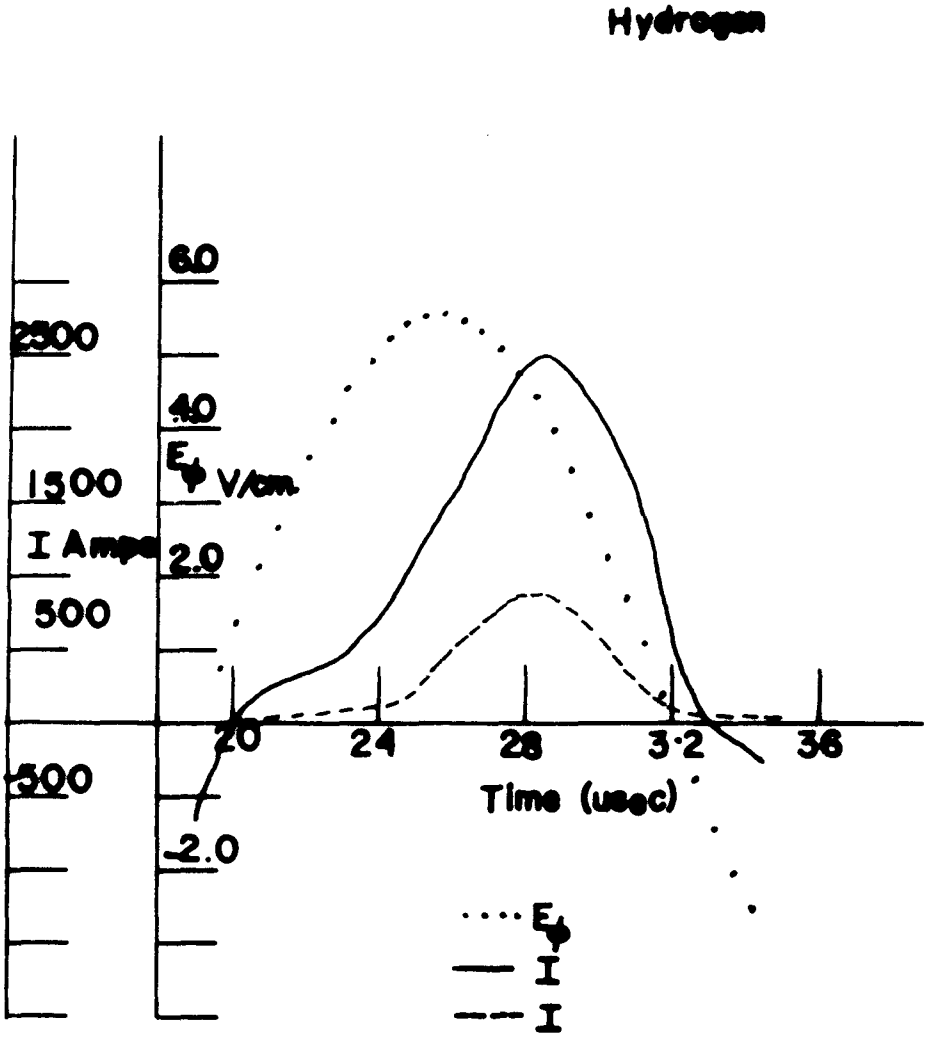
Hydrogen
6.0
2500
4.0
E_ϕ V/cm
1500
I Amps
2.0
500
20
24
28
3·2
36
Time (usec)
-500
-2.0
E_ϕ
I
I

FIG. 3

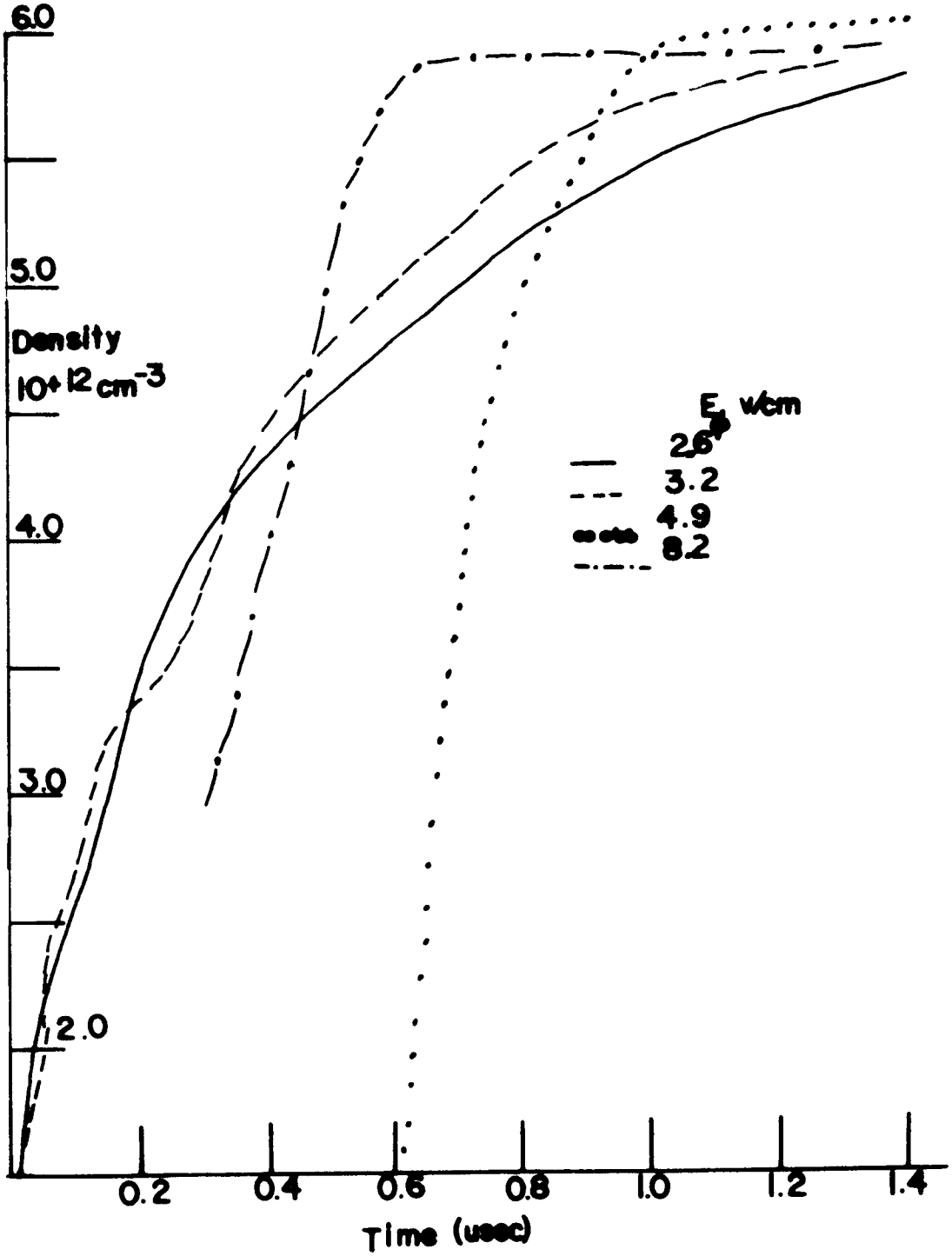
6.0
5.0
4.0
3.0
2.0
Density
10+12 cm-3
E w/cm
2.6
3.2
4.9
8.2
0.2
0.4
0.6
0.8
1.0
1.2
1.4
Time (usec)

FIG. 4

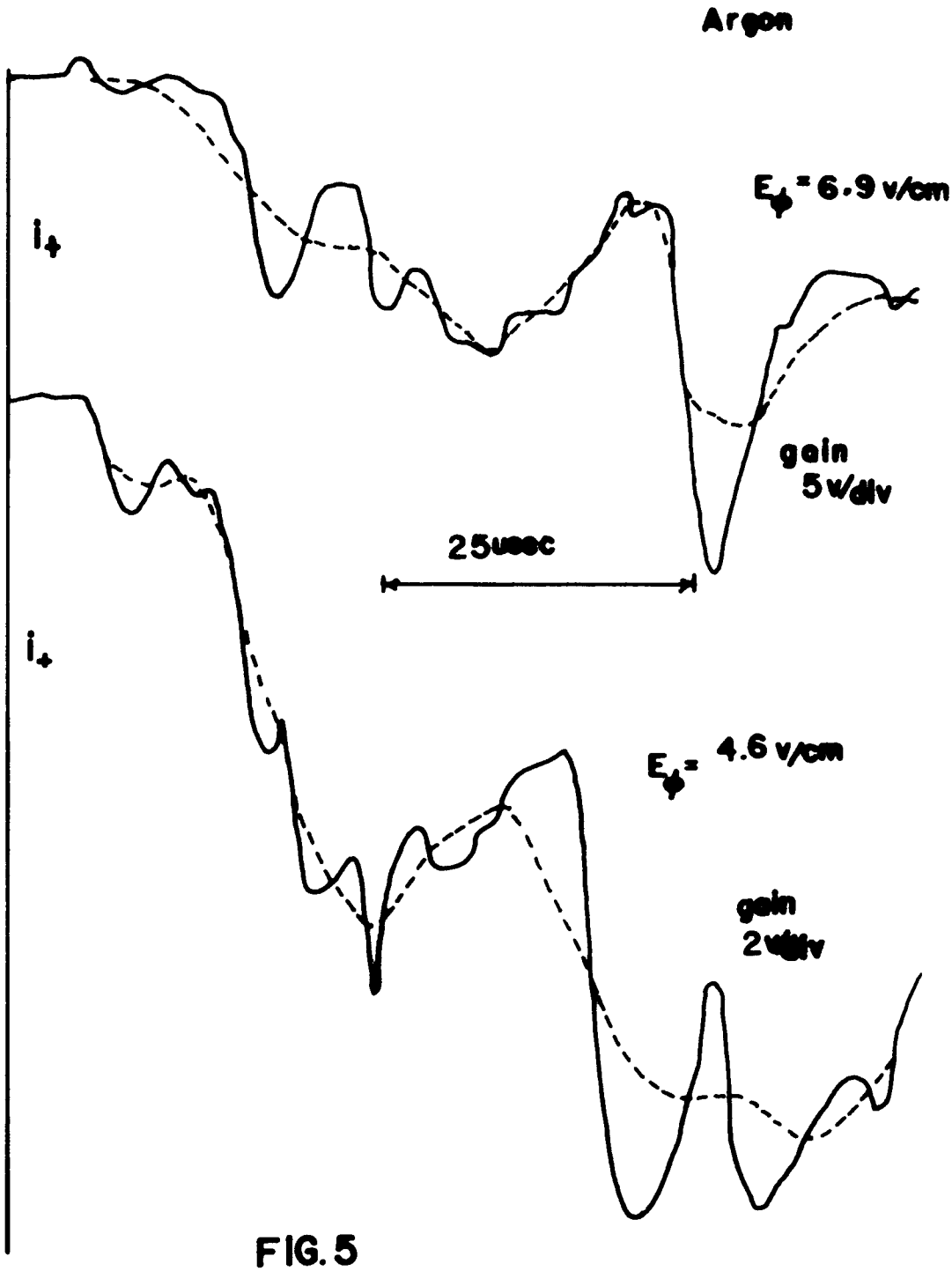

FIG. 5

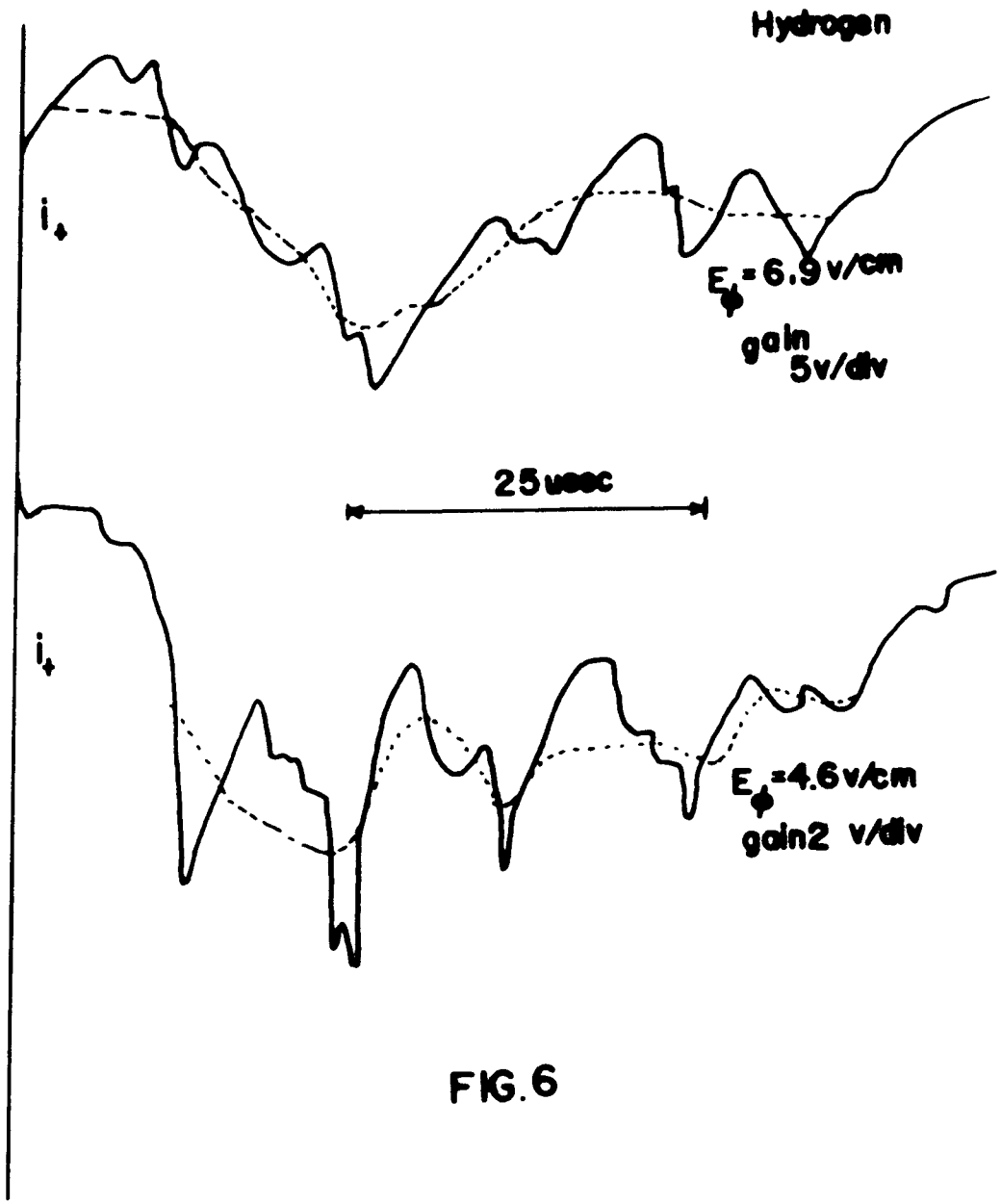
Hydrogen
i_ϕ
E_ϕ = 6.9 v/cm
gain 5v/div
25 μsec
i_ϕ
E_ϕ = 4.6 v/cm
gain 2 v/div

FIG. 6

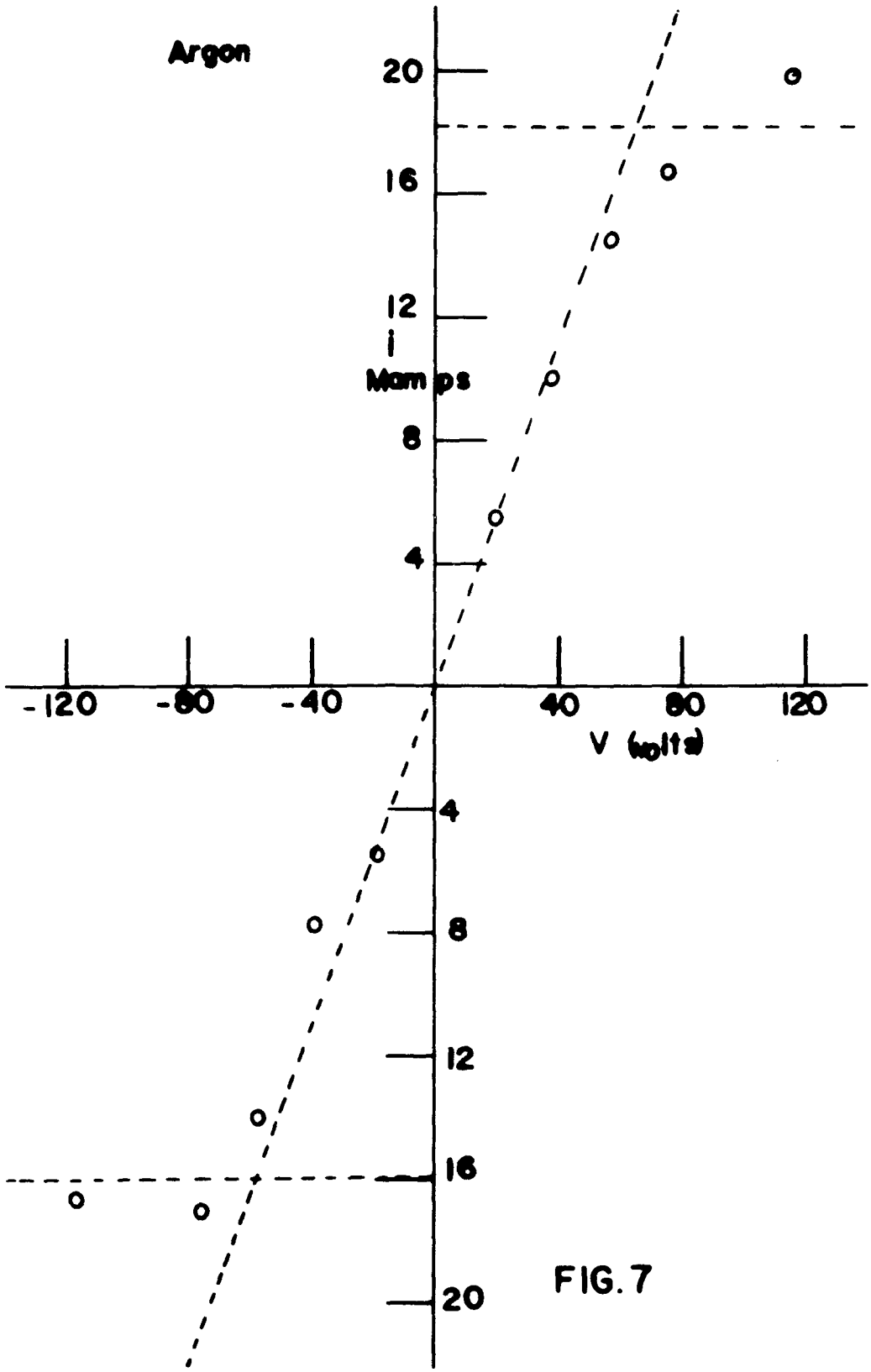

FIG. 7

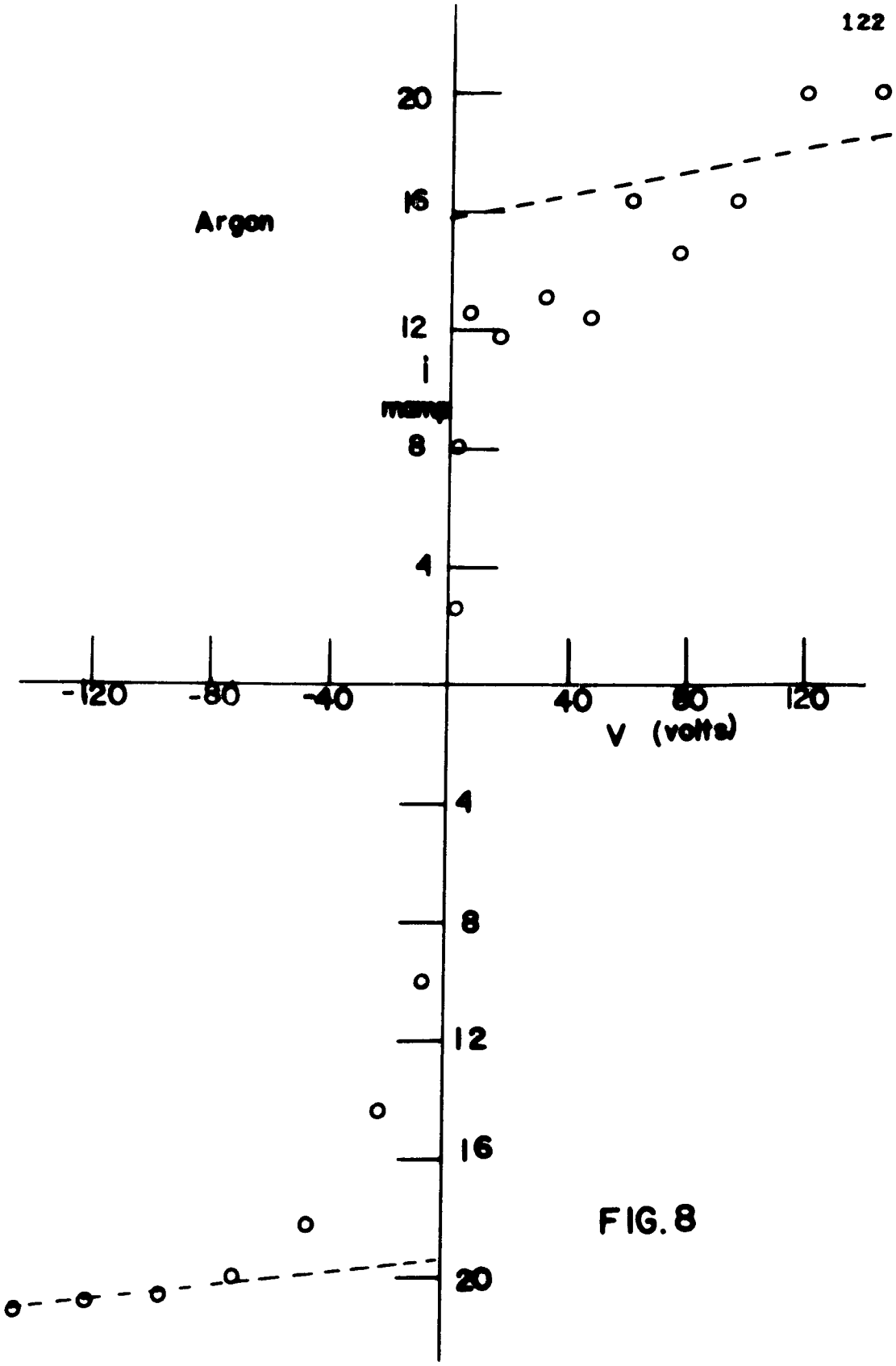

FIG. 8

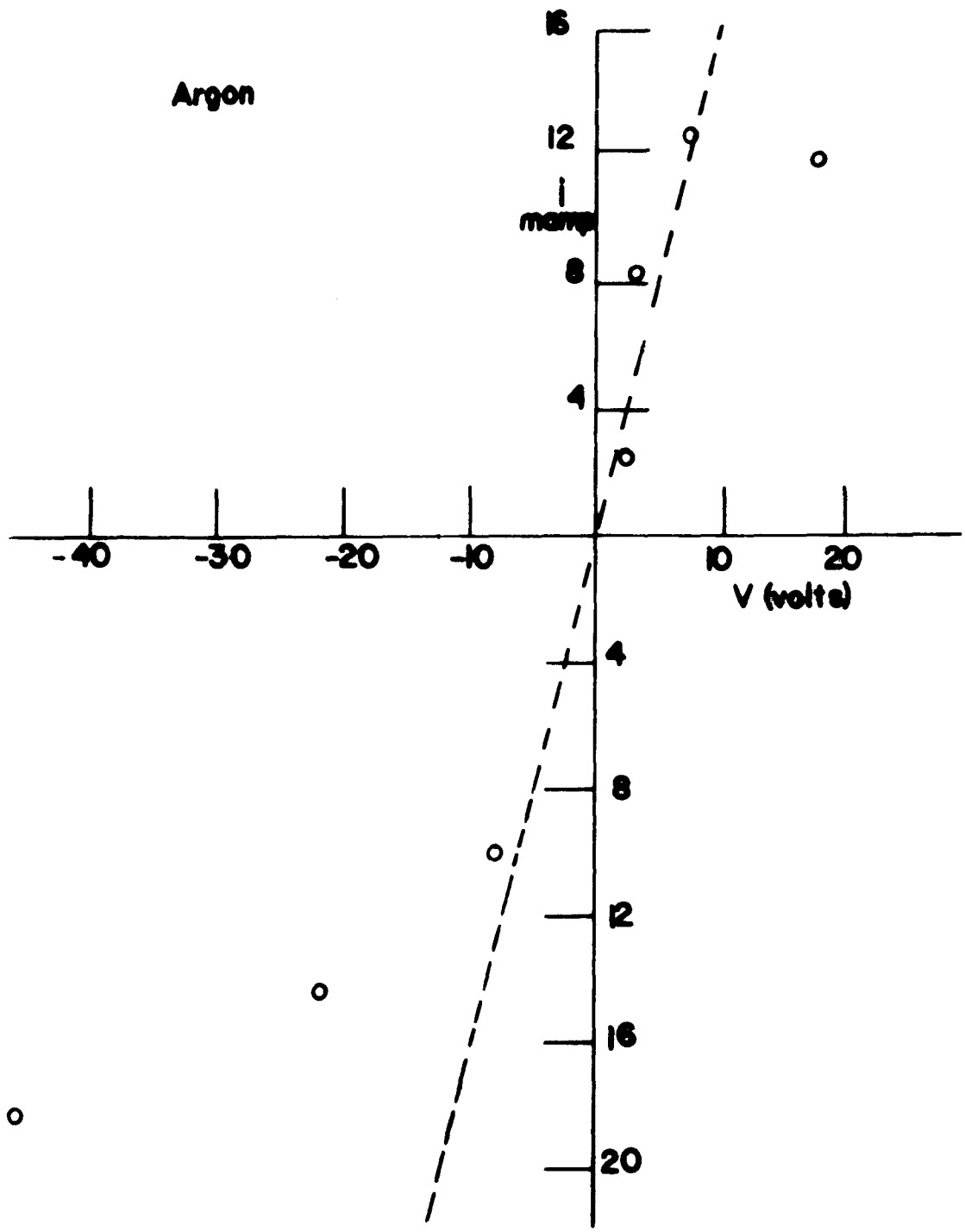

FIG.9

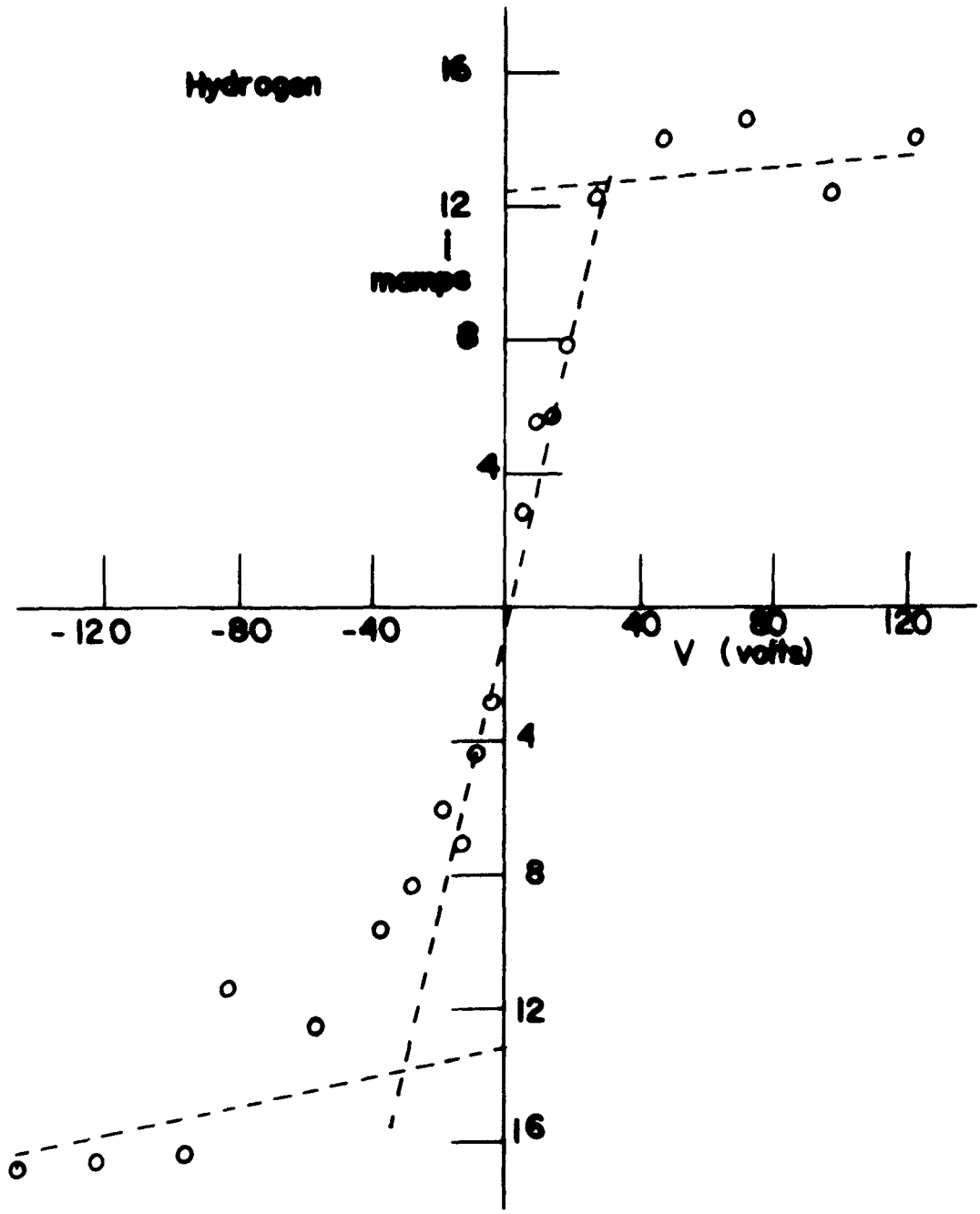

FIG. 10

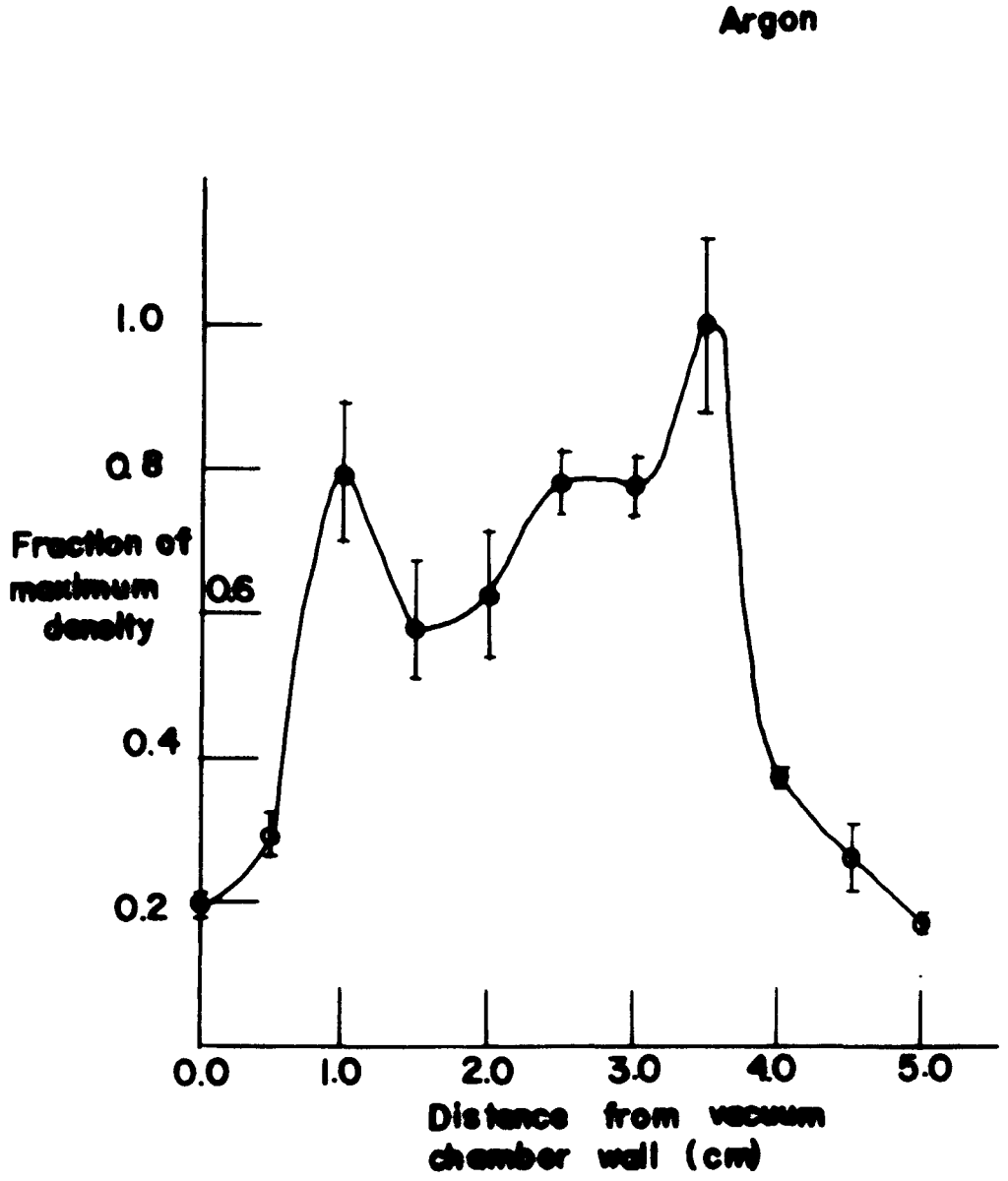
Argon
1.0
0.8
Fraction of maximum density
0.6
0.4
0.2
0.0
1.0
2.0
3.0
4.0
5.0
Distance from vacuum chamber wall (cm)

FIG. 11

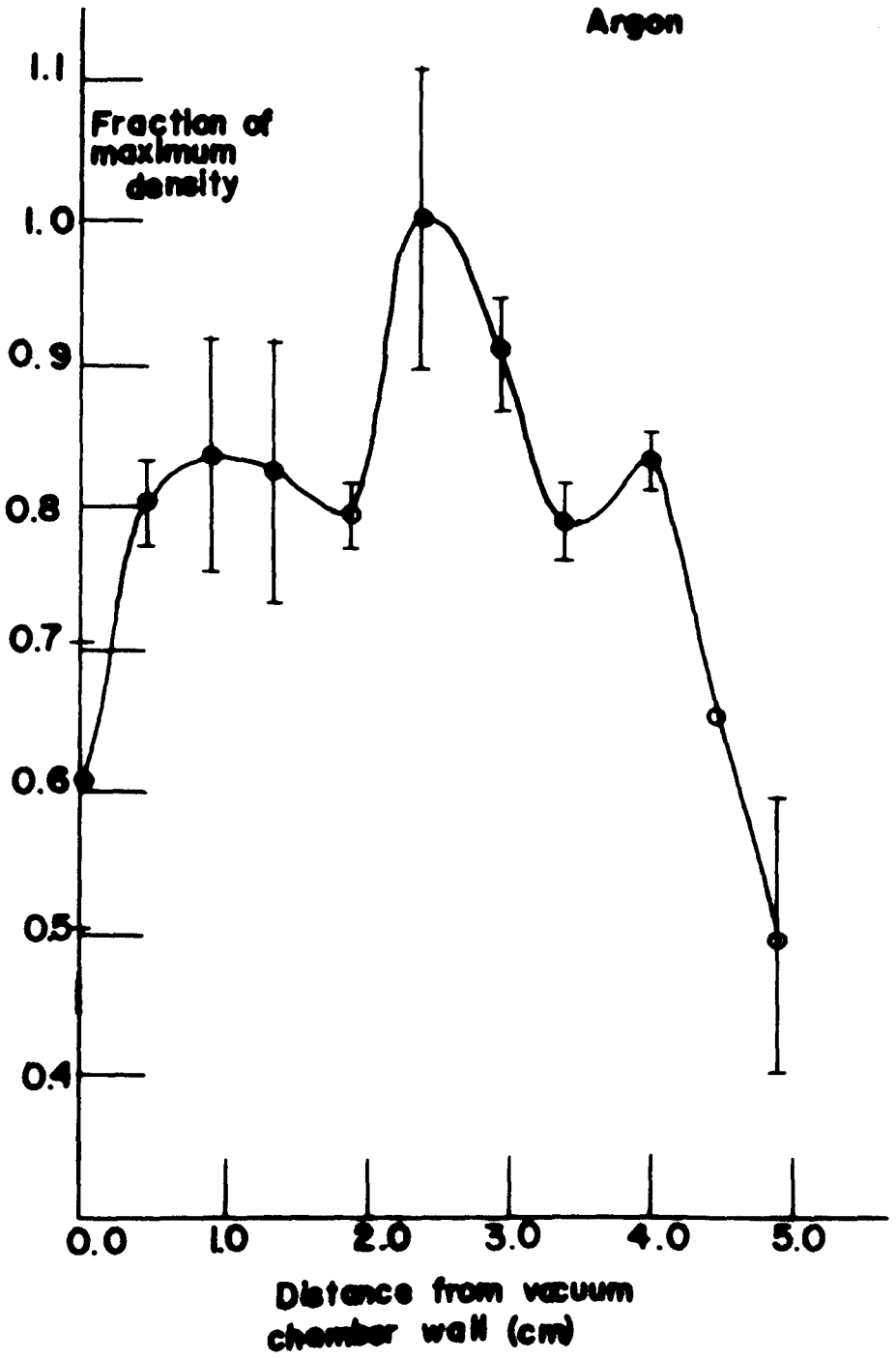
Argon
Fraction of maximum density
1.1
1.0
0.9
0.8
0.7
0.6
0.5
0.4
0.0
1.0
2.0
3.0
4.0
5.0
Distance from vacuum chamber wall (cm)

FIG. 12

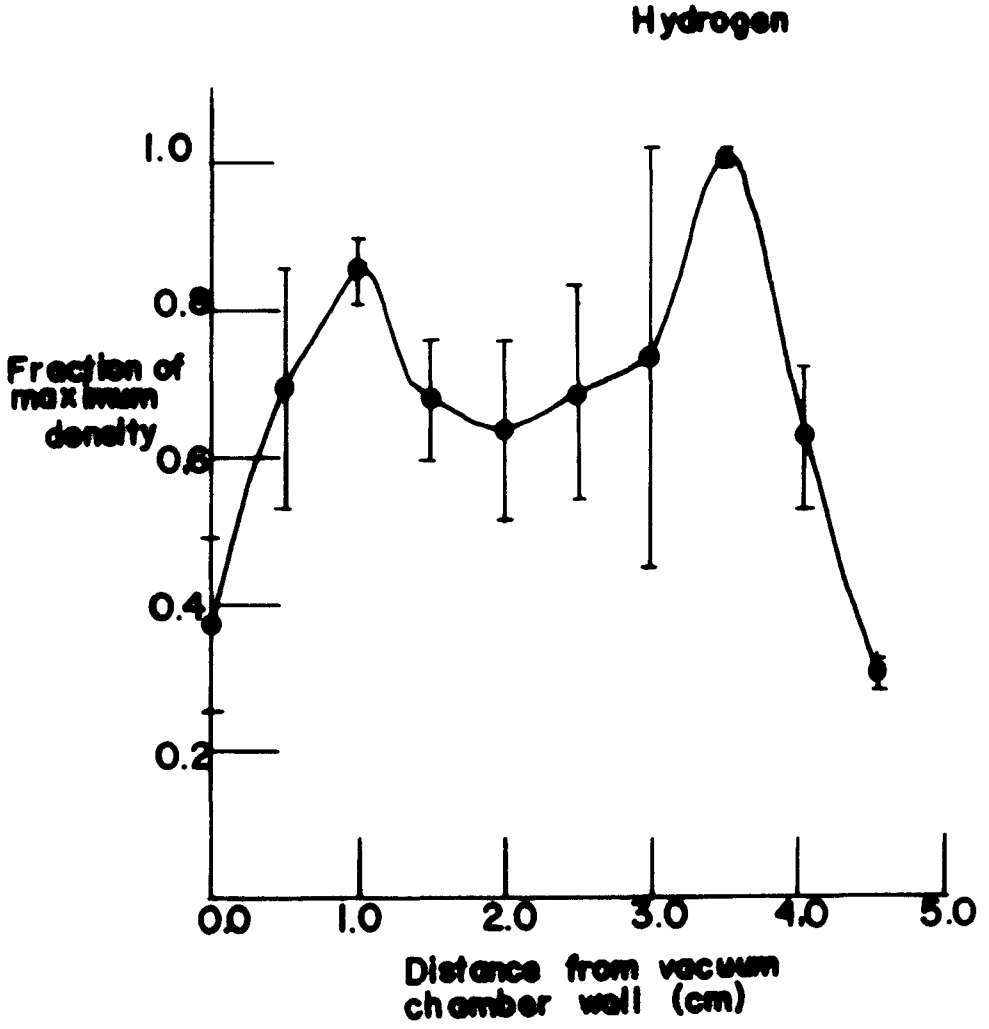
Hydrogen
1.0
0.8
0.6
0.4
0.2
Fraction of maximum density
0.0
1.0
2.0
3.0
4.0
5.0
Distance from vacuum chamber wall (cm)

FIG. 13

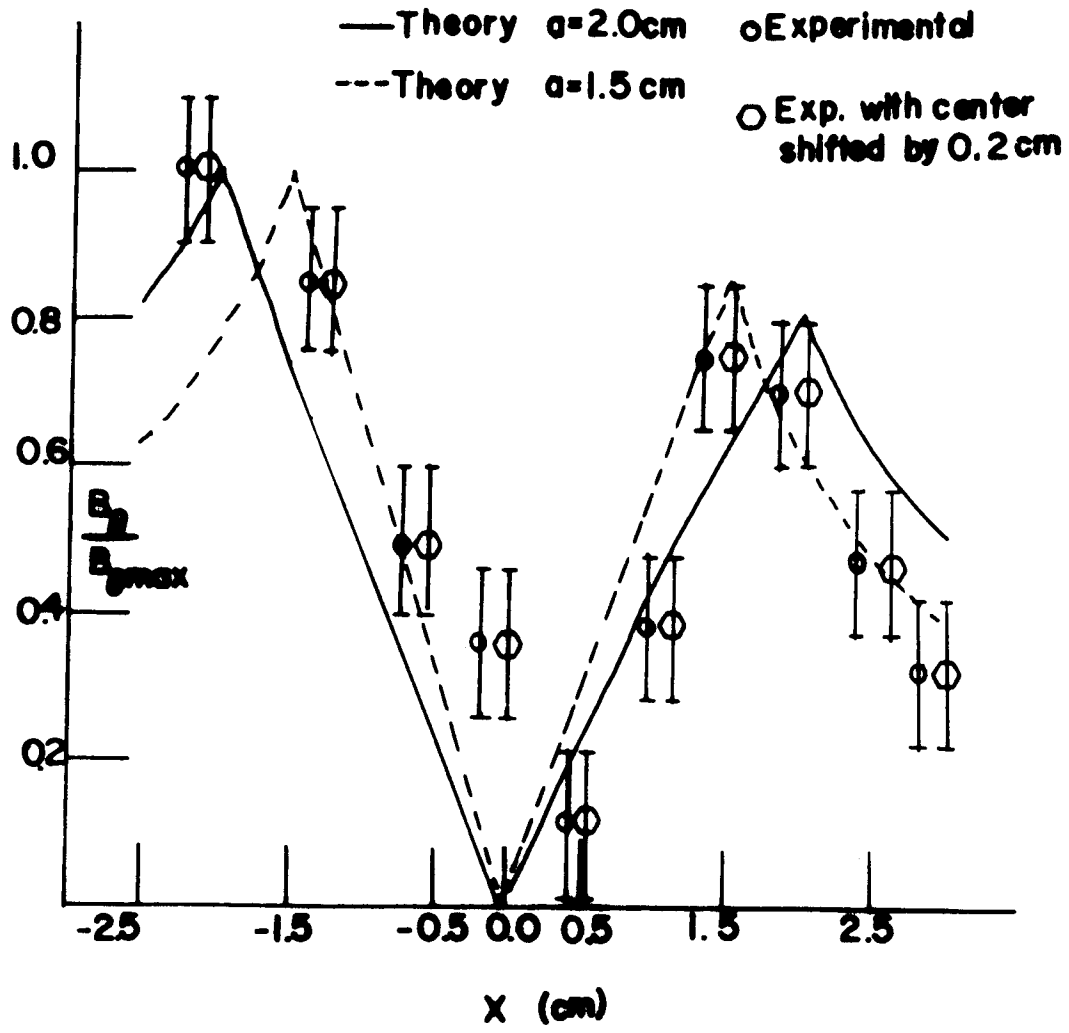
—Theory a=2.0cm
---Theory a=1.5 cm
oExperimental
O Exp. with center shifted by 0.2 cm
1.0
0.8
0.6
0.4
0.2
$\frac{B_z}{B_{z\max}}$
-2.5
-1.5
-0.5
0.0
0.5
1.5
2.5
X (cm)

FIG. 14

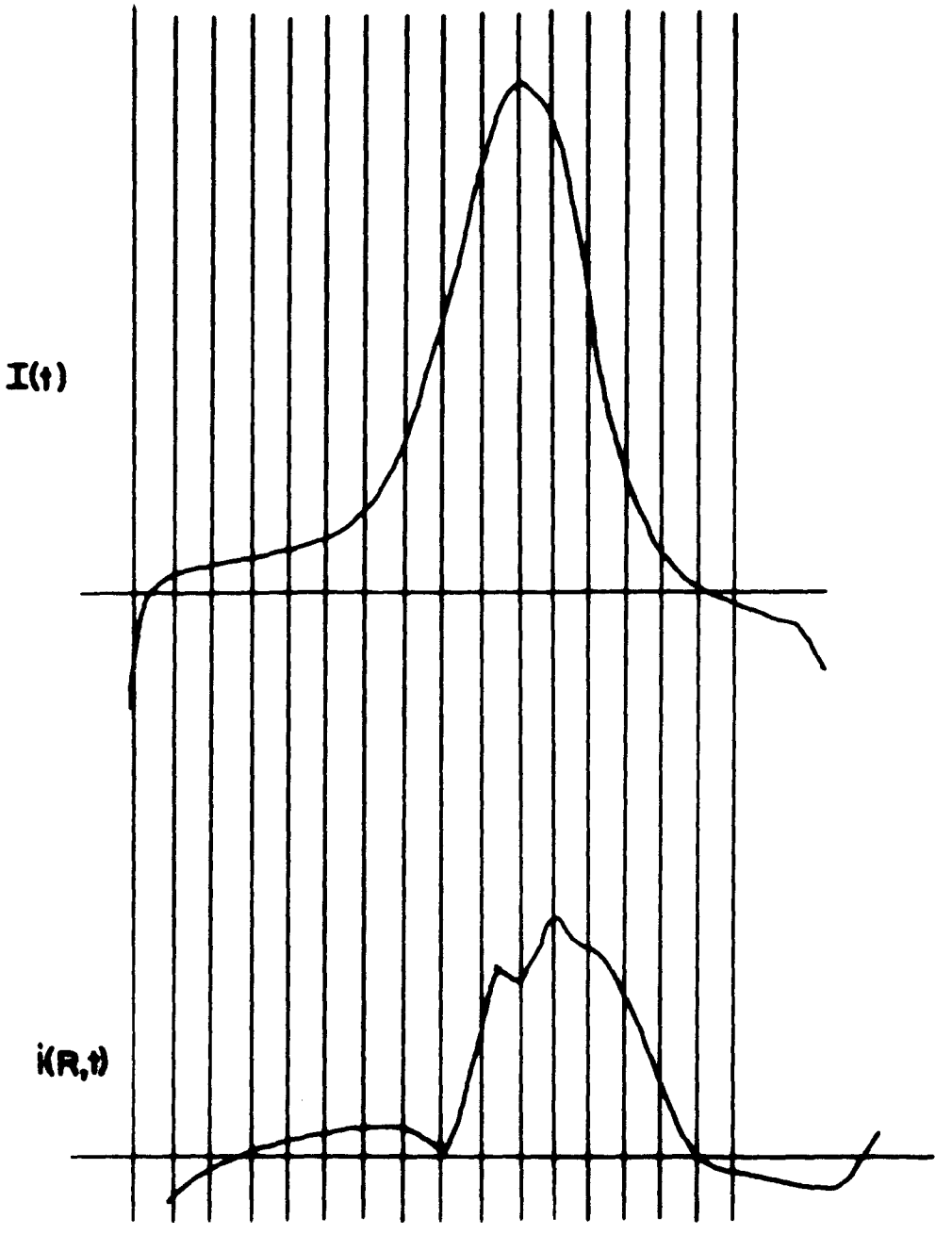

FIG. 15

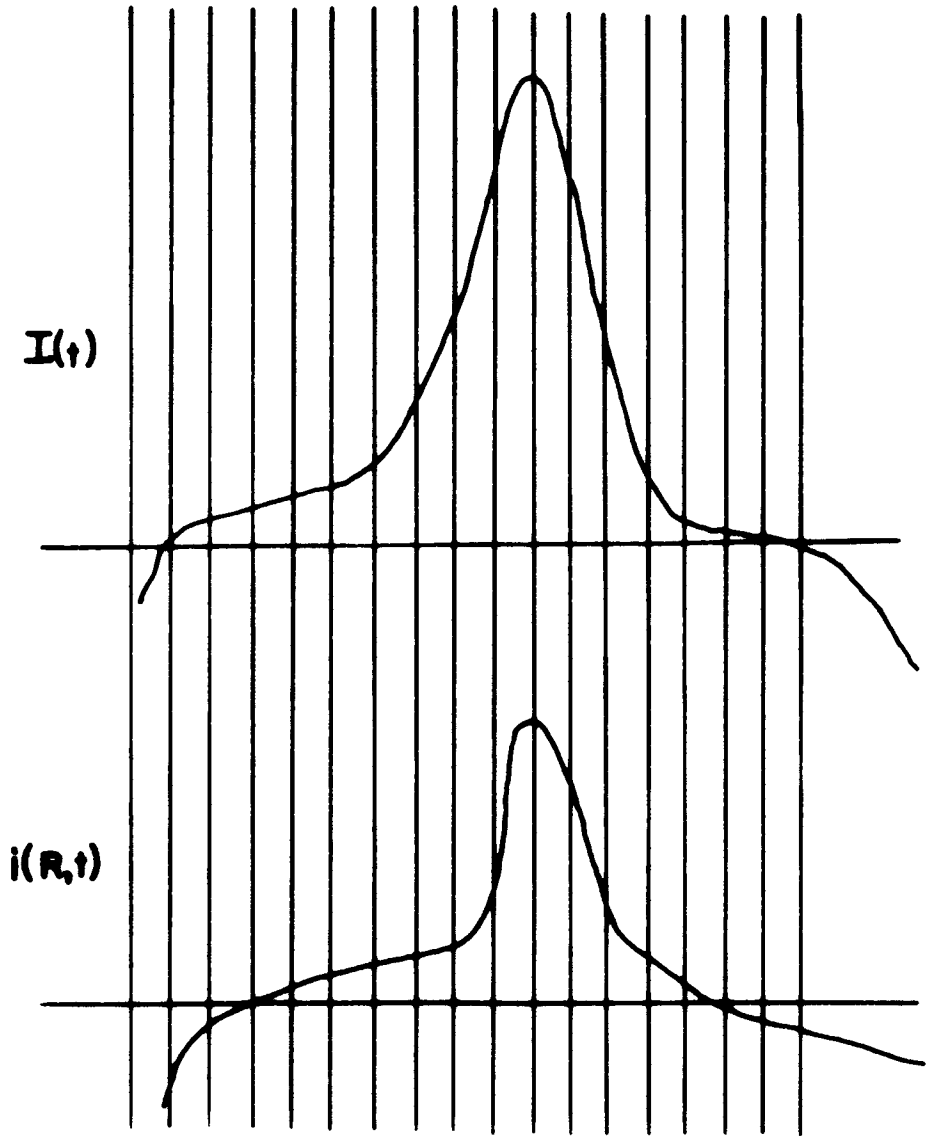

FIG. 16

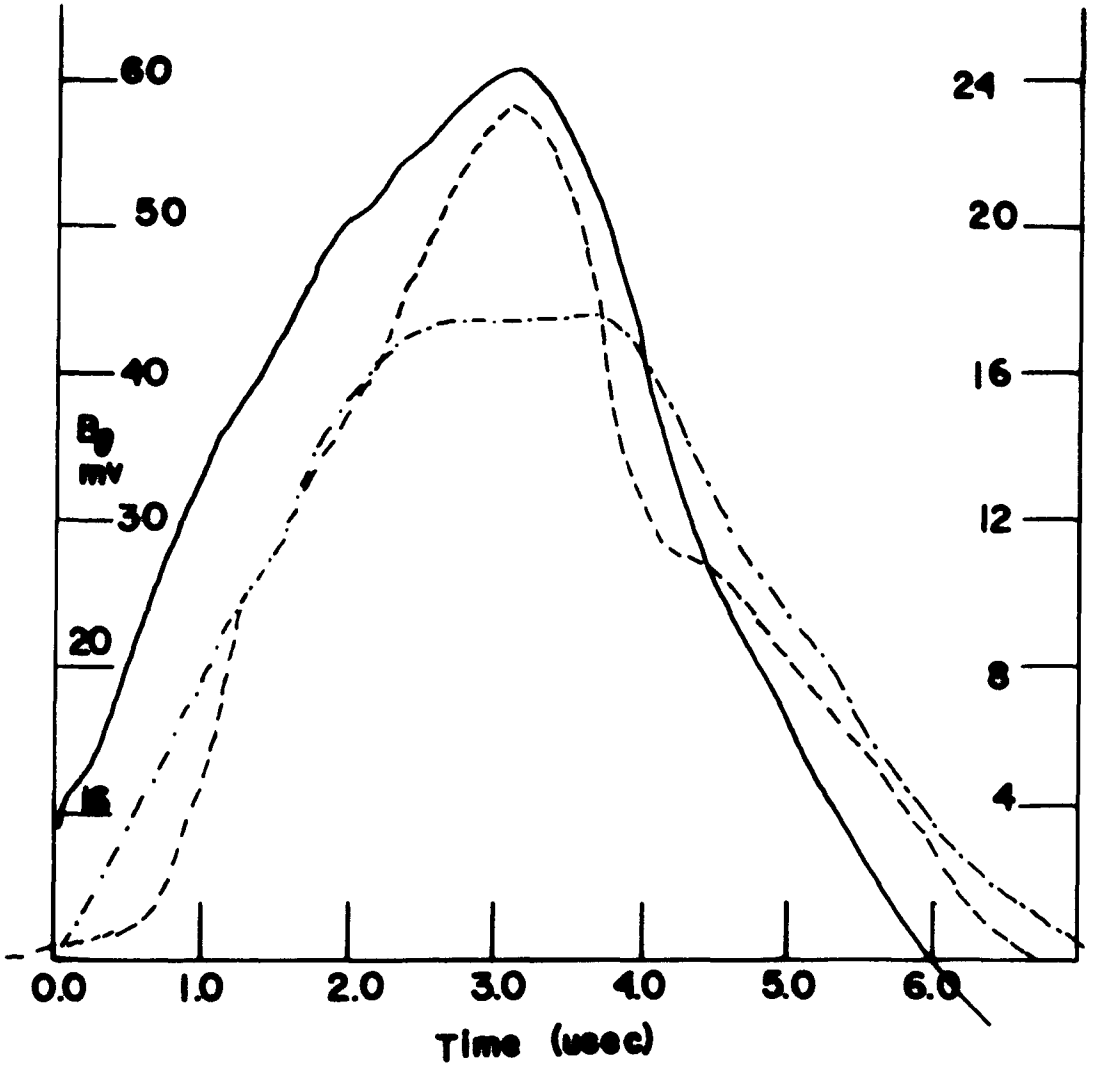

Loop	Rcm	Scale
1	0.89	24
2	1.52	60
3	2.15	60

1mv = 2.44gauss

FIG. 17

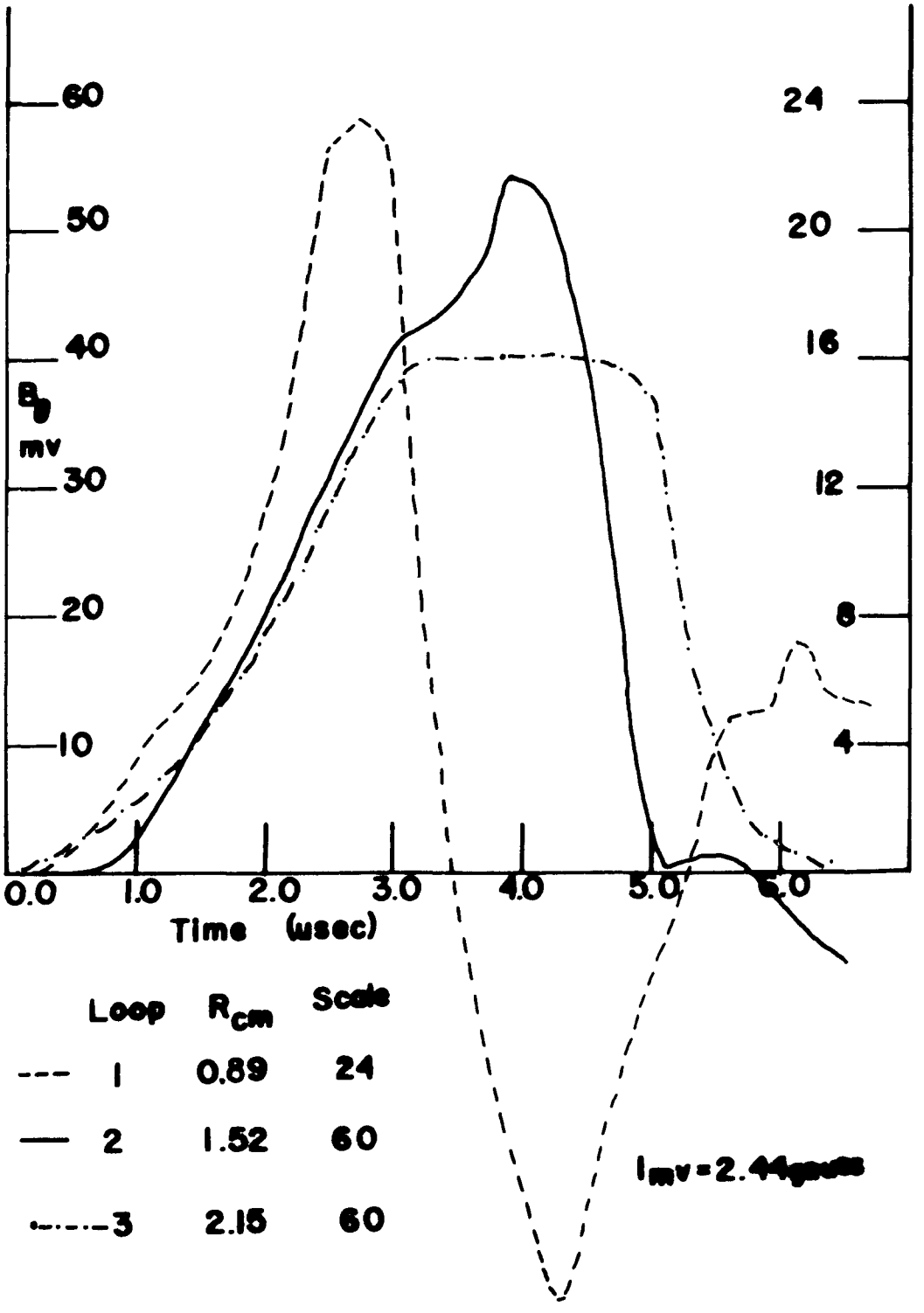
60
50
40
B_θ
mv
30
20
10
24
20
16
12
8
4
0.0
1.0
2.0
3.0
4.0
5.0
6.0
Time (μsec)
Loop
R_{cm}
Scale
--- 1 0.89 24
— 2 1.52 60
·---·---3 2.15 60
I_{mv}=2.44gauss

FIG. 18

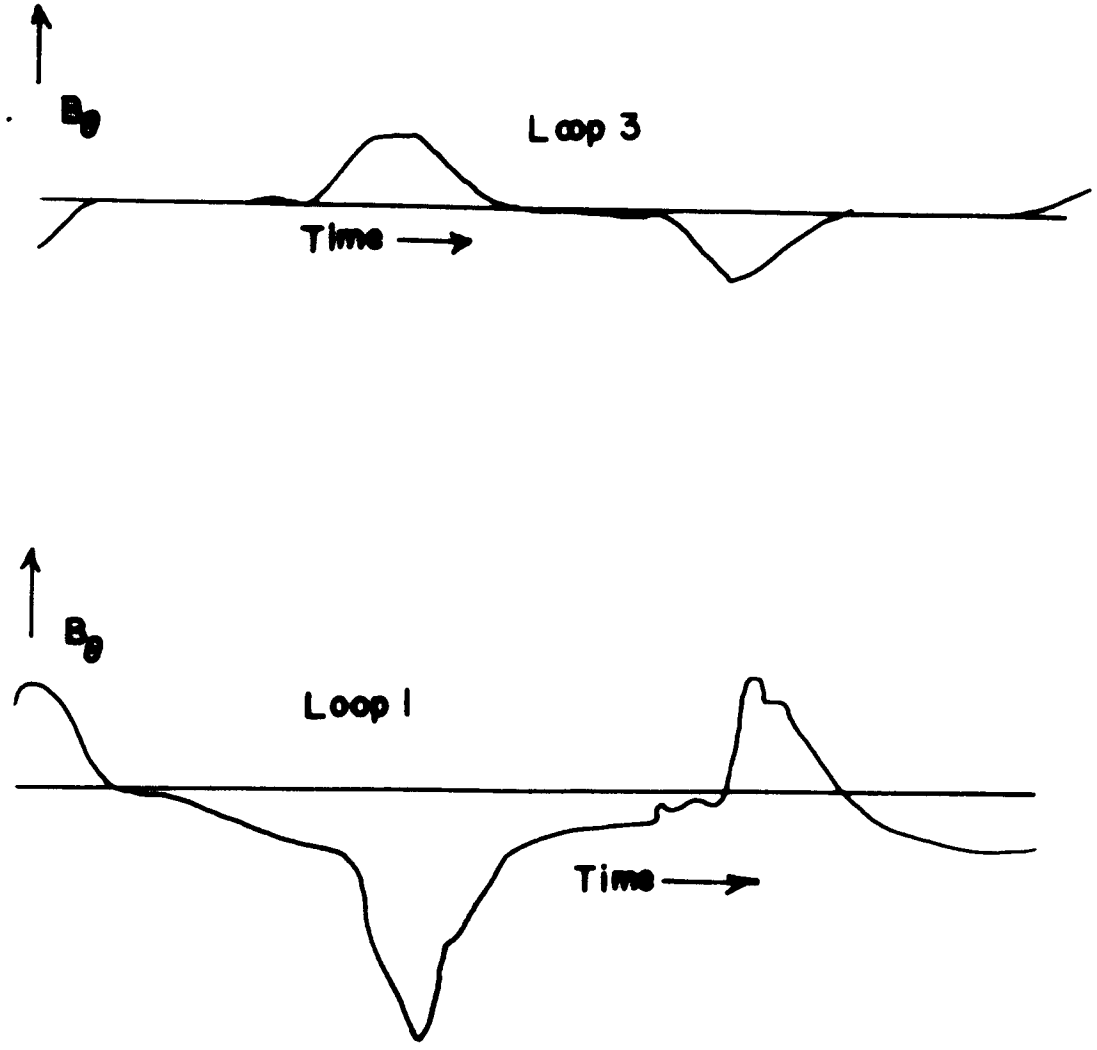

FIG. 19

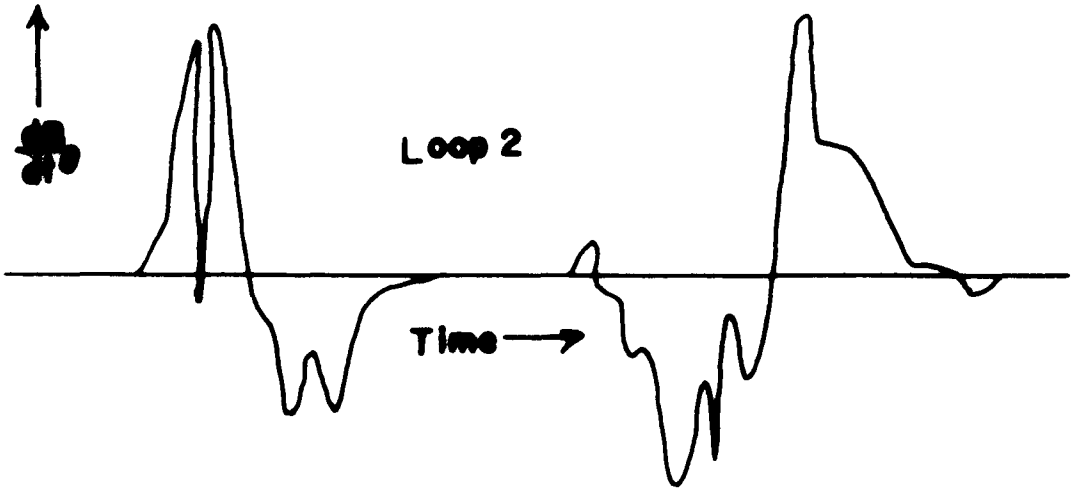

FIG. 20

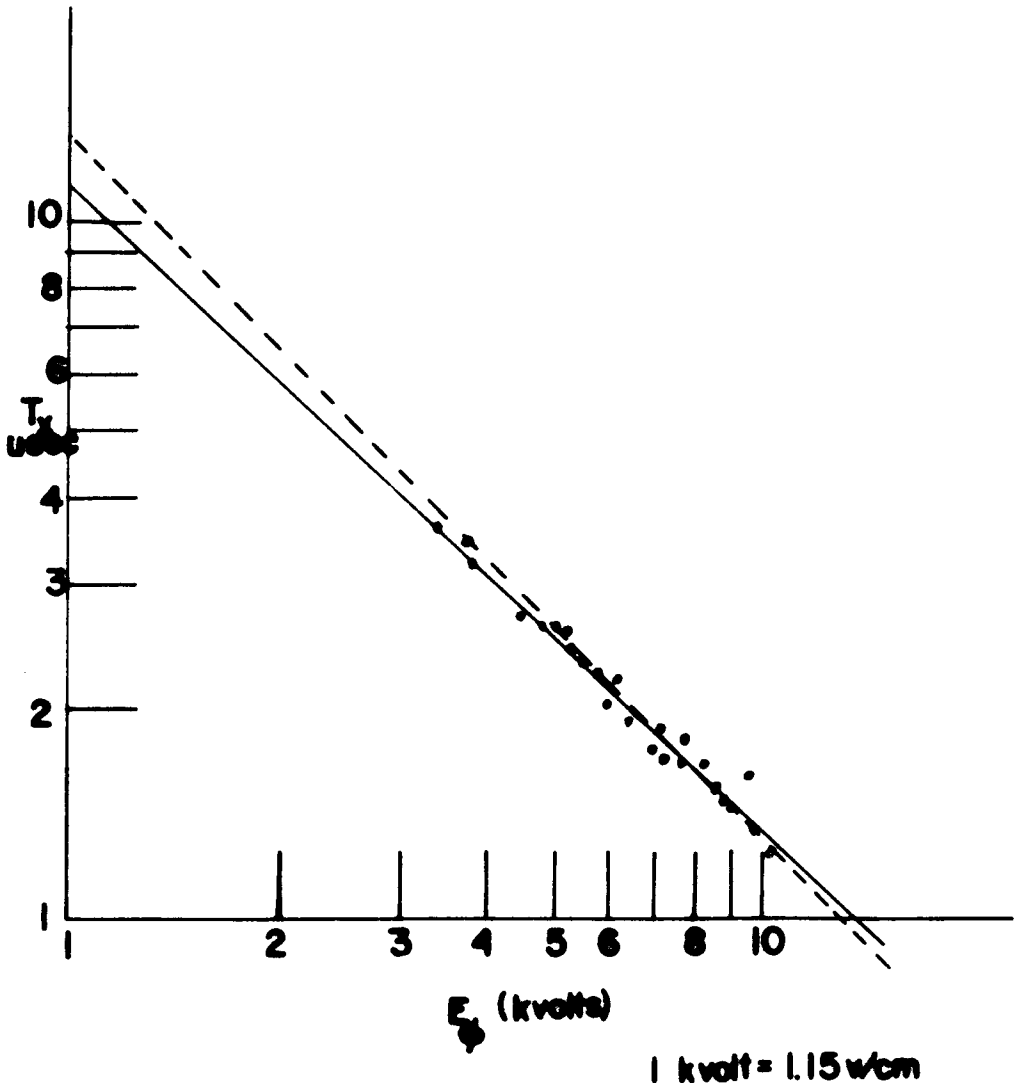

FIG. 21

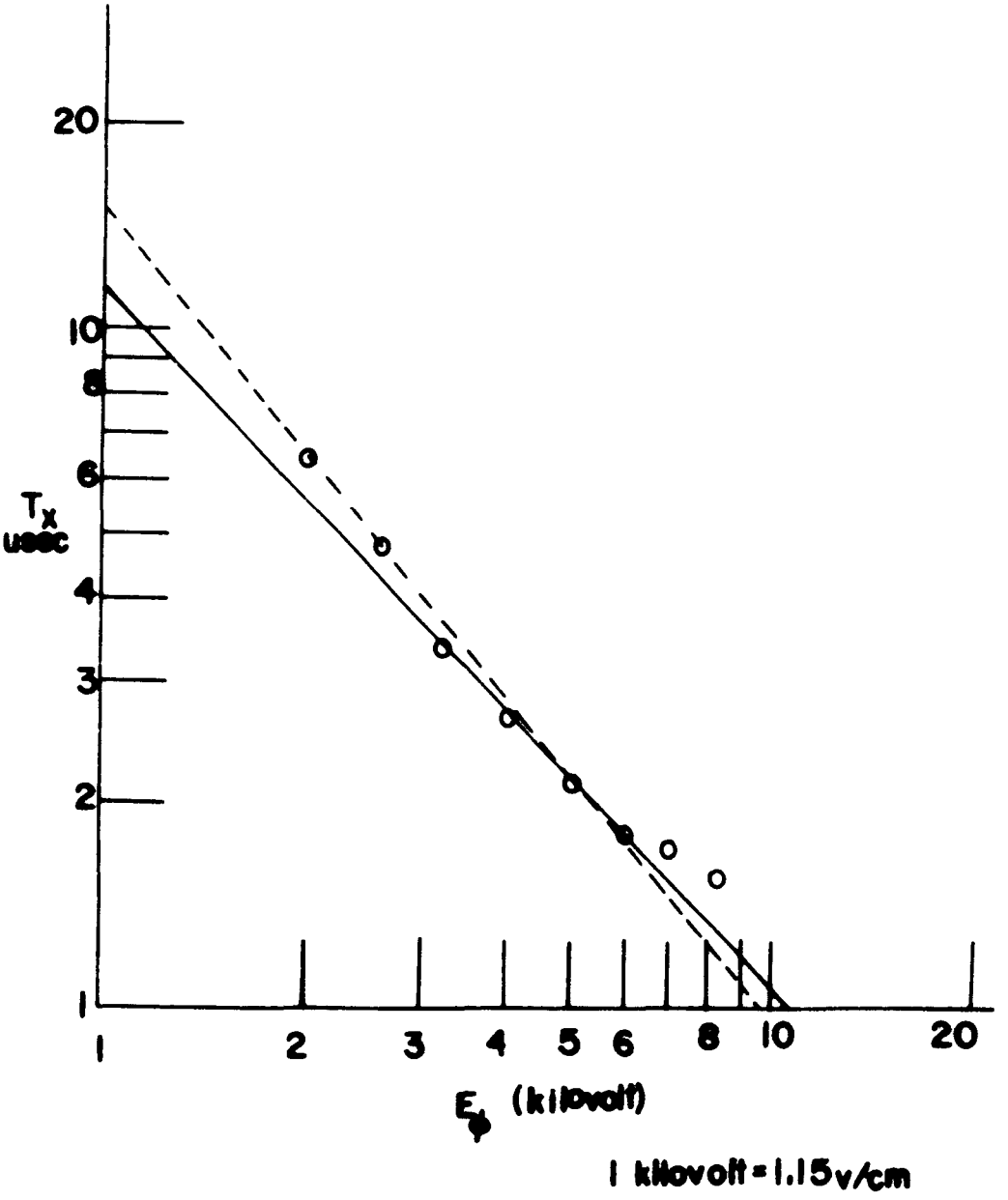
20
10
8
6
T_x usec
4
3
2
1
1
2
3
4
5
6
8
10
20
E_ϕ (kilovolt)
1 kilovolt = 1.15 v/cm

FIG. 22

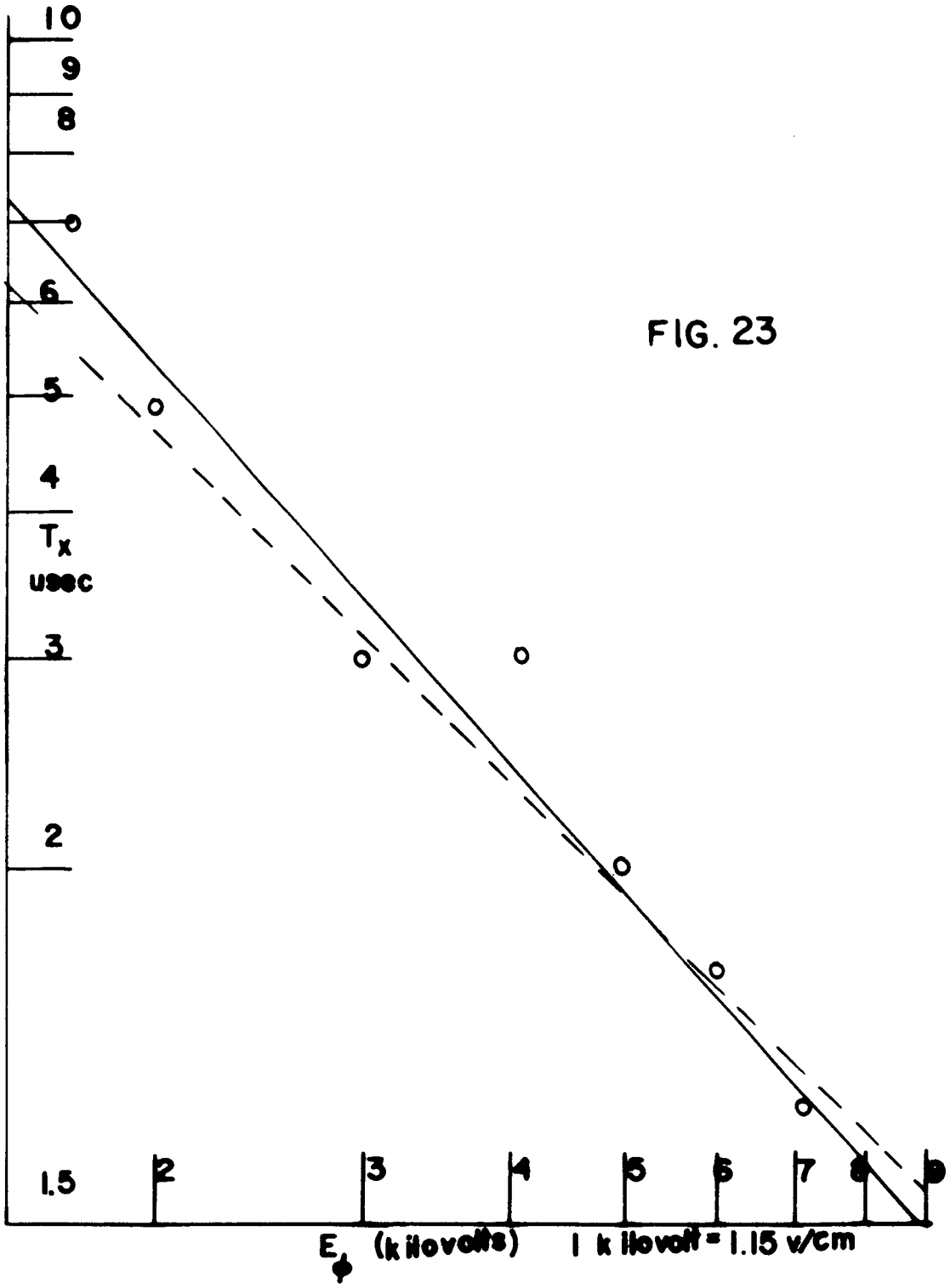
10
9
8
6
5
4
T_x
usec
3
2
1.5
2
3
4
5
6
7
8
E_ϕ (kilovolts)
1 kilovolt = 1.15 v/cm

FIG. 23

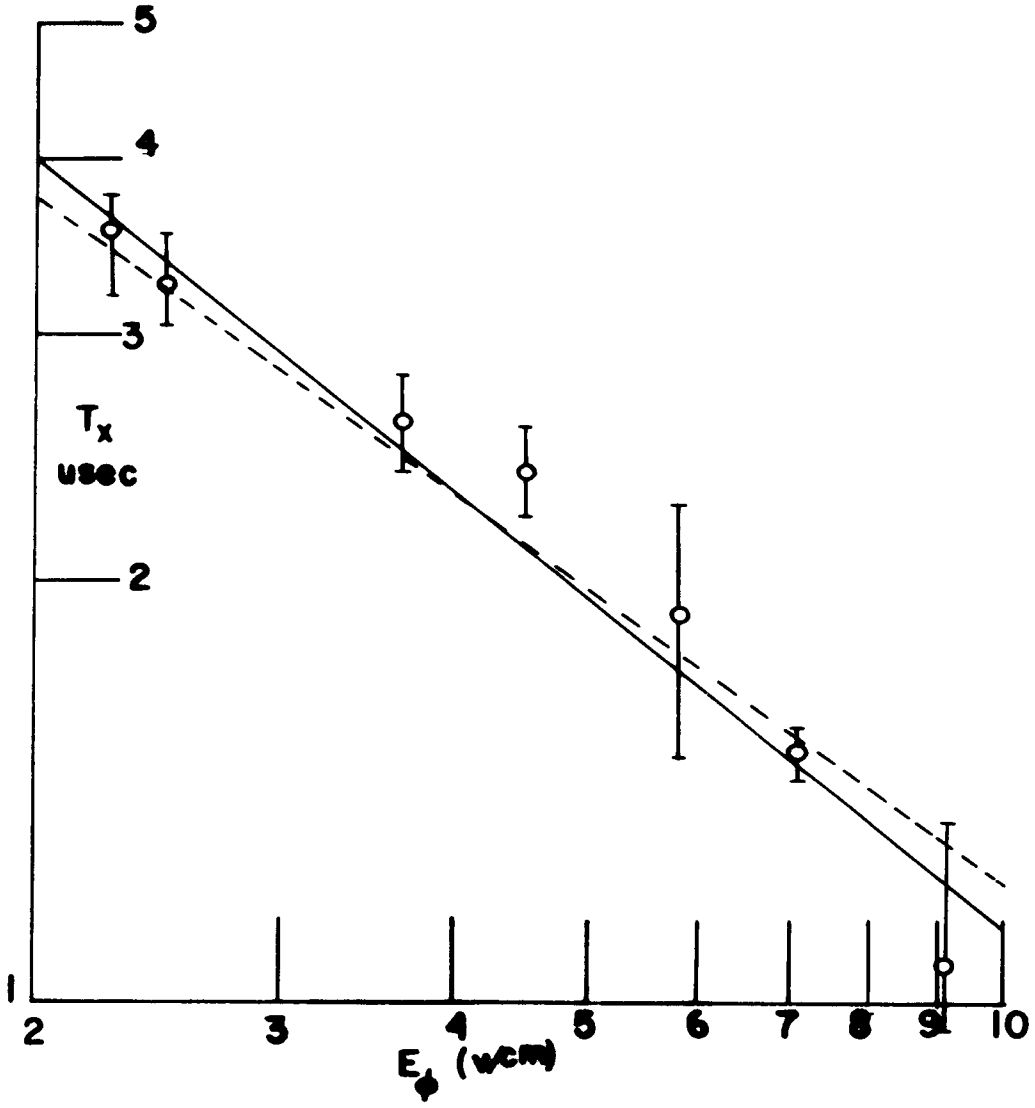

FIG. 24

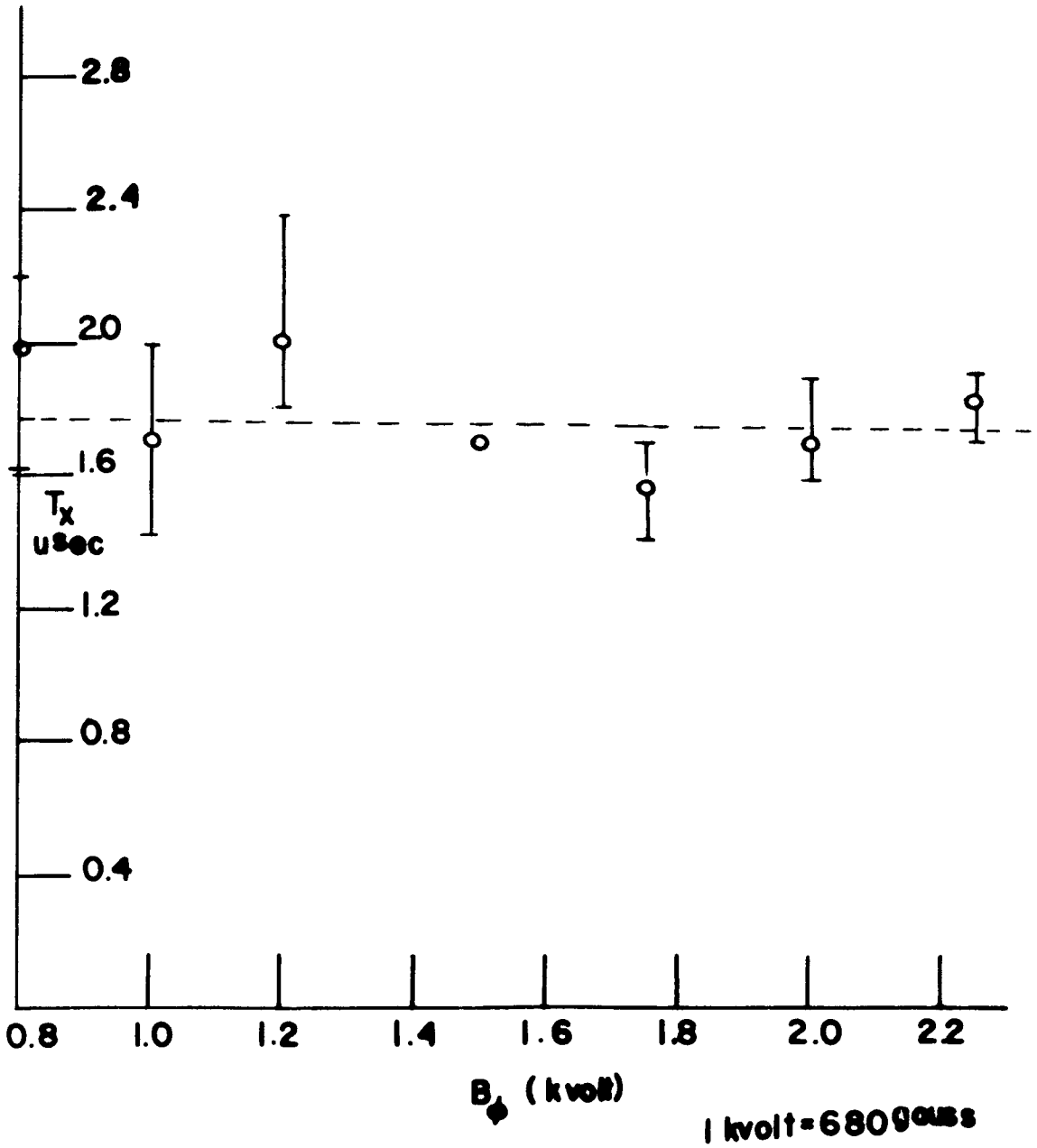
2.8
2.4
2.0
1.6
T_x usec
1.2
0.8
0.4
0.8
1.0
1.2
1.4
1.6
1.8
2.0
2.2
B_ϕ (kvolt)
1 kvolt=6800 gauss

FIG. 25

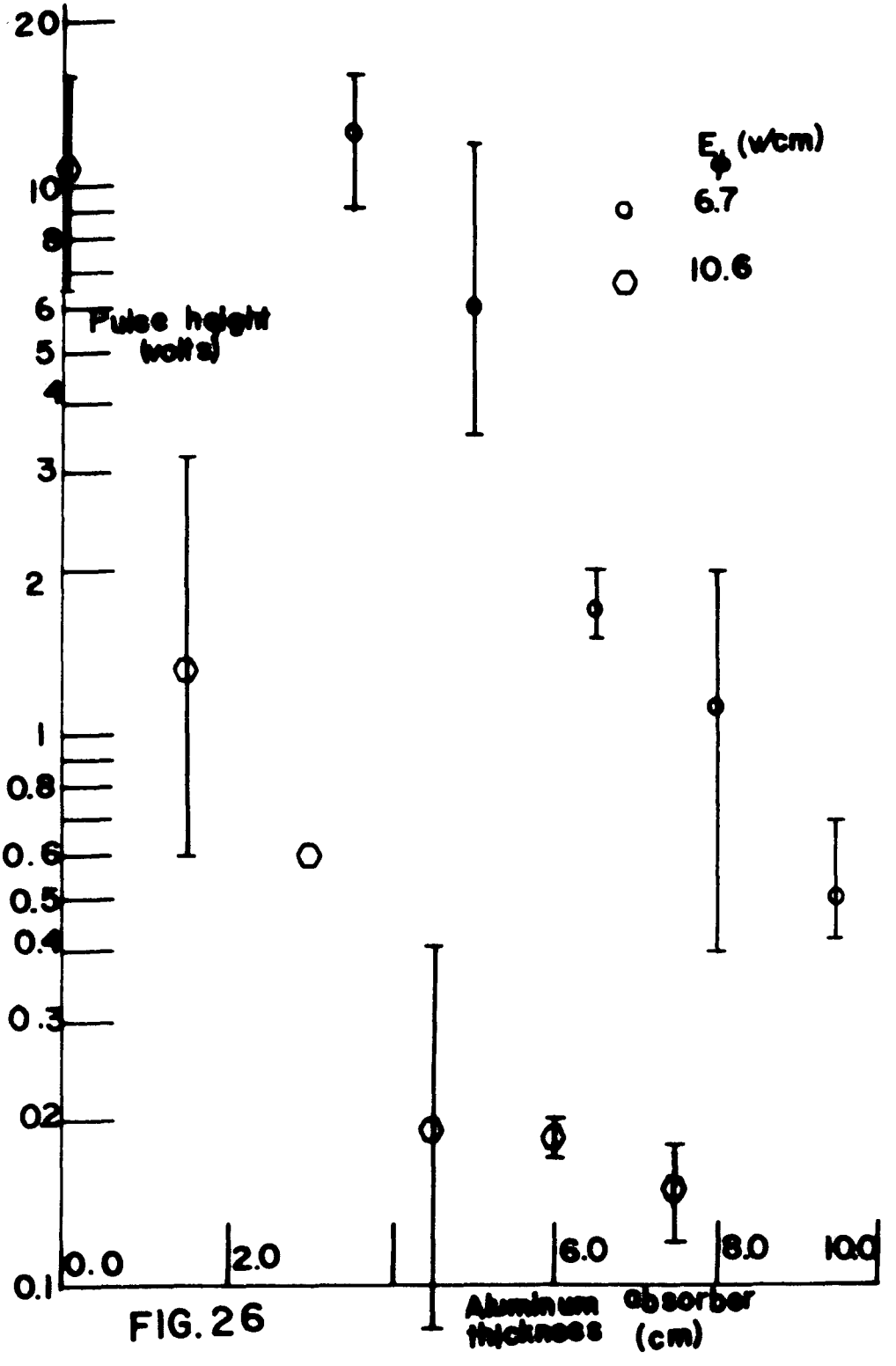
20
10
8
6
5
4
3
2
1
0.8
0.6
0.5
0.4
0.3
02
0.1
Pulse height (volts)
E (w/cm)
6.7
10.6
0.0
2.0
6.0
8.0
10.0
Aluminum absorber thickness (cm)

FIG. 26

FIG. 27

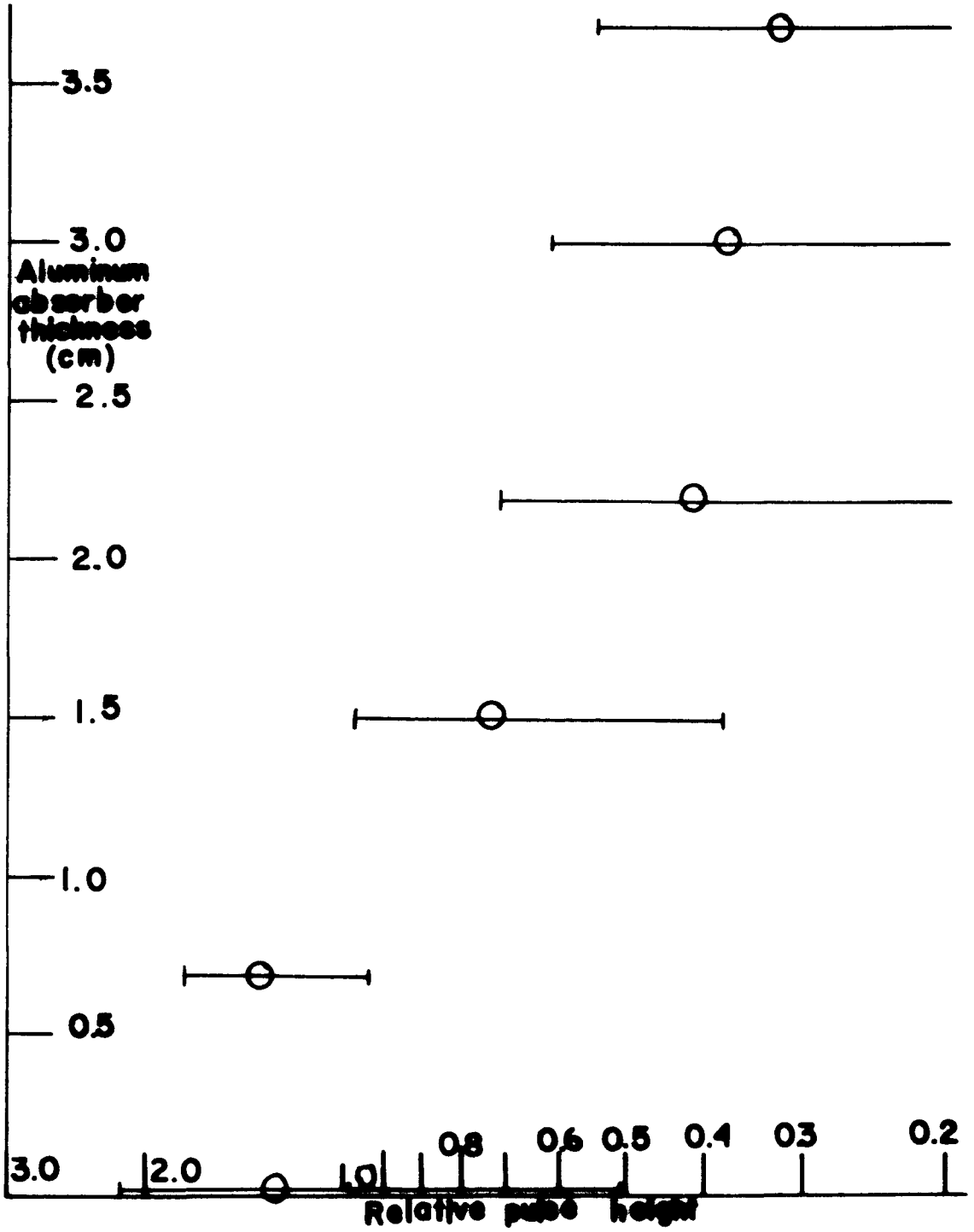
3.5
3.0
Aluminum absorber thickness (cm)
2.5
2.0
1.5
1.0
0.5
3.0
2.0
1.0
0.8
0.6
0.5
0.4
0.3
0.2
Relative pubic height

CHAPTER VII

THEORETICAL MODELS

In this chapter two theoretical models are considered. The first describes the ionization of neutral gas molecules by freely accelerated electrons and the resulting current. The second describes the conduction current as a function of time.

As discussed in previous chapters the plasma density build-up is rapid during the first acceleration cycle. It is of interest to see the role that the runaway electrons play in producing the ionization of the plasma. In the model used to calculate the ionization the following assumptions are made:

1. The azimuthal electric field is given by $E_\phi = E_0 \cos \omega t$.
2. The ionizing electrons are assumed to move along $\underline{E}_\phi$ with no scattering or energy loss during the ionization process.
3. Boundaries are neglected.
4. Collisions without ionization are neglected.
5. The electrons are initially at rest.

With these assumptions one can calculate the rate of ionization and the total current flow. The effect of a vertical drift due to electrons created out of phase with the

acceleration cycle is included in these calculations. These electrons are produced in the ionization process.

The basic scheme of the calculation is to add up all the electrons created by primary, secondary, tertiary, and higher order ionization processes. A single electron will produce the following number, $N_s(t)$, of secondary electrons in time t : $N_s(t) = \int_0^{t+t_m} v n_0 \sigma_i \, dt$

where t_m = quarter period of $E\phi$ (taken to be 4usec)

v = relativistic electron velocity

n_0 = neutral density

σ_i = ionization cross-section

The relativistic velocity is given by

$$v = \frac{eE_0/(\omega m) \cdot \sin \omega t}{\left[1 + \left(\frac{eE_0}{\omega m} \frac{1}{2}\right)^2 \sin^2 \omega t\right]^{1/2}}$$

The ionization cross section is obtained, as a function of v, from the experimental data of Tate and Smith.[1,2] For high velocities the empirical formula of Stuart and Gerjouy[3] is used. The integral for $N_s(t)$ is evaluated by the use of the Trapezoid rule. The size of the integration interval was determined by decreasing the interval until little or no change was observed in the integral value. The range of integration is broken into N intervals and the following terms are defined:

$$P_{ji} = \frac{n_o(t)\,\Delta T}{2}\left(v_{ji}\,\sigma_{ji} + v_{j(i-1)}\,\sigma_{j(i-1)}\right)$$

= the number of electrons produced in step i due to 1 electron created in step j where $i > j$ and

$$v_{jk} = \frac{u\, s_{k-j}}{\left[1 + u^2/c^2\, s_{k-j}^2\right]^{1/2}}$$

u = non-relativistic velocity at the end of the acceleration cycle = $< E_o/m\omega$

$s_{k-j} = \int_j^k f(t)\,dt$, $E_\phi = E_o f(t)$, ΔT = size of the time step, $n_o(t)$ = the neutral density which decreases in time.

The secondary ionization at the end of the i^{th} step is

$$i \geq 1 \qquad P_i^{(2)} = P_{oi}$$

For example, $P_3^{(2)} = P_{03}$ is the number of secondaries produced in time step 3 due to the electron created(in this case a primary electron) in time step 0. The total tertiary ionization at the end of the i^{th} step is

$$i \geq 2 \qquad P_i^{(3)} = P_1^{(2)} \sum_{k=2}^{i} P_{1k} + P_2^{(2)} \sum_{k=3}^{i} P_{2k} + \cdots + P_{i-1}^{(2)} P_{i-1,i}$$
$$= \sum_{m=1}^{i-1} \sum_{k=m+1}^{i} P_{om}^{(2)} P_{mk} = \sum_{m=1}^{i-1} \sum_{k=m+1}^{i} P_{om} P_{mk}$$

It is noted that each term in the sum arises from a secondary electron produced in the m^{th} time step by the original primary electron.

The number of electrons produced by secondary electrons from the $i-1$ to i time step is

$$Q_i^{(2)} \equiv P_i^{(2)} - P_{i-1}^{(2)} = \sum_{m=1}^{i-1} \sum_{k=m+1}^{i} P_{om} P_{mk} - \sum_{m=1}^{i-2} \sum_{k=m+1}^{i-1} P_{om} P_{mk}$$

$$= P_{o\,i-1}\,P_{i-1\,i} + \sum_{m=1}^{i-2}\sum_{l=m+1}^{i} P_{om}P_{ml} - \sum_{m=1}^{i-2}\sum_{l=m+1}^{i-1} P_{om}P_{ml}$$

$$= P_{o\,i-1}\,P_{i-1\,i} + \sum_{m=1}^{i-2} P_{om}P_{mi}$$

Thus $Q_i^{(3)} = \sum_{m=1}^{i-1} P_{om}P_{mi} = \sum_{m=1}^{i-1} P_i^{(2)}P_{mi}$

Just as each secondary electron produced tertiary electrons, the tertiary electrons produced will create the next generation of electrons. It is assumed that all the $Q_i^{(3)}$ electrons are created at the same time. Thus the total production of fourth generation electrons per unit time is given by: $P_i^{(4)} = Q_2^{(3)}\sum_{l=3}^{i} P_{2l} + Q_3^{(3)}\sum_{l=4}^{i} P_{3l} + \ldots + Q_{i-1}^{(3)}P_{i-1\,i}$

$$P_i^{(4)} = \sum_{m=2}^{i-1}\sum_{l=m+1}^{i} Q_m^{(3)}P_{ml}$$

For the next generation one has $Q_i^{(4)} = \sum_{m=2}^{i-1} Q_m^{(3)}P_{mi}$

The general expressions for the cascade are as follows:

total ionization by the end of the i^{th} step due to the n^{th} generation $P_i^{(n)} = \sum_{m=n-2}^{i-1}\sum_{l=m+1}^{i} Q_m^{(n-1)}P_{ml}$

ionization between the $i-1$ and i steps due to the n^{th} generation $Q_i^{(n)} = \sum_{m=n-2}^{i-1} Q_m^{(n-1)}P_{mi}$

where $i>1$ and $n>2$

(For $n = 2$ $P_i^{(2)} = P_{oi}$ and $Q_i^{(2)} = P_{oi}$, $i \geq 1$)

total ionization at the end of the I^{th} time step due to all N generations $T_I = \sum_{n=3}^{N} P_I^{(n)} + \sum_{i=1}^{I} P_{oi}^{(2)} = \sum_{n=3}^{N}\sum_{i=1}^{I} Q_i^{(n)} + \sum_{i=1}^{I} P_{oi}^{(2)}$

By computing the velocity for the electron produced at different time steps a net current can be computed. One can also include drifts due to the betatron restoring force and the centrifugal drift. Assuming that the net azimuthal current flow is given by the difference between the azimuthal current and the drift current one can calculate the dependence of the ionization induction current maxima on $E\phi$ and $B\phi$.

Figure 1 shows the variation of the electron velocity with time for a primary electron. The secondary ionization per unit time (number of secondaries produced between two time steps) and the total secondary ionization is also shown for hydrogen. It is noted that the electron velocity becomes relativistic in about 0.3 usec. for the maximum value of the electric field strength, $E\phi$, equal to 20v/cm. Figure 2 shows the ionization of hydrogen gas for different initial neutral densities and primary electron densities. Here $B\phi$ = 2Kgauss and the maximum electric field strength is 20v/cm. Figure 3 shows the effect of different primary electron densities on the time to completely ionize the gas within 1.0usec. Different neutral densities are used and $B\phi$ = 2Kgauss and $E\phi$ = 20v/cm. Figure 4 shows the computed current density as a function of time for $B\phi$ = 2 Kgauss and

$E\phi$ = 1,2, and 3v/cm for hydrogen. It is of interest to see how the current reaches a maximum and then levels off or decreases rapidly. It is observed that for higher $E\phi$ this trend continues. The magnitude of the maximum current does not increase with increasing $E\phi$ but from 1 to 20 v/cm appears to be about constant ($\pm$10%). Figure 5 shows log-log plots of the maximum current time, t_m versus $B\phi$ and $E\phi$. t_m shows the following approximate dependence on $E\phi$ and $B\phi$: $t_m = k B\phi^{1.07 \pm 0.07}$ and $t_m = k' E\phi^{-1.15 \pm 0.15}$ In these cases the electron mass is used in the drift current calculations which assumes free diffusion of the electrons across the azimuthal magnetic field. If instead, one assumes that the electrons drift across the azimuthal magnetic field at the rate of the ions, which is roughly the case in ambipolar diffusion, then one would calculate the rate of ion drift for the purpose of finding the rate of current loss. When the ion drift is considered to be responsible for diffusion losses t_m becomes independent of $B\phi$ but having the same $E\phi$ dependence as above. Ionization in argon has also been studied but to a lesser extent than in hydrogen. Similar results occur.

Thses calculations show the rapid build-up of ionization due to freely accelerated electrons. Also observed is a parametric dependence of current maxima on external

fields due to ionization and drift as well as a constant resistivity, i.e., I_{max} independent of $E\phi$. The range of $E\phi$ and $B\phi$ are 1v/cm to 20v/cm and 0.85Kgauss to 20. Kgauss, respectively.

The conduction current exhibits anomalously high resistivity and exhibits a non-linear wave form. The size of the conduction current affects the position of the equilibrium orbit and may affect the plasma temperature from the point of view of resistive heating. It is of interest, therefore, to have a better understanding of the dependence of conduction current on time. To do this the plasma betatron is viewed as an air core transformer (see chapter IV) and coupled circuit equations are used to describe the current flow. This model must be used cautiously since the plasma resistance and inductance are not necessarily constants.

It is convenient for certain calculations to consider the secondary circuit to be uncoupled from the primary circuit. The plasma current, i , the plasma resistance, r , the plasma inductance, l , are related to the applied voltage (supplied by the betatron primary) by the following: $ir + l\frac{di}{dt} = V(t)$

If one assumes that $V(t)$ is given by $V(t) = V_0 \cos\omega t\, e^{-\delta t}$

The differential equation for i has the form

$$\frac{di}{dt} + f(t)\, i = r(t)$$

and has the solution $i = e^{-h}\left[\int e^{h} r\, dt + C\right]$ where $h = \int f\, dt$. For the initial condition that $i(0) = 0$ one finds that $i(t)$ is given by:

$$i_e(t) = \frac{V_0 e^{-\gamma/2(\omega t)}}{(r-\gamma\ell)^2 + (\omega t)^2}\left\{(r-\gamma\ell)\cos\omega t + \omega\ell\sin\omega t - (r-\gamma\ell)e^{\left(-\frac{r}{L}+\frac{\gamma}{2}\right)\omega t}\right\}$$

where it is assumed the secondary resistance is constant. One sees that of the five parameters which $i_e(t)$ depend on, V_0 , γ , ω , r_e , and ℓ the first three are determined experimentally and depend only on the primary circuit. The secondary electron resistance is assumed to depend on the cross sectional area of the current column and the resistivity. If the resistivity is assumed to follow the classical $T^{-3/2}$ law one can assign an electron temperature and a current channel radius to fix the value of r_e . The secondary inductance is assumed to depend only on the current column radius. This assumes an approximate uniform current distribution and an approximate constant major radius. Thus the current depends on two plasma parameters which are the plasma current column size and the electron temperature. As discussed in chapter VI the current form is digitized and compared to the electric field. For five different cases, (called data sets 1,2,3,4, and 5), the time of the third cycle current maxima is measured and compared with the electric field maximum time as follows:

Data set	Electric field	Argon 1	Argon 2	H 3	H 4	H 5
$\mathcal{L}_m$ (usec)	50.50	59.20	59.79	58.33	57.50	55.44
I_m (amps)		1649	1487	2511	881.0	523.3

Measuring the phase difference between the current peak and the electric field and making use of the current amplitude one can use the expression for $i_e(t)$ to find the value of the electron temperature γ_e and current radius $\mathcal{R}$ which fits the above data. The results are

Data set	1	2	3	4	5
γ_e (ev)	50	135	3.9	2.2×10^3	1.5×10^4
$\mathcal{R}$ (cm)	0.19	0.10	1.2	0.0085	0.0015

It is seen that only trial 3 gives a temperature and radius consistant with measured temperature and radius. It is significant that for this trial the current form is most sinusoidal in appearance. This correspondence is what one would expect since the resistance one uses for $i_e(t)$ has a constant value implying a sinusoidal waveform. For a variation of 0.25 usec in the relative phase of trial 1 with respect to the electric field a change in the current radius of ten percent with a similar change in the electron temperature occur. The sensitivity to variations in the current is the same. Thus the results are qualitatively the same within the accuracy of the measurement of the

current maximum with respect to the electric field maximum and within the current maximum measuring accuracy.

The same calculations are carried out using the coupled circuit equations. Qualitatively the results are the same

Data set	1	2	3	4	5
T_e (ev)	137	400	11.4	1.6×10^{4}	5.5×10^{5}
$\mathcal{R}$ (cm)	0.12	0.062	0.83	2.2×10^{-3}	1.1×10^{-4}

It is noted that in addition to having temperatures and radii not near the experimental values, trials 1,2, 4 and 5 must have drift velocities which are near the speed of light or higher due to the small value of $\mathcal{R}$. The drift velocity for trial 3 is 1.2×10^{7} cm/s. Also one requires that the electron cyclotron radius be smaller than or equal to the radius of the current channel. Trials 4 and 5 do not fit this condition.

The uncoupled model for the electron current can readily be used to estimate the effect of the finite rise time of E_ϕ on the position of the current maxima and their magnitudes. Let t_R be the time it takes for E_ϕ to reach its initial maximum value. The external voltage time dependence can be divided into two regions

$$V = V_0\, t/t_R\, e^{-\gamma t}\cos\omega t \qquad 0 \le t \le t_R$$

$$V = V_0\, e^{-\gamma t}\cos\omega t \qquad t \ge t_R$$

In this case the solution for $i(t)$ is

$$i(t) = \frac{V_0 e^{-\frac{\gamma}{\omega}\omega t}}{\tau_R A}\left\{ a\tau\cos\omega t + b\tau\sin\omega t - \frac{\rho}{A}\left[(a^2-b^2)\cos\omega t + 2ab\sin\omega t\right] + \frac{\rho}{A}(a^2-b^2)e^{\left(-\frac{\tau}{\omega\tau}+\frac{\gamma}{\omega}\right)\omega t}\right\}$$

where $t \le t_R$. For $t \ge t_R$ one has the following:

$$i(t) = \frac{V_0}{A} e^{-\frac{\gamma}{\omega}\omega t}\left\{ a\cos\omega t + b\sin\omega t + C e^{-\frac{\tau}{\omega\tau}\omega t + \frac{\gamma}{\omega}\omega t}\right\}$$

where $A = a^2+b^2$; $a = r - \gamma\rho$; $b = \omega\rho$

$$C = \frac{\rho}{A\tau_R}(a^2-b^2)\, e^{-\left(-\frac{\tau}{\omega\tau}+\frac{\gamma}{\omega}\right)\omega t_R} \cdot \frac{\rho}{\tau_R A}\left\{(a^2-b^2)\cos\omega t_R + 2ab\sin\omega t_R\right\}$$

For the third current maximum and t_R =1.0 usec the maximum time of the current and the current amplitude are changed by less than 0.1 percent with respect to the t_R = 0 case. It is concluded that for the third and subsequent cycles the finite rise time of $V(t)$ has no significant effect on the time of occurence of the current maxima or the current amplitude.

For a high enough current (trial 3) it is seen that the linear theory gives good agreement with experimental results. For lower currents, however, the linear theory fails to show any agreement with the experimental results. In order to account for the non-linear current forms the electrons are assumed to diffuse out of the current stream by ambipolar diffusion. In order to calculate the ambipolar diffusion rate the ion motion must be calculated as a function of time. The transverse ion motion is given by

$$W_D = \frac{\frac{1}{2} m_i V_{i\perp}^2}{R q B_{o\phi}} + \frac{1}{q}\left(\frac{m_i V_{i\phi}^2}{R} - q V_{i\phi} B_z\right)$$

where $v_{i\perp}$ = ion thermal velocity perpendicular to

R = major radius of current column

$B_{o\phi}$ = quasi-static longitudinal magnetic field

$v_{i\phi}^{(t)}$ = ion velocity parallel to $B_{o\phi}$

$B_z^{(t)}$ = betatron magnetic field

In order to find $v_{i\phi}$ the ion current is first found. From this an average drift velocity is found which is then used to approximate $v_{i\phi}$. In order to calculate the ion current it is assumed that the ion current obeys the equation

$$i_i r_i + l_i \frac{di_i}{dt} = V(t)$$

However, due to the presence of the electron current one must assume a mutual inductance M between the ion current loop and the electron current loop. Thus the current equations for the ions and electrons become

$$i_i r_i + l_i \frac{di_i}{dt} + M_{ie} \frac{di_e}{dt} = V_i(t)$$

$$i_e r_e + l_e \frac{di_e}{dt} + M_{ei} \frac{di_i}{dt} = V_e(t)$$

These equations are simplified due to the fact that

$$V_i = V_e = V$$

$$l_i = l_e = l$$

$$M_{ei} = M_{ie} = l$$

These last two equations follow from the fact that the ion and electron current loops occupy the same space. Thus the magnetic flux produced by the current flow passes through the same region of space with the same spatial dependence

for each loop. Since these are the factors which determine inductance, the self-inductance will be the same for the ions and electrons, $\ell_e = \ell_i \equiv \ell$. Also, $M_{ie} = \ell$, for the same reason, the circuits overlap.

Taking the derivatives of the above current equations with respect to time allows one to de-couple the ion equation and the electron equation. One obtains the following equations for the electron current and ion current:

$$i_i r_i + \frac{di_i}{dt} \ell \left(1 + \frac{r_i}{r_e}\right) = V(t)$$

$$i_e r_e + \frac{di_e}{dt} \ell \left(1 + \frac{r_e}{r_i}\right) = V(t)$$

These equations hold for any overlapping two beam system. In this case it will be shown that $r_i >> r_e$ so that one obtains the equations

$$i_i r_i + \ell \frac{r_i}{r_e} \frac{di_i}{dt} = V(t)$$

$$i_e r_e + \ell \frac{di_e}{dt} = V(t)$$

Substituting $I_i = \frac{r_i}{r_e} i_i$ one obtains for the ion equation $r_e I_i + \ell \frac{dI_i}{dt} = V(t)$

But this equation is identical to the electron equation which means that the ion current is in phase with the electron current but reduced in size by a factor of r_e/r_i, that is, $i_i = \frac{r_e}{r_i} i_e$ Thus one need only consider the solution to the electron current equation to find the longitudinal ion current as a function of time. It is noted that these results hold true for any $V(t)$.

In particular $V(t)$ could depend on the secondary current, as in a coupled circuit model of the plasma betatron, and these results would still hold true.

One can derive the fact that $n_i = \frac{m_i}{m_e} n_e$ by considering some of the results obtained by Dreicer[4] for a fully ionized plasma. One considers the individual Boltzmann equations for the ions and electrons

$$\frac{\partial F_e}{\partial t} + \underset{\sim}{u} \cdot \underset{\sim}{\nabla} F_e + \left(-\frac{e}{m}\right)\left(\underset{\sim}{E} + \underset{\sim}{u} \times \underset{\sim}{B}\right) \cdot \underset{\sim}{\nabla}_{\underset{\sim}{u}} F_e = \left(\frac{\partial F_e}{\partial t}\right)_u$$

$$\frac{\partial F_i}{\partial t} + \underset{\sim}{u} \cdot \underset{\sim}{\nabla} F_i + \left(\frac{e}{m}\right)\left(\underset{\sim}{E} + \underset{\sim}{u} \times \underset{\sim}{B}\right) \cdot \underset{\sim}{\nabla}_{\underset{\sim}{u}} F_i = \left(\frac{\partial F_i}{\partial t}\right)_u$$

Assuming that only small angle collisions are the ones of importance, the collision terms are evaluated by the Fokker-Planck approximation[5] which gives

$$\left(\frac{\partial F_\alpha}{\partial t}\right)_u = \sum_{\beta = e,i} \left\{ -\frac{\partial}{\partial u_k}\left[F_\alpha \langle \Delta u_k \rangle_{\alpha\beta}\right] + \frac{1}{2}\frac{\partial^2}{\partial u_k \partial u_j}\left[F_\alpha \langle \Delta u_k \Delta u_j \rangle_{\alpha\beta}\right] \right\}$$

$\alpha = e, i$ $\qquad \langle \Delta u_k \rangle_{\alpha\beta} = \frac{\partial H_{\alpha\beta}}{\partial u_k}$; $\qquad \langle \Delta u_k \Delta u_j \rangle_{\alpha\beta} = \frac{\partial^2 G_{\alpha\beta}}{\partial u_k \partial u_j}$

$$G_{\alpha\beta}(\underset{\sim}{x}, \underset{\sim}{u}, t) = \Gamma_\alpha \int F_\beta(\underset{\sim}{x}, \underset{\sim}{u}', t)\, d^3\underset{\sim}{u}'$$

$$w = |\underset{\sim}{u} - \underset{\sim}{u}'| \; ; \quad \Gamma_\alpha = 4\pi \left(\frac{e^2}{4\pi\varepsilon_0 m_\alpha}\right)^2 \log_e\left(\frac{\lambda_D}{p_0}\right)$$

λ_D =Debye length, p_0 = average impact parameter for 90° deflection. The current $\underset{\sim}{j}$ is given by

$$\underset{\sim}{j} = n_e\left(\underset{\sim}{V}_i - \underset{\sim}{V}_e\right)$$

and

$$\underset{\sim}{V}_\alpha = \frac{1}{n_e}\int F_\alpha \, \underset{\sim}{u}\, d^3\underset{\sim}{u}$$

Taking the first moment of the Boltzmann equations for the

ions and electrons yields

$$m_e \frac{\partial \underset{\sim}{v}_e}{\partial t} + e\underset{\sim}{E} = \frac{m_e}{n}\int \underset{\sim}{F}_e(\underset{\sim}{u},t)\,\underset{\sim}{\nabla}_{\underset{\sim}{u}} H_{ei}\, d^3\underset{\sim}{u}$$

$$m_i \frac{\partial \underset{\sim}{v}_i}{\partial t} - e\underset{\sim}{E} = \frac{m_i}{n}\int \underset{\sim}{F}_i(\underset{\sim}{u},t)\,\underset{\sim}{\nabla}_{\underset{\sim}{u}} H_{ie}\, d^3\underset{\sim}{u}$$

The integrals in the above two equations represent the average dynamic friction force acting on the electrons and ions. The sum of these two terms are zero as can be shown directly. Thus by adding the two moment equations one has

$$m_e \frac{\partial v_e}{\partial t} = -m_i \frac{\partial v_i}{\partial t} \qquad \text{or} \qquad m_e v_e = -m_i v_i$$

for appropriate initial conditions. This is just what one expects in a steady state situation. Denoting γ_i and γ_e as the effective collision frequencies for the ions and electrons respectively, the collision terms may be written as $m_e v_e \gamma_e = -m_i v_i \gamma_i$. Thus $\gamma_e = \gamma_i$ or the ion and electron collision frequencies for momentum exchange are equal in a fully ionized plasma in steady state.

The resistivity can be related to the electric field in the following way

$$\underset{\sim}{E} = \rho\,\underset{\sim}{J}$$

$$\underset{\sim}{J} = q\,\underset{\sim}{v}\,n$$

$$\frac{\partial \underset{\sim}{v}}{\partial t} = q\underset{\sim}{E} - \underset{\sim}{v}\,\nu m$$

When each species is in a steady state

$$\partial \underset{\sim}{v}/\partial t = 0 \qquad \text{and} \qquad \underset{\sim}{J} = \frac{q^2 n}{\nu}\underset{\sim}{E}$$

Thus

$$\rho = \frac{\nu m}{q^2 n}$$

The ratio of the ion resistance to the electron resistance is $\frac{r_i}{r_e} = \frac{\rho_i}{\rho_e} = \frac{m_i}{m_e}\frac{\nu_e}{\nu_i} = \frac{m_i}{m_e}$. Thus the ion resistance, in a fully ionized steady state plasma is given by $r_i = \frac{m_i}{m_e} r_e$

If the plasma is not fully ionized, one expects that the ion resistance is more affected by neutral collisions than the electron resistance due to greater momentum transfer between masses of nearly equal size. If the collision frequency is large compared to the characteristic time of a large change in i_e one expects the steady state approximation to be a good one. Figure 6 shows the approximately best fit obtained using the above ion drift model for hydrogen ions. An electron temperature of 20ev is assumed. The current column cross section is 2 cm and the effective electron resistance is found to be 40 times the classical resistivity. The ion drift is enhanced by a factor of 10 to obtain this current form and the ion temperature is 1/25 of the electron temperature.

The last method used to calculate the conduction current uses the coupled circuit equations and a plasma resistivity given by $r = r_0 + r_1(t)$

The r_0 is just a constant classical resistance determined by the plasma dimensions and electron temperature. $r_1(t)$ is a non-linear phenomenological term with a definite time dependence related to the external fields or plasma current.

Different functional dependences of $r_1(t)$ are used. When $r_1(t)$ is proportional to $|B_z(t)|^2$ or $|B_z(t)|$ qualitative fits were found to occur between the calculated waveform and the forms observed experimentally. Figure 7 shows the experimentally observed current form and vacuum electric field for an argon discharge. Figure 8 shows a calculated wave form that resembles the measured one in shape. The parameters used for this fit are T_e = 1.0ev and plasma radius = 1.75cm. r_1 is proportional to $|B_z|^2$. Figure 9 shows a contracted time scale of figure 8 for several cycles. The over-all current form is similar to that observed experimentally. Figure 10 shows the experimentally observed current and electric field for a hydrogen discharge while figure 11 shows a calculated current form and electric field. A $|B_z|$ dependence is used for $r_1(t)$ and a radius of 2.5cm and an electron temperature of 10ev is used. With additional calculations it is felt a better fit will be obtained between computed and measured current for this current range.

Compared to the ion drift model, the non-linear resistance model gives a better qualitative fit of all the observed wave forms. However, the ion drift model produces wave form distortions in a physically clear way while the non-linear resistance model does not give clear

insight into the physical mechanism for the non-linear current form.

The results of the conduction current models can be summarized as follows. The current form calculations have shown that the plasma betatron conduction current can be approximated by a linear circuit model for high enough currents (about 2500 amperes in hydrogen). For lower currents the current form becomes too non-linear in form to be estimated by this model. A current made up of two streams, an ion stream and an electron stream, in which the ion resistance, $\mathcal{R}_i$, and the electron resistance, $\mathcal{R}_e$, are related by $\mathcal{R}_i = \frac{m_i}{m_e}\mathcal{R}_e$ is considered. The electrons are assumed to diffuse in an approximately ambipolar manner, in this way being eliminated from the electron current stream and reducing the overall current flow. The ion drift is calculated from guiding center drifts. This model gives some qualitative agreement with observed experimental results. Finally, a non-linear cicuit is used in which the plasma resistance is composed of a constant term, calculated from the plasma electron temperature and plasma column size plus a phenomenological term varying in time. When the phenomenological term is proportional to $|B_z|$ or $|B_z|^2$ qualitative agreement is found between all of the measured wave forms and those calculated.

CHAPTER VII

FIGURE CAPTIONS

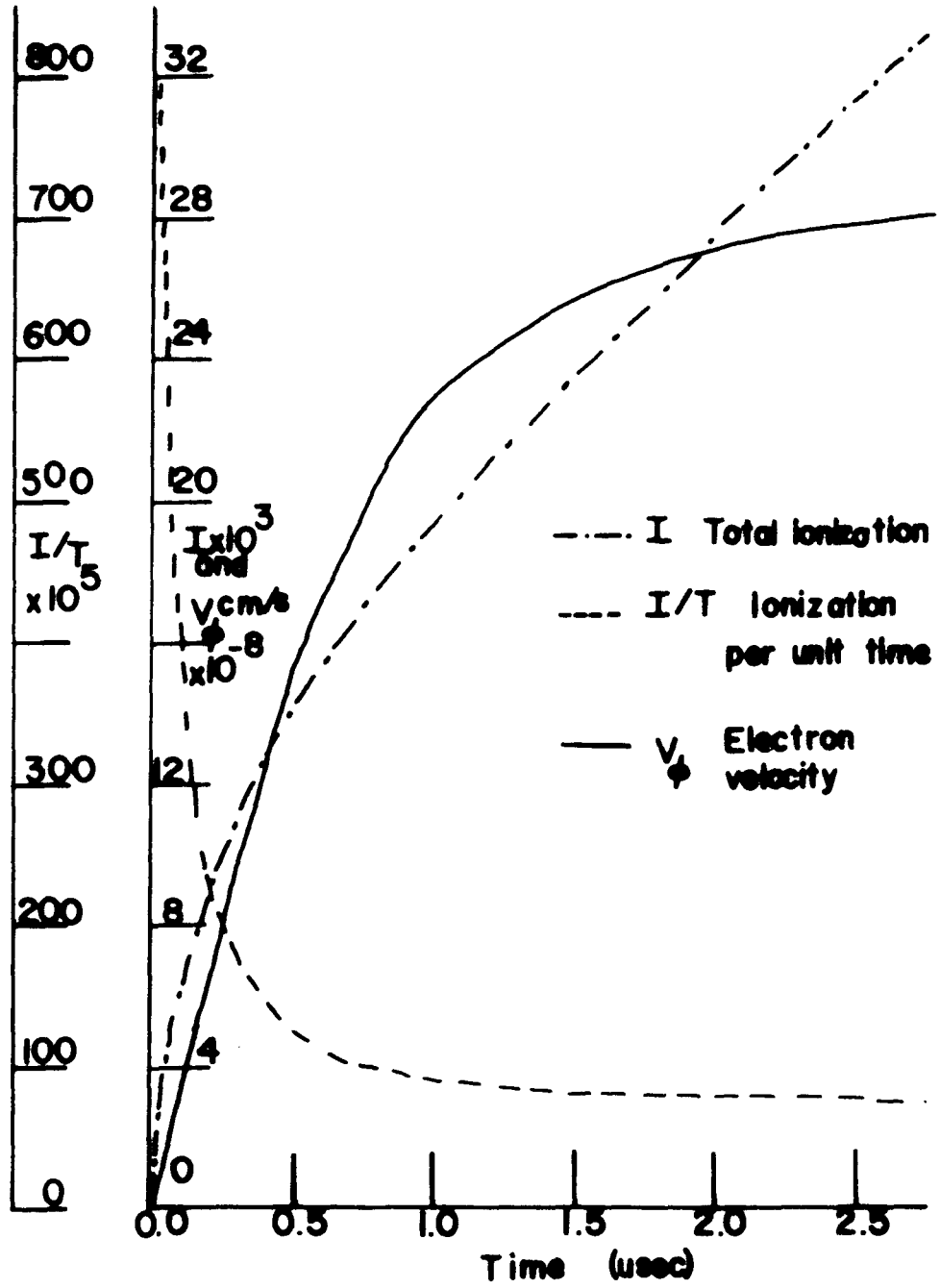
800
700
600
500
I/T
x10^5
300
200
100
0
32
28
24
20
I x10^3
and
V cm/s
φ
-8
1x10
12
8
4
0
0.0
0.5
1.0
1.5
2.0
2.5
Time (μsec)
I Total Ionization
I/T Ionization per unit time
V_φ Electron velocity

FIG. 1

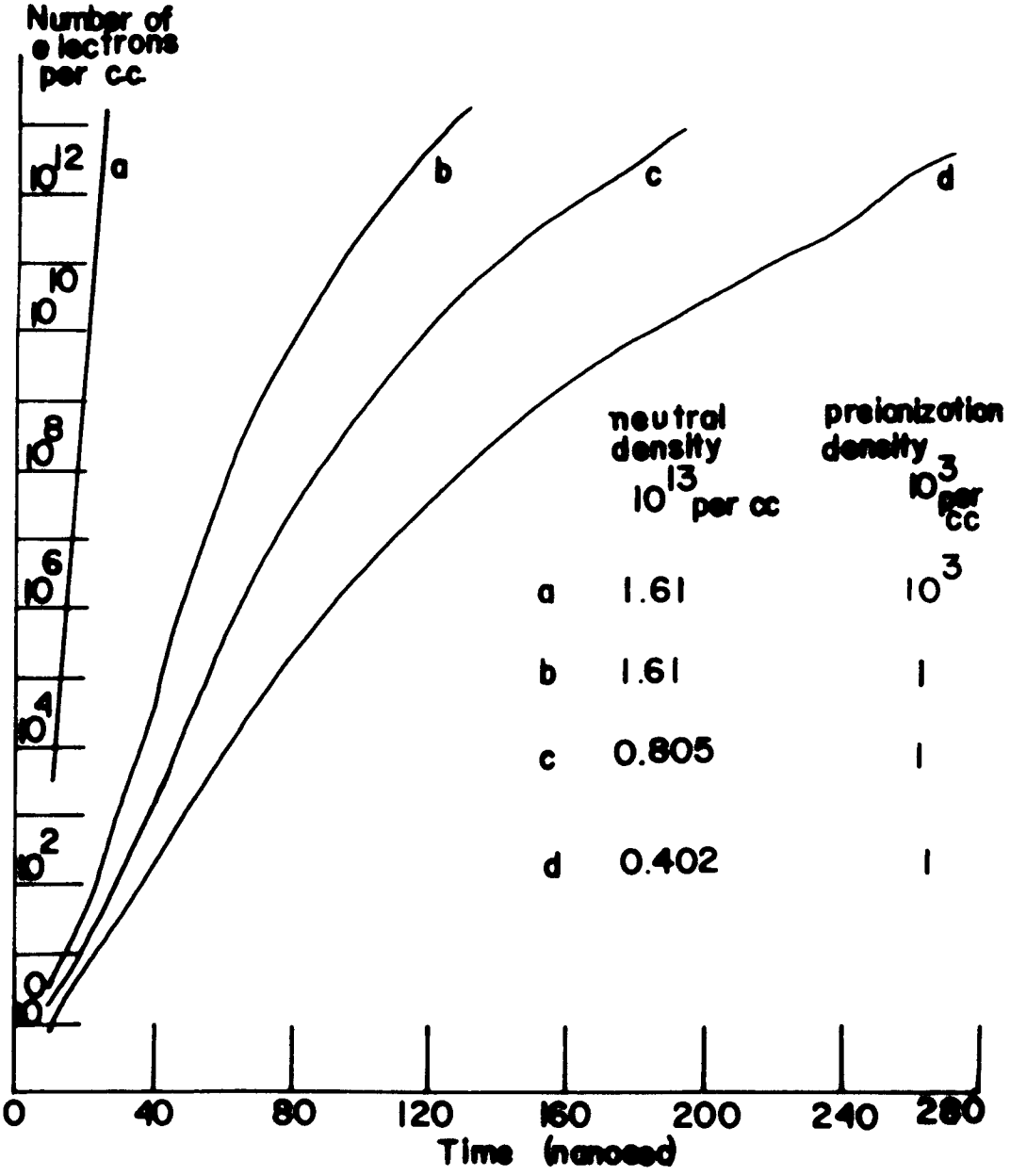
Number of electrons per c.c.
10^{12}
10^{10}
10^{8}
10^{6}
10^{4}
10^{2}
10^{0}
a
b
c
d
neutral density 10^{13} per cc
preionization density 10^{3} per cc
a 1.61 10^{3}
b 1.61 1
c 0.805 1
d 0.402 1
0
40
80
120
160
200
240
280
Time (nanosec)

FIG. 2

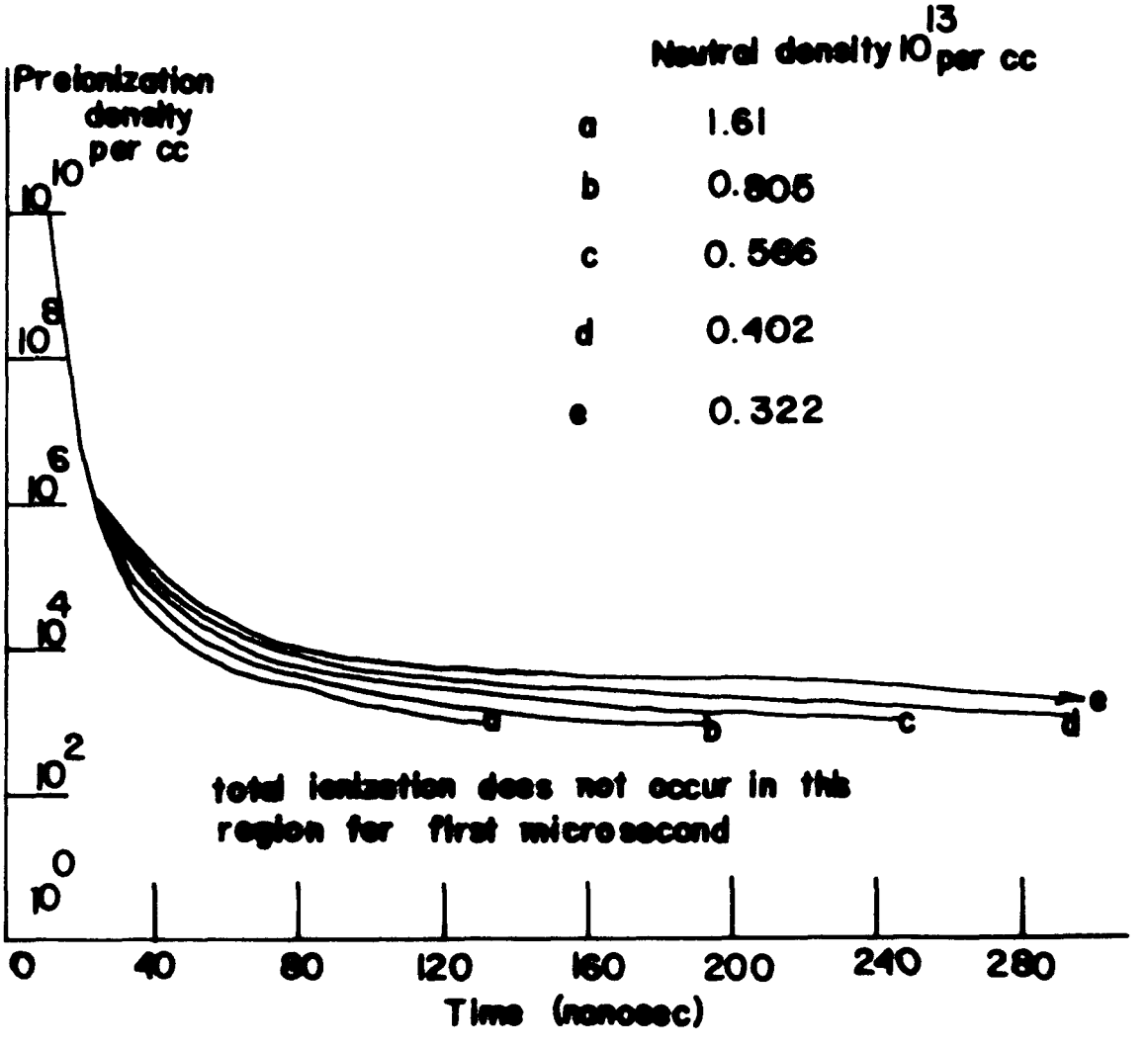
Neutral density 10^{13} per cc
a 1.61
b 0.805
c 0.586
d 0.402
e 0.322
Preionization density per cc
10^{10}
10^{8}
10^{6}
10^{4}
10^{2}
10^{0}
total ionization does not occur in this region for first microsecond
0 40 80 120 160 200 240 280
Time (nanosec)

FIG. 3

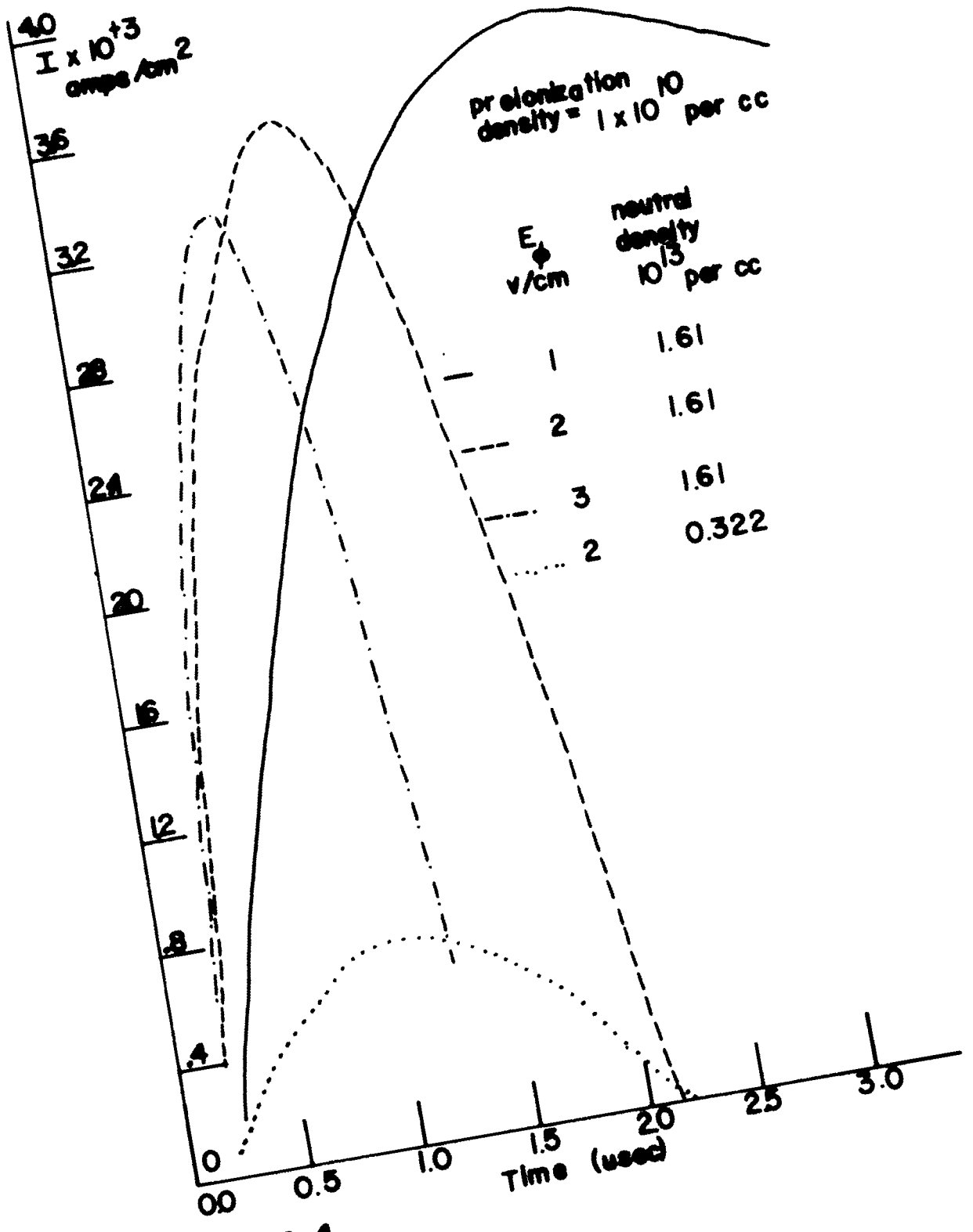
40
I x 10^+3 amps/cm^2
36
32
28
24
20
16
12
8
4
0
0.0
0.5
1.0
1.5
2.0
2.5
3.0
Time (usec)
preionization density = 1 x 10^10 per cc
E volts/cm
neutral density 10^13 per cc
1
1.61
2
1.61
3
1.61
2
0.322

FIG. 4

FIG.5

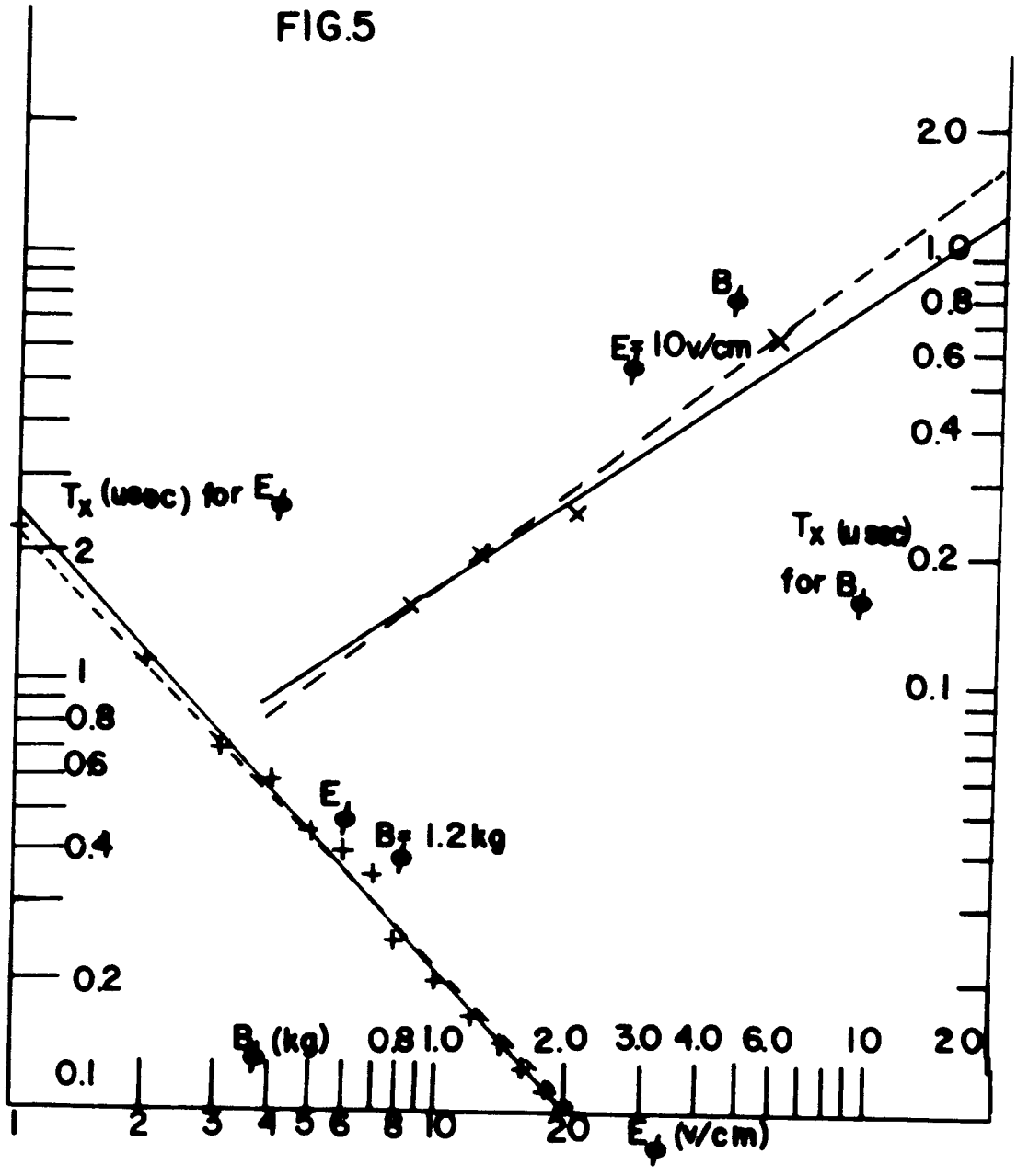
2.0
1.0
0.8
0.6
0.4
0.2
0.1
B_ϕ
E_ϕ= 10v/cm
T_x (usec) for E_ϕ
T_x (usec) for B_ϕ
2
1
0.8
0.6
0.4
0.2
0.1
E_ϕ
B_ϕ= 1.2kg
B_ϕ (kg) 0.8 1.0 2.0 3.0 4.0 6.0 10 20
1 2 3 4 5 6 8 10 20 E_ϕ (V/cm)

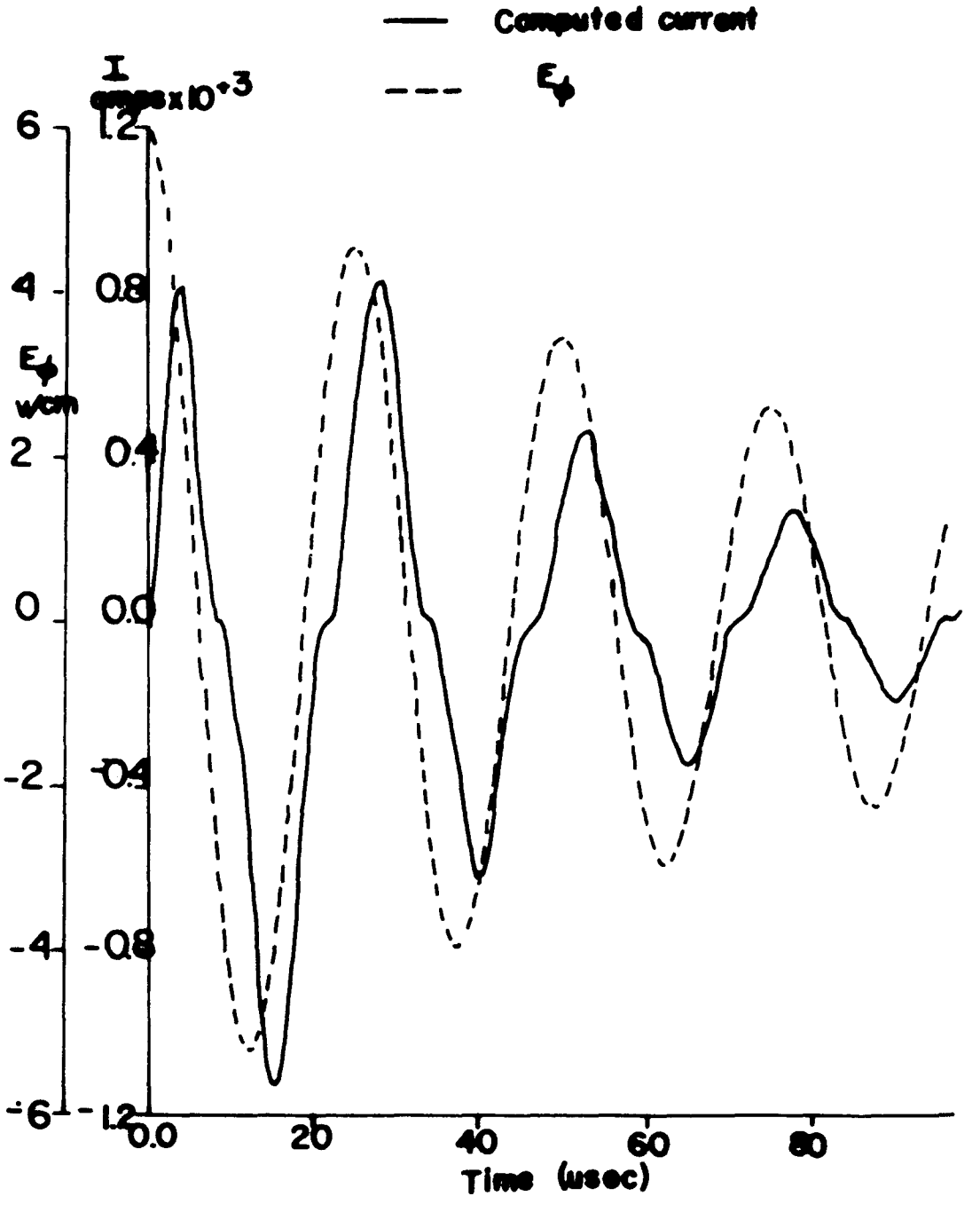
Computed current
E_ϕ
I amps x10^-3
E_ϕ v/cm
6
4
2
0
-2
-4
-6
1.2
0.8
0.4
0.0
-0.4
-0.8
-1.2
0.0
20
40
60
80
Time (μsec)

FIG.6

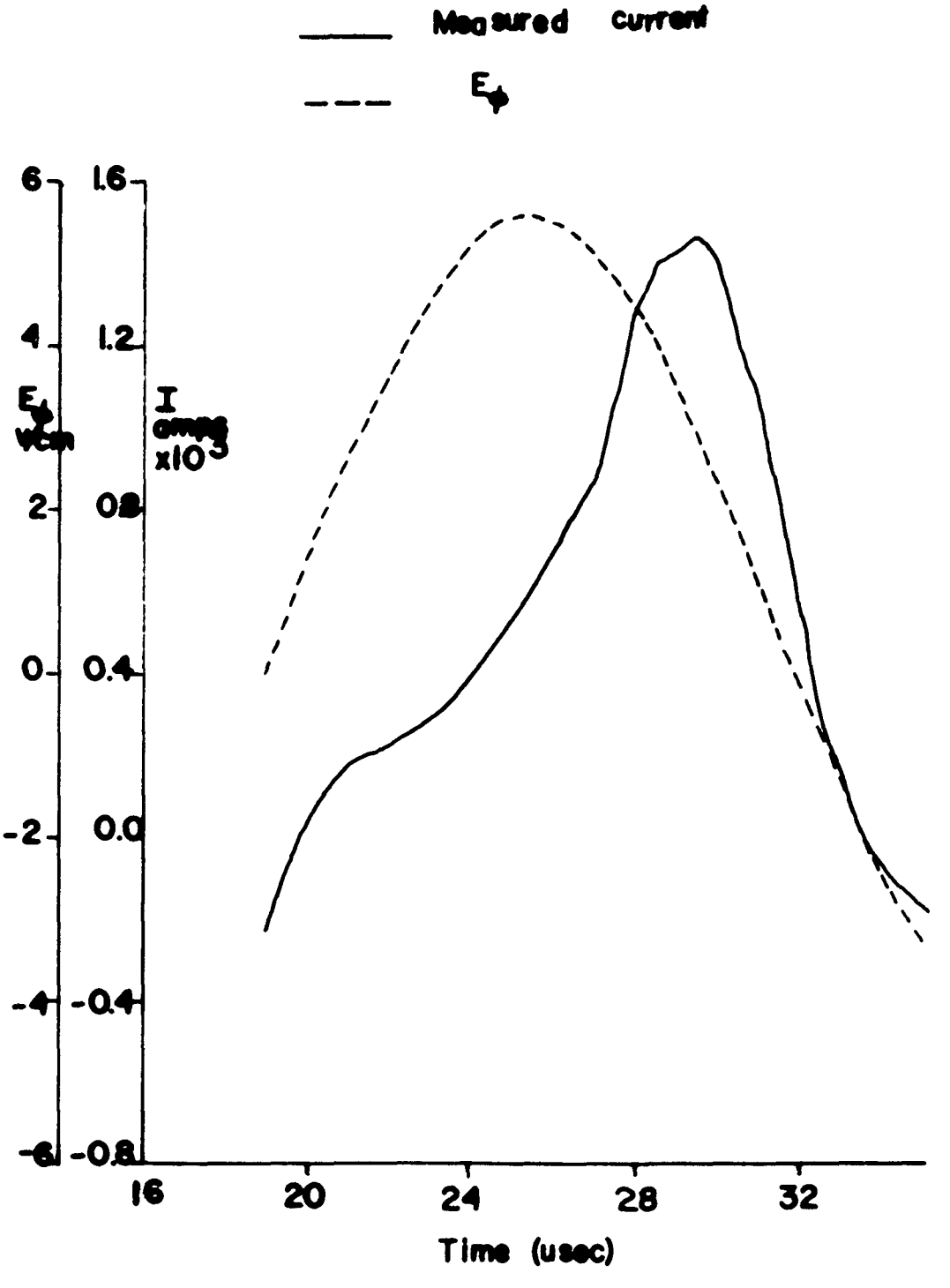
Measured current
E_ϕ
6
4
2
0
-2
-4
-6
1.6
1.2
0.8
0.4
0.0
-0.4
-0.8
E_ϕ volts
I amps x10^3
16
20
24
28
32
Time (usec)

FIG. 7

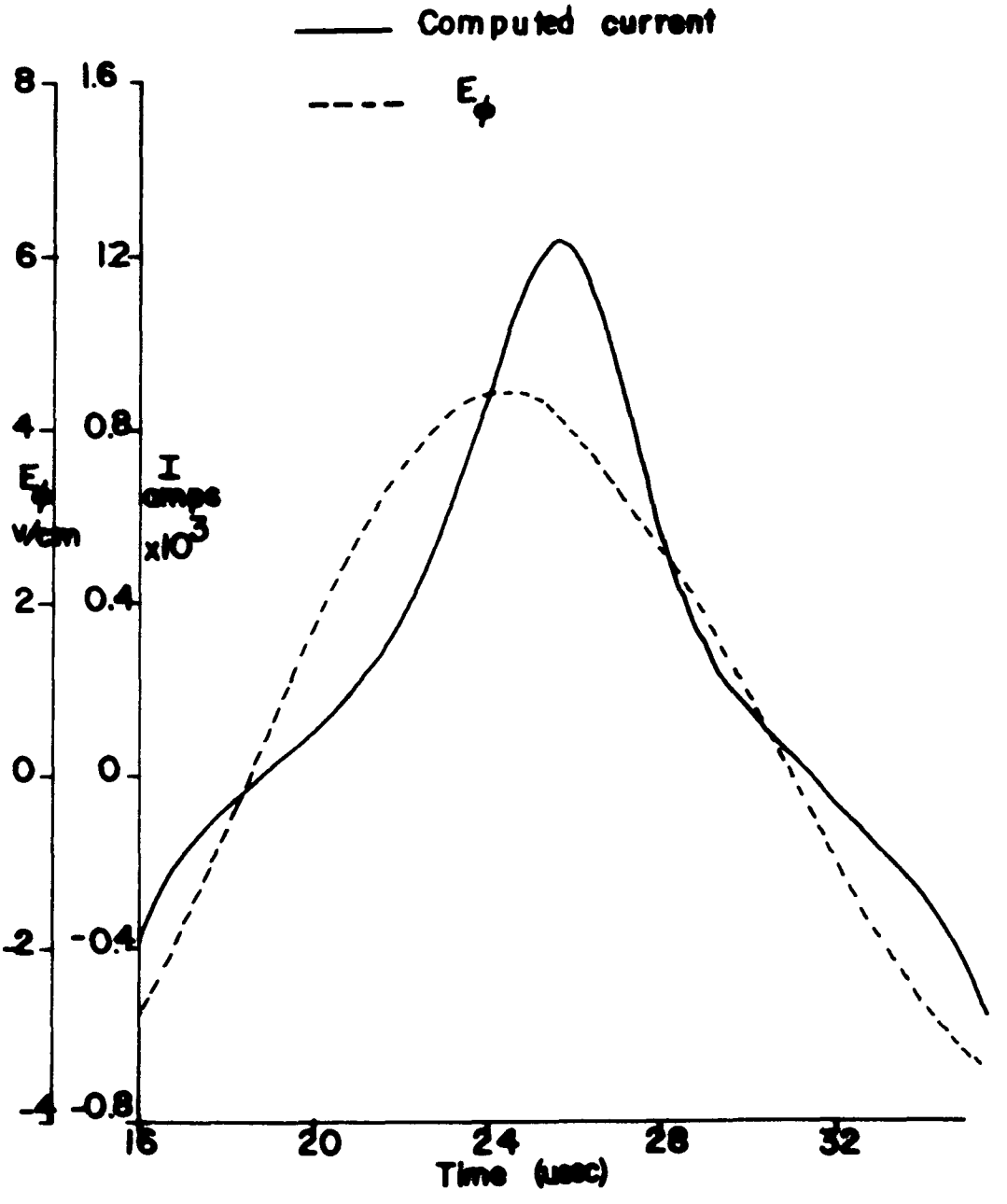
Computed current
E_ϕ
8
6
4
2
0
-2
-4
1.6
1.2
0.8
0.4
0
-0.4
-0.8
E_ϕ v/cm
I amps x10^3
16
20
24
28
32
Time (usec)

FIG. 8

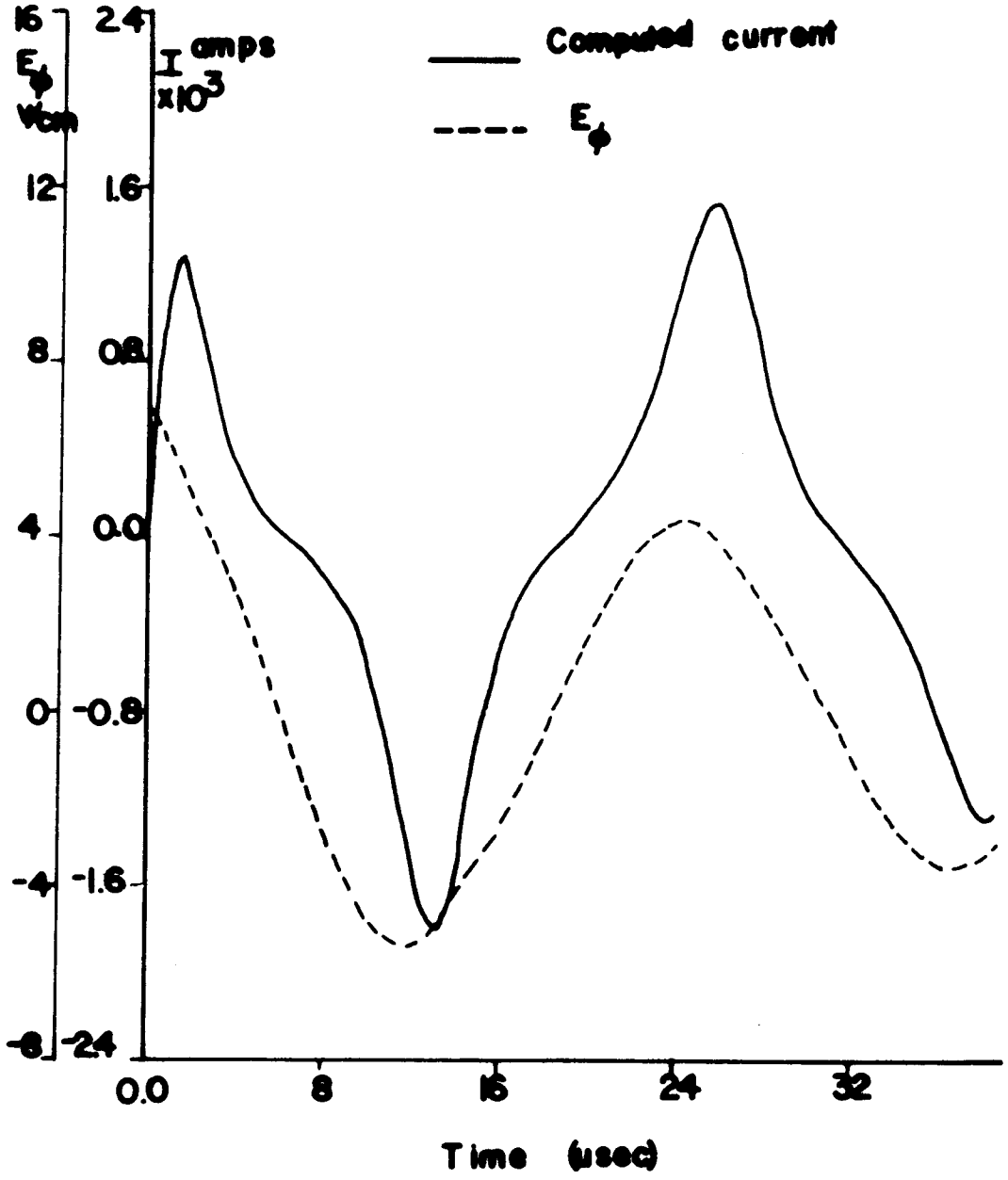
16
12
8
4
0
-4
-8
E_ϕ V/cm
2.4
1.6
0.8
0.0
-0.8
-1.6
-24
I amps x10^3
Computed current
E_ϕ
0.0
8
16
24
32
Time (μsec)

FIG. 9

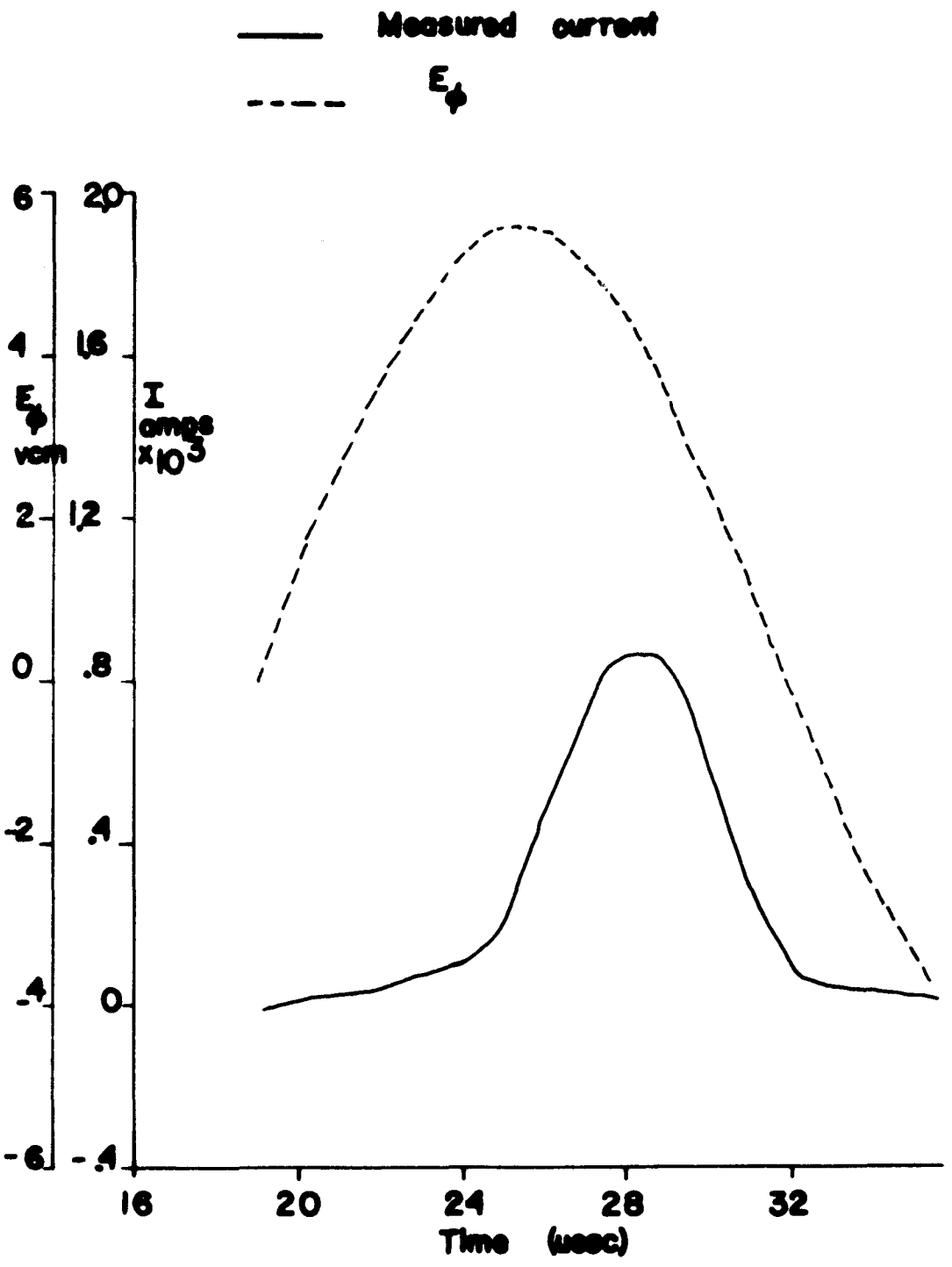
Measured current
E_ϕ
6
4
2
0
-2
-4
-6
20
16
12
8
4
0
-4
E_ϕ volts
I amps $\times 10^3$
16
20
24
28
32
Time (usec)

FIG. 10

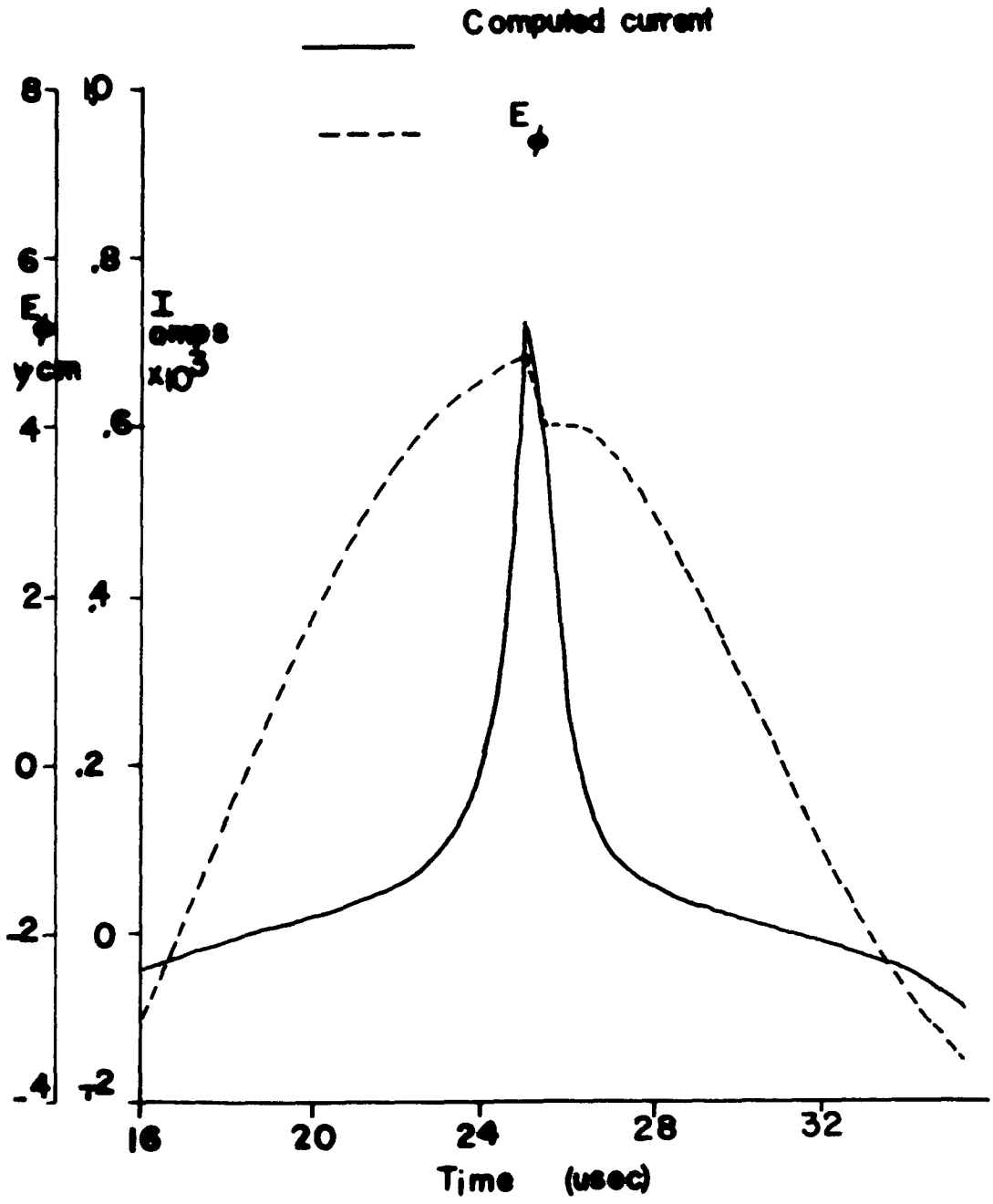
Computed current
E_ϕ
8
6
4
2
0
-2
-4
10
.8
.6
.4
.2
0
-2
E_ϕ v cm
I amps x10^3
16
20
24
28
32
Time (usec)

FIG. 11

CHAPTER VII

REFERENCES

1. J. T. Tate and P. T. Smith, Physical Review 39, 270 (1932).
2. P. T. Smith, Physical Review 36, 1293 (1930).
3. E. Gerjouy and G. W. Stuart, The Physics of Fluids 3, 1008 (1960).
4. H. Dreicer, Physical Review 115, 238 (1959).
5. N. A. Krall and A. W. Trivelpiece, Principles of Plasma Physics (McGraw-Hill Book Company, New York, 1973).
6. Ibid., chapter 6.

CHAPTER VIII

CALCULATIONS AND DISCUSSION

Using the digitized current form and electric field (chapter VI figures 2 and 3) the conductivity is calculated as a function of time. Because of the non-linear wave forms it is difficult to define the resistive component of the current. What is done here is to assume that the phase angle between the current amplitude $I(t)$ and the current maximum I_m is given by $\phi_I = \sin^{-1}\frac{I(t)}{I_m}$. The electric field phase angle is given by $\phi_E = \sin^{-1}\frac{E(t)}{E_m}$. The phase difference between E_ϕ and I is $\phi = \phi_I - \phi_E$. The resistive component of the current is then given by

$$I_R = I(t)\cos\phi$$

The real part of the conductivity is given by $\sigma_R = K\frac{I_m}{E_m}\cos\phi$, where K is one over the cross-sectional area of the current column. The observed changes in current column size (chapter VI) were not taken into account in the calculation of σ_R. Figure 1 shows the variation of σ_R with electric field in argon (chapter VI data set 1) as a function of time. Figure 2 compares the change in σ_R in argon for two different neutral pressures (data sets 1 and 2). Typical conductivity values are seen to be $10\text{x}10^{12}$ esu

near the current peaks. Figure 3 shows G_R plotted against time for data sets 3 and 4 which are two hydrogen discharges. As noted before, a much greater range in peak current values is found in hydrogen than in argon discharges. Figure 4 shows the argon conductivity extended to additional cycles. Trial 5 follows the trend of trials 3 and 4 and has a conductivity range of $4x10^{12}$ to $0.1x10^{12}$ esu. The apparant regular variation of conductivity with electric field strength over one cycle has not yet been explained in terms of a physical model, though the empirical computer model (chapter 7) does reproduce the basic current forms observed experimentally. The current column is assumed, in all these cases, to have a radius of 2.0cm.

The conductivity measured at the current maxima is considered in a series of measurements in both hydrogen and argon discharges. The initial current maximum is excluded due to high ionization rates during this time period. Four values of peak electric field are used(2.3, 4.6, 6.9, and 9.2 v/cm). The neutral pressure in argon is $5.4x10^{-4}$Torr while the hydrogen neutral pressure is about $6x10^{-3}$ Torr. The hydrogen discharges are similar to data set 4. The current column radius is estimated to be 2 cm. The conductivity is given by $G = \frac{I_m}{A E_m}$ where A is the

current cross-sectional area. The real part of the conductivity is reduced by $\cos\phi$ and this amounts to approximately a .7 reduction in the computed σ (3 usec shift between the peak of E_ϕ and the peak of I). It is found that in both the argon and hydrogen discharges the conductivity showed little variation with electric field. This is shown for argon in figure 5. The average value of σ obtained for this set of data (283 peaks) is

$$\sigma_A = 9.5 \pm 1.0 \times 10^{12} \text{ esu}$$

Similar results occur for hydrogen (56 peaks)

$$\sigma_H = 7.0 \pm 1.0 \times 10^{12} \text{ esu}$$

A third set of data was obtained to try to compare the plasma density in hydrogen and argon as the conductivity measurements are taken. Figure 6 shows the relative variation of the ion saturation current for different current peaks in both hydrogen and argon discharges. It is noted that $nT^{1/2}$ is very similar for both hydrogen and argon in the trial, which is typical of the trials considered. For 26 peaks the average value of σ in argon is

$$\sigma_A = 9.2 \pm 1.4 \times 10^{12} \text{ esu}$$

and for 23 peaks the average value of in hydrogen is

$$\sigma_H = 6.3 \pm 1.3 \times 10^{12} \text{ esu}$$

Tabulated below are the measured density, electron temp-

erature, peak electric field, and computed ion acoustic speed, C_s , and the the rate of the electron drift velocity to ion acoustic speed.

Gas	E_ϕ v/cm	$\bar{n}$ $\times 10^{12}$ cc^{-1}	$\bar{T}_e$ ev	σ $\times 10^{12}$ esu	c_s $\times 10^{6}$ cm/s	v_D/c_s
argon	2.3	2.8	29	9.1	1.4	36
argon	4.6	3.4	32	9.8	1.5	68
argon	6.9	5.9	27	9.9	1.4	62
argon	9.2	7.9	24	9.2	1.3	56
hydrogen	4.6			5.9		
hydrogen	6.9			6.6		
hydrogen	9.2	7.3	14	8.3	6.4	9.4

The classical conductivity corresponding to 14ev is $6.9\text{x}10^{14}$esu. The corresponding classical conductivity temperature for a conductivity of $8.3\text{x}10^{12}$esu is 0.73ev. When the phase difference between E_ϕ and I is taken into account $\sigma_{R_N} = 6\text{x}10^{12}$esu and the corresponding electron temperature is predicted to be 0.6ev. Using the conductivity value of $1\text{x}10^{13}$esu obtained in the calculation of $\sigma(t)$ one finds that the classical resistivity temperature is 0.8ev. It is thus seen that the measured conductivity is anomalously low.

As discussed in chapter II various theories have been formulated to account for anomalously low conductivity. Assuming a density of $8\times10^{12}cc^{-1}$ the following conductivity values (esu) are found for the theories mentioned for hydrogen and argon plasmas:

theory	2-stream Buneman	2-stream Sizenenko	ion-acous. Sagdeev	ion-acous. Sizenenko	ion-acous. Dupree $k\lambda_D=1$
gas					
argon	3.3×10^{12}	6.9×10^{12}	$4\times10^{12}\cdot T_i/T_e$	4.1×10^{14}	1.6×10^{12}
hydrogen	9.8×10^{11}	1.1×10^{12}	$4\times10^{12}\cdot T_i/T_e$	1.2×10^{13}	1.6×10^{12}

For the Sagdeev fomulation it is assumed that $V_D = 5\times10^5$ m/s, $T_e = 15ev$, $n = 8\times10^{12}cc^{-1}$, $V_e = 1.6\times10^6$m/s. For the Dupree conductivity it is assumed that the fastest growth rate is for ion acoustic wave numbers having $k = \frac{1}{\lambda_D}$.

Hirose and Alexeff[6] have found resistivities higher than the Buneman resistivity in the case of a radial gradient in the drift velocity. This value is higher than what is measured in this experiment and a drift velocity gradient is not observable with the measurements made. Other formulations of conductivity involve analysis of power spectrum and were omitted since relevant data has not yet

been obtained.

These theoretical results do not show good numerical agreement with the measured values of conductivity. The values obtained by the Sagdeev formula are too low since T_i/T_e cannot be expected to be much greater than 0.1. Both two-stream formulations show too strong an ion mass dependence as well as having numerical values which are two low. The ion acoustic formulation by Sizenenko and Stepanov is too high and shows too strong a mass dependence. The Dupree formulation gives values which are too low assuming the maximum growth rate of ion acoustic waves occur for k^{-1} = one Debye length.

The Dupree formulation may be best suited for the description of the conductivity measurements for the following reasons:

1. Lack of ion mass dependence.
2. Possibility of electron trapping.[1,2] The measured values of n_e and T_e are such that the observed discharges occur in a regime in which electrons can be trapped in the periodic fields of the ion-acoustic waves, $(n_e J_0^3)^{1/4} > \left(\frac{n_e}{n_i}\right)^{1/2}$. This results in the greater slowing of growth of short wavelength waves rather than long wavelength waves thus decreasing the value

of k that should be used in the Dupree formulation. This increases the predicted value of Γ .

3. T_e/T_i and v_D/c_s may be of such values that the linear stability theory of ion acoustic waves predicts faster growth rates for $k\lambda_D < 1$ than for $k\lambda_D > 1$ thus increasing the predicted value of Γ .

It will now be shown that for reasonable values of T_e/T_i and observed values of v_D/c_s the linear theory of stability of ion acoustic waves predicts the maximum growth of ion acoustic waves with wavenumbers k such that the Dupree formulation fits the experimental results for the average conductivity. It is assumed that for argon $c_s = 6.2\text{x}10^5$ cm/sec and $c_s = 6.4\text{x}10^6$ cm/sec for hydrogen. With these values of c_s it is found that the linear analytic solution is valid for $0.1 \lesssim k\lambda_{De} \lesssim 2$ provided that $T_e/T_i \gtrsim 10$ and for hydrogen $v_D/c_s \lesssim 40$ while for argon $v_D/c_s \lesssim 300$. As noted before these are just the range of values of v_D/c_s observed experimentally.

Figure 7 shows ω_r as a function of wave number. Figure 8 shows the values of v_D/c_s for maximum growth rates as a function of k for no Landau damping ($T_e/T_i \gtrsim 100$). The value of ω_i is included next to some of the points plotted. It is found that for k^{-1} less than one Debye length the maximum ω_i is negative

indicating a damping of waves at these wave numbers. In order to have smaller wavenumbers which represent growing waves one must consider cases in which Landau damping is not negligible. Figure 9 is a plot of ω_i versus k for different values of T_e/T_i. One sees a maximum for ω_i occuring at $k^{-1} \lesssim \lambda_D$ (λ_D = one Debye length and $\lambda_{De} = \sqrt{2}/2 \cdot \lambda_D$). When $T_e/T_i \cong 11$ for hydrogen and argon the values of σ computed from Dupree's formula agree with the experimental values discussed above for equal argon and hydrogen densities. The values of k^{-1}, ω_i, ω_R, f_R (wave frequency in Hz), and T_i (wave growth period) for hydrogen and argon are shown below

	k^{-1} (λ_D)	ω_i (sec^{-1})	ω_R (sec^{-1})	f_R (MHz)	T_i (usec)
argon	0.17	2.2×10^5	5.5×10^7	0.88	28
hydrogen	0.2	2.5×10^7	3.2×10^9	510	0.25

It is noted that the argon growth rate of 28 usec is too high for agreement with experimental conditions. Also the possibility of neutral collisions enhancing the resistivity,[3] particulary in hydrogen, makes the interpretation of these calculations less clear. Because of the possibility of electron trapping, however, the maxima of the ω_i curves for higher values of T_e/T_i may be

shifted to lower values of $k\lambda_{De}$. The obvious dependence of conductivity, in hydrogen discharges, on plasma density may be explained by assuming that the values of v_0/c_s and T_e/T_i adjust to give the proper k values. This is an experimentally verifiable point. It is also noted that at lower conductivity values k should increase, according to the Dupree theory, and the corresponding ω_i increases, too. This implies that the lower current discharges in hydrogen would have a fast enough growth rate for ion-acoustic waves of the proper wave number. Again, the increasing number of neutrals tends to mask changes in σ_R .

One notes several important tests of the Dupree theory. A measurement of the plasma wave spectrum[4] to detect the presence of ion acoustic waves and their dominate frequency, a measurement of T_e/T_i , and measuring n and the current distribution are important parameters to determine the validity of the Dupree theory for this experiment.

Figure 10 shows the variation of the equilibrium orbit position with time for the argon data, trial 2, discussed in chapter VII. This is calculated using the resistive current instability formulation discussed in chapter II. A field index of 0.5 and of 0.25 in the stable orbit region is assumed. For the cycles shown it is seen that the equilib-

rium orbit lies within the vacuum chamber (shift $\leq$ 0.025m) for only a small period of time and when this occurs the acceleration cycle is not in the proper phase in order for betatron acceleration to occur. As was mentioned in chapter VI the lack of energetic runaway electrons in cycles other than the initial cycle is consistant with the resistive current instability. The observation of X-rays in hydrogen during cycles other than the first can be used to further test this hypothesis by carefully measuring the threshold current at which beam disruption occurs and how this threshold varies with changes in the external fields. The measured dependence of X-ray disruption time on $\mathcal{E}_\phi$ and B_ϕ during the first cycle can not be definitely attributed to single particle effects (resistive current instability) or to collective effects. A collective effect which is possibly occuring is a two-stream instability in which the density builds up to such an extent that the growth rate, which is proportional to the plasma frequency, becomes comparable to the acceleration time. Rapid density build-up is observed in all the cycles in which X-rays are produced. This is also consistent with the calculations in chapter VII dealing with ionization by runaway electrons. Again, it is necessary to observe the plasma wave spectrum to see whether electron plasma waves of the appropriate

frequencies are being generated at the disruption time. To prove that a collective effect is causing the beam disruption, it is also necessary to explain the E_ϕ dependence of the disruption time though this may be related to the ionization rate being a function of E_ϕ .

The non-linear current form may be related to particle trapping effects. In Tokamak devices a type of particle trapping occurs along the toroidal field lines due to the rotational transform and the B_ϕ gradient. In this experiment these, so called, banana orbits are unlikely to be significant in producing the non-linear wave form since the current distortion is greatest when the current is the smallest. Thus the banana trajectories become too long to have a significant trapping effect. The regular corrugation of B_ϕ , however, may be large enough to produce trapping effects. Again one can consider single particle phenomena in which a beam of electrons with drift velocity $V_D(t)$ is passing through the corrugated field. If one assumes that the ion-electron collision frequency stays constant, then by reducing the number of charge carriers through trapping, the effective drift velocity is reduced. Alternatively, or in addition to, the trapped particles may interact with the free streaming particles

producing a two-stream instability which enhances the plasma resistivity. An effect like this may be applicable to the low conductivity values observed at the current peaks. This effect has recently been reported in the literature[5] though the results are inconclusive.

The measured current column size is consistent with other measurements taken. Additional measurements should be performed to try to better understand the apparant motion of the current column. According to the calculations of the ion drift, the motion of the center of the current column appears to be at least 10 times too fast to be accounted for by ion drift in the external fields. In addition, since the equilibrium orbit is far from the vacuum chamber for most of the discharge the apparant back and forth motion of the current column cannot be explained by the presence of restoring forces. These arguments suggest that the observed oscillations in the current probe signals (chaper VI figure 18) are due to a kink structure in the plasma column. This may also explain, in part, the observed oscillations of the ion saturation current. The correlation between the kink structure (or column motion) and the conductivity and X-ray emission is an interesting relationship to investigate. From the

measured B_θ profile as a function of time (figure 17 chapter VI) the q values, $\frac{r}{R}\frac{B_\phi}{B_\theta}$, can be calculated as a function of time. For $q<1$ the plasma is unstable to the kink instability. The table below shows computed values of q for the two probe positions r_1 =.89cm and r_2 = 1.52cm. These positions are measured with respect to the center of the toroidal vacuum chamber. The values of r used are calculated from the position of the current column center, r_o, as calculated in chapter VI. Similarly the values of R used are the major radius of the current column.

t μsec	R_o cm	r_o cm	r_1 cm	r_2 cm	R cm	B_{θ_1} gauss	B_{θ_2} gauss	q_1	q_2
0.5	0.66	0.86	0.03	0.66	19.86	2.2	47	.75	0.77
1.0	0.75	0.80	0.09	0.72	19.65	11	79	.46	0.51
1.5	0.94	0.65	0.24	0.87	19.63	27.8	101	.48	.48
2.0	1.02	.63	.26	.89	19.55	36.6	123	.40	.40
2.5	1.10	.55	.44	.97	19.49	47.1	136	.52	.40
3.0	1.11	.49	.50	1.03	19.49	55.9	147	.46	.39
3.5	1.15	.51	.48	1.01	19.51	50.5	136	.53	.41
4.0	1.20	.61	.28	.91	19.61	39.8	99	.39	.51
4.5	1.33	.52	.37	1.00	19.52	25.1	62	.84	.91
5.0	2.01	.17	.72	1.35	19.17	15.6	39	2.7	2.0

Here t is the time measured with respect to the current zero. It is seen that the q values are less than 1, except at 5.0 usec, and the plasma column is kink unstable. It is noted that these calculations are based on the assumption of a uniform current distribution.

CHAPTER VIII

FIGURE CAPTIONS

Figure	Page	Caption
1-4	189-192	Conductivity as a Function of Time Using Single Discharges
5	193	Conductivity for Argon Peak Current Values Averaged Over Many Discharges
6	194	Density as a Function of Time Using a Langmuir Probe
7	195	Ion Acoustic Frequency Versus Wavenumber
8	196	Electron Drift Velocity Versus Wavenumber for Maximum Growth Rate of Ion Acoustic Waves
9	197	Ion Acoustic Wave Growth Rate as a Function of Wave Number
10	198	Typical Variation of Single Particle Equilibrium Orbit Position as a Function of Time

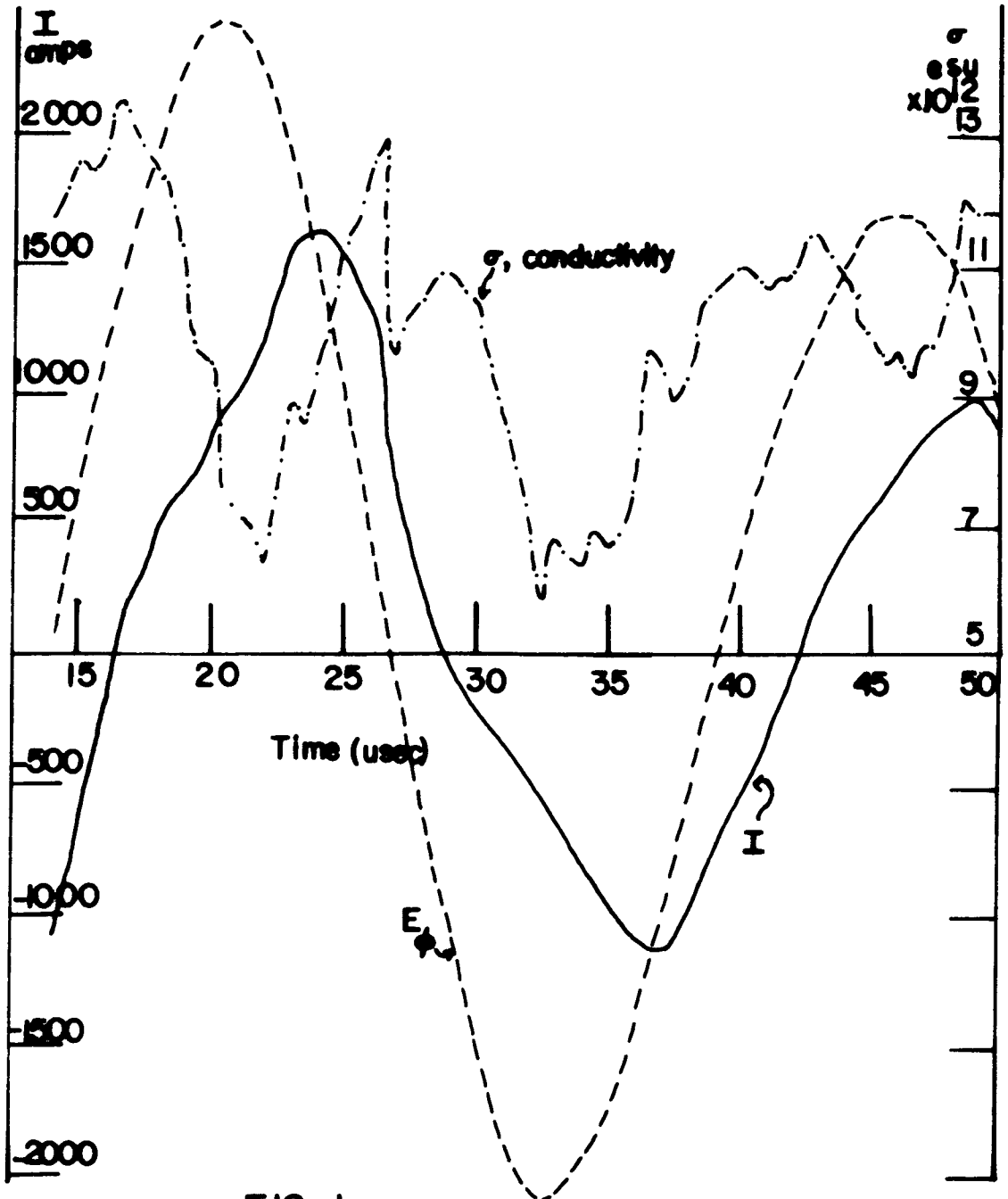
I
amps
2000
1500
1000
500
-500
-1000
-1500
-2000
σ
esu
x10^12
13
11
9
7
5
σ, conductivity
15
20
25
30
35
40
45
50
Time (usec)
E
I?

FIG. 1

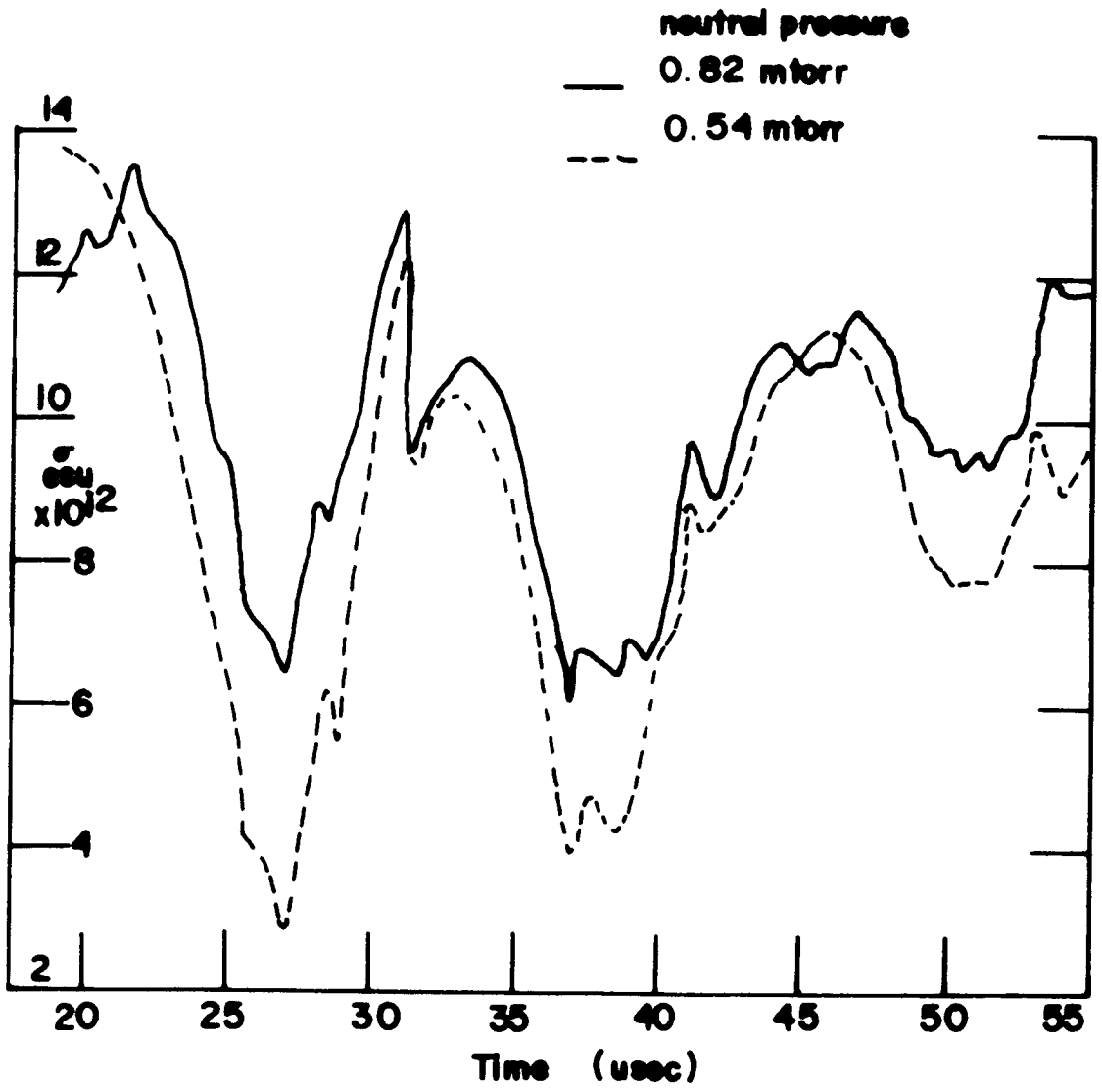
neutral pressure
0.82 mtorr
0.54 mtorr
14
12
10
8
6
4
2
σ eeu x10^12
20
25
30
35
40
45
50
55
Time (usec)

FIG. 2

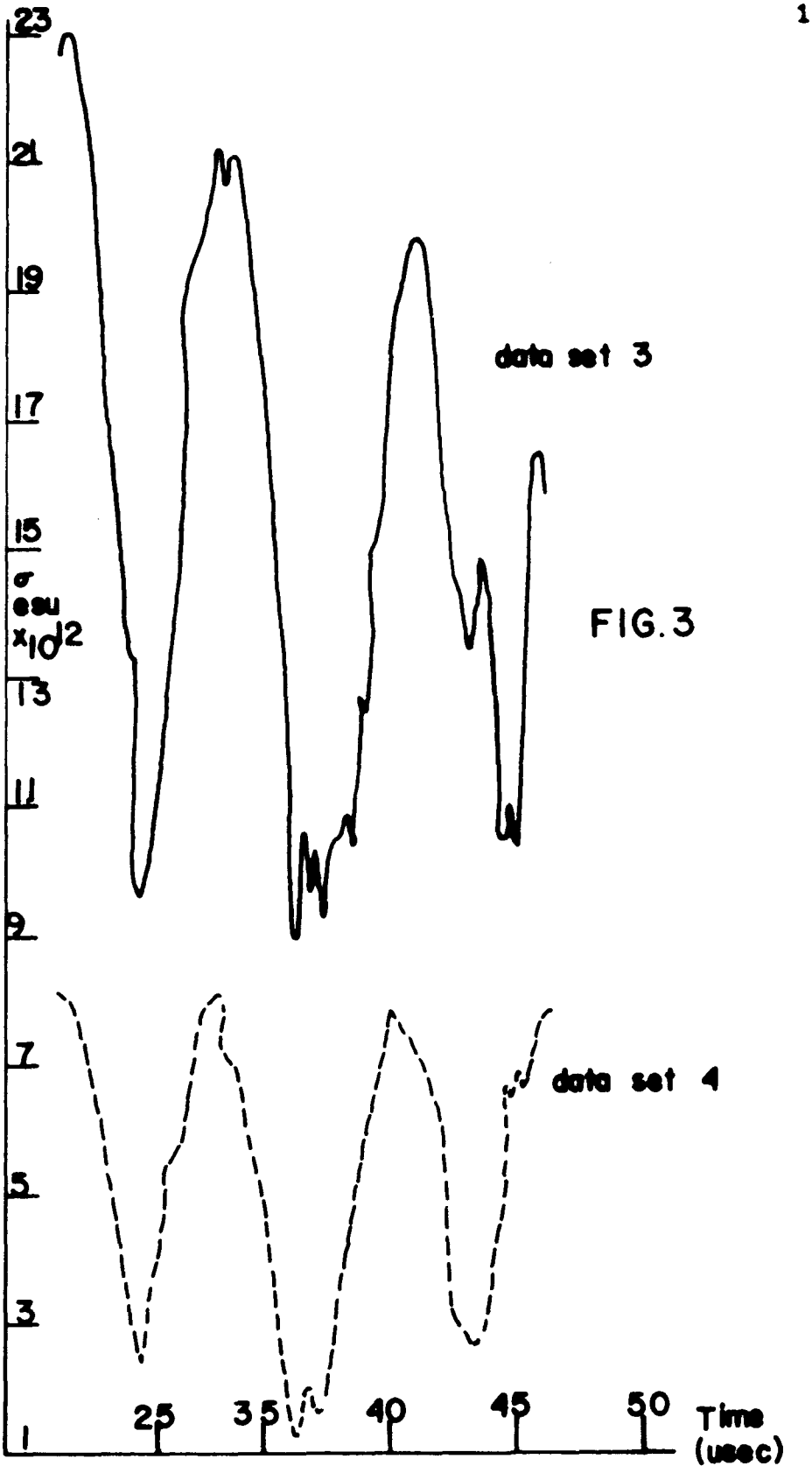
23
21
19
17
15
σ esu x10^12
13
11
9
7
5
3
1
25
35
40
45
50
Time (usec)
data set 3
data set 4

FIG. 3

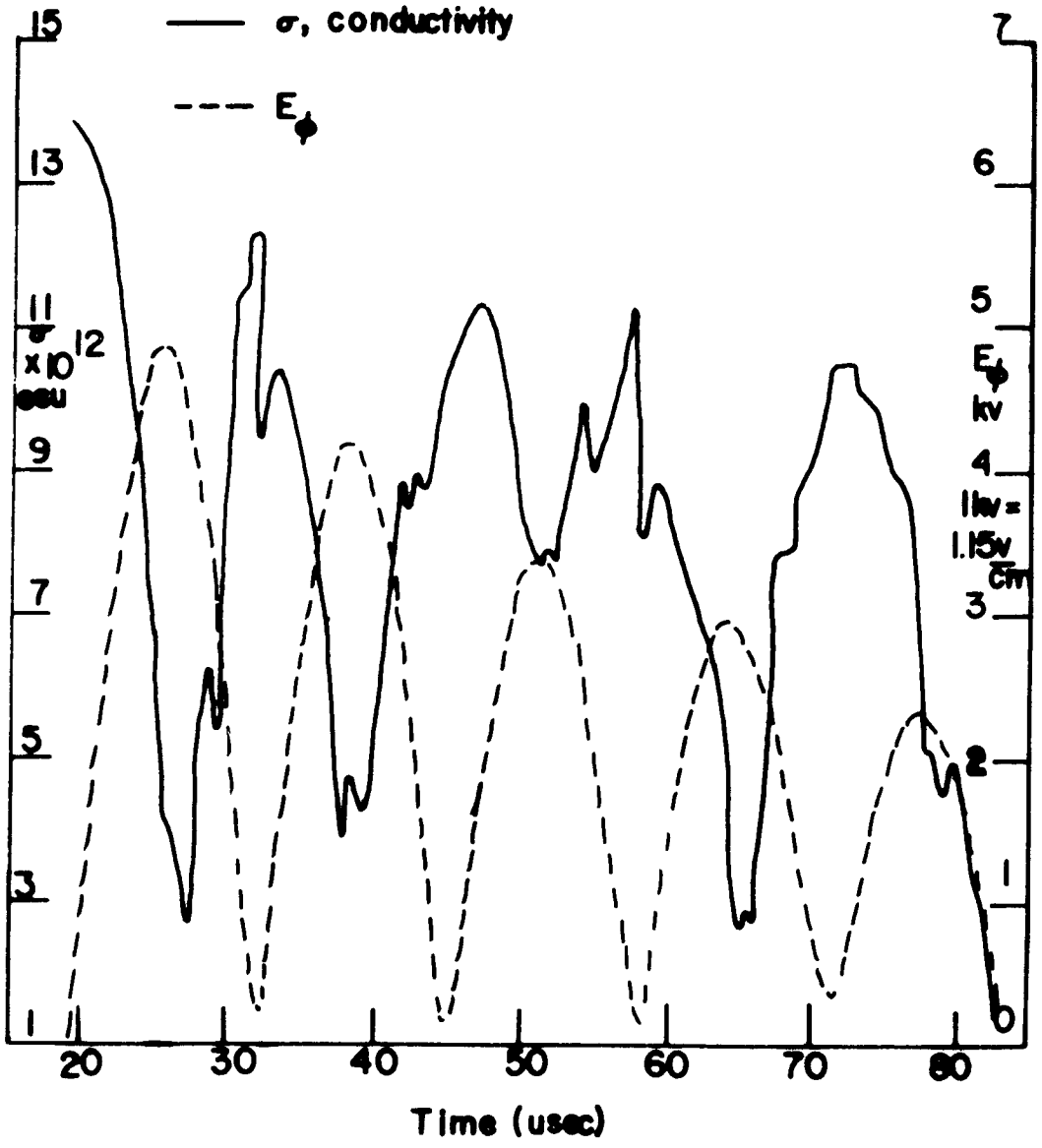
σ, conductivity
E_ϕ
15
13
11
9
7
5
3
1
σ x10^{12} emu
7
6
5
4
3
2
1
0
E_ϕ kv
1kv = 1.15v/cm
20
30
40
50
60
70
80
Time (usec)

FIG. 4

FIG. 5

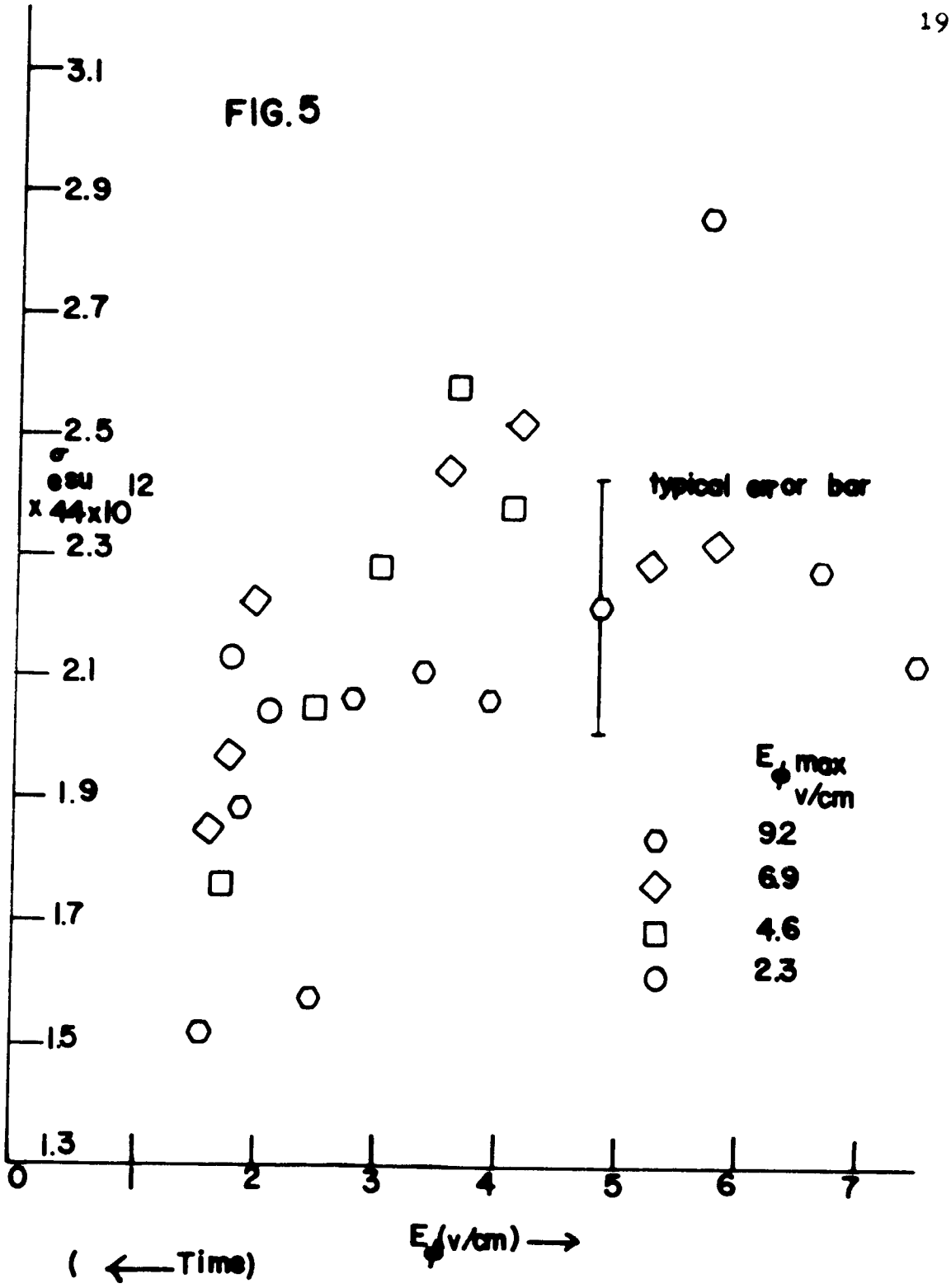
3.1
2.9
2.7
2.5
σ esu x 44x10^12
2.3
2.1
1.9
1.7
1.5
1.3
typical error bar
E_φ max v/cm
92
6.9
4.6
2.3
0
2
3
4
5
6
7
E_φ (v/cm) →
(← Time)

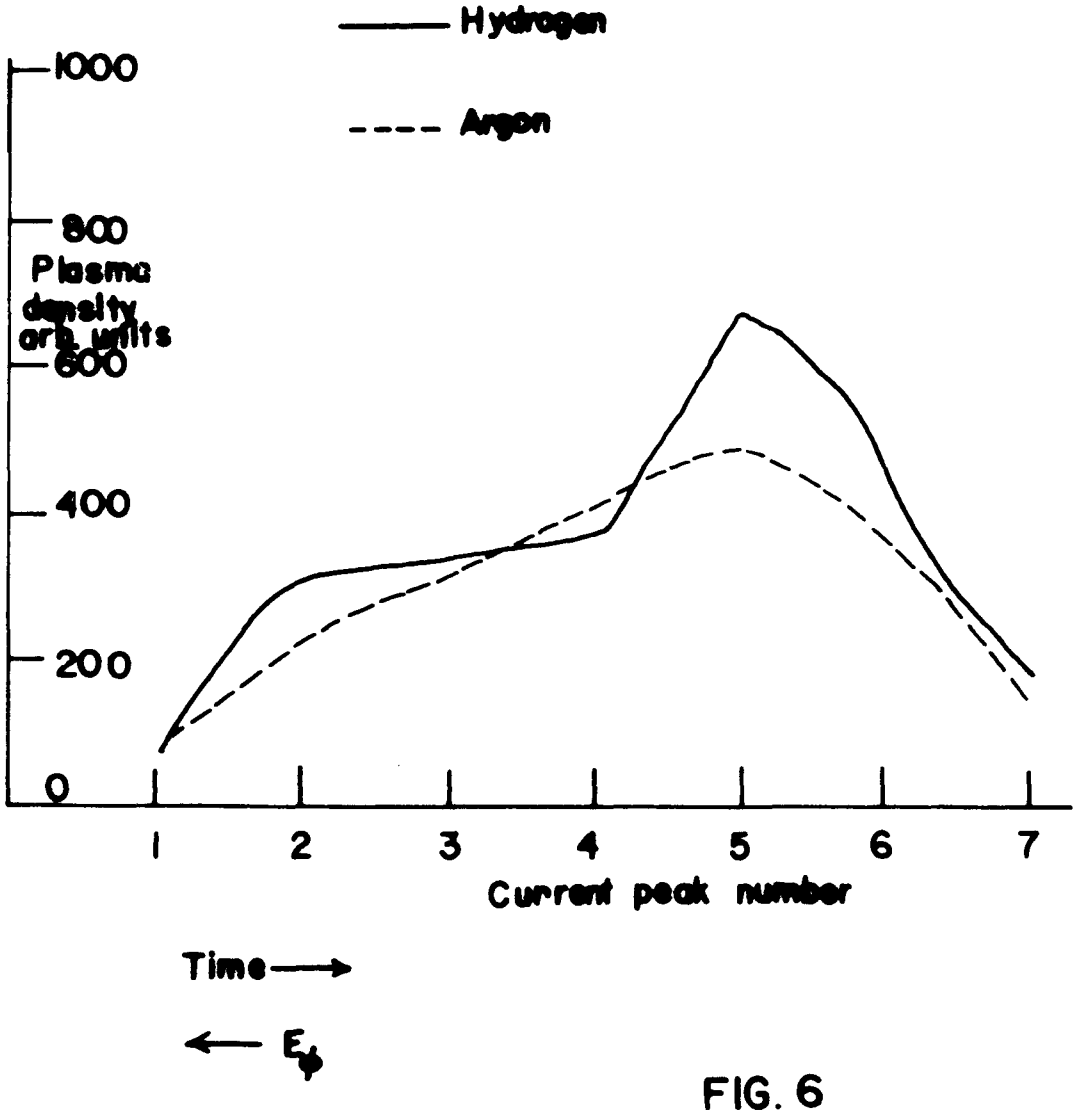
Hydrogen
Argon
1000
800
Plasma density arb. units
600
400
200
0
1
2
3
4
5
6
7
Current peak number
Time
E_ϕ

FIG. 6

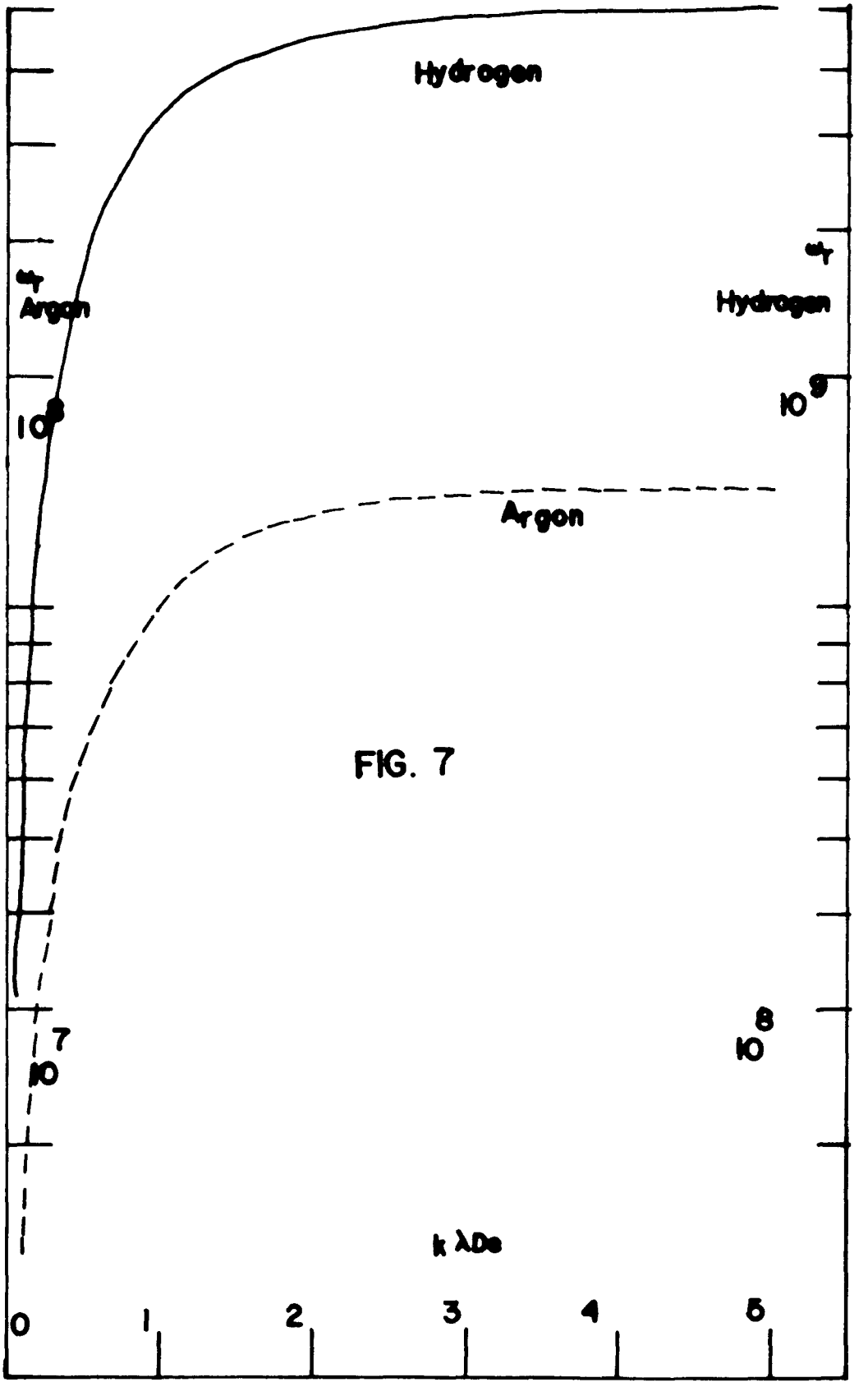
Hydrogen
ω_r
Argon
10^8
ω_r
Hydrogen
10^9
Argon
10^7
10^8
$k\lambda_{De}$
0
1
2
3
4
5

FIG. 7

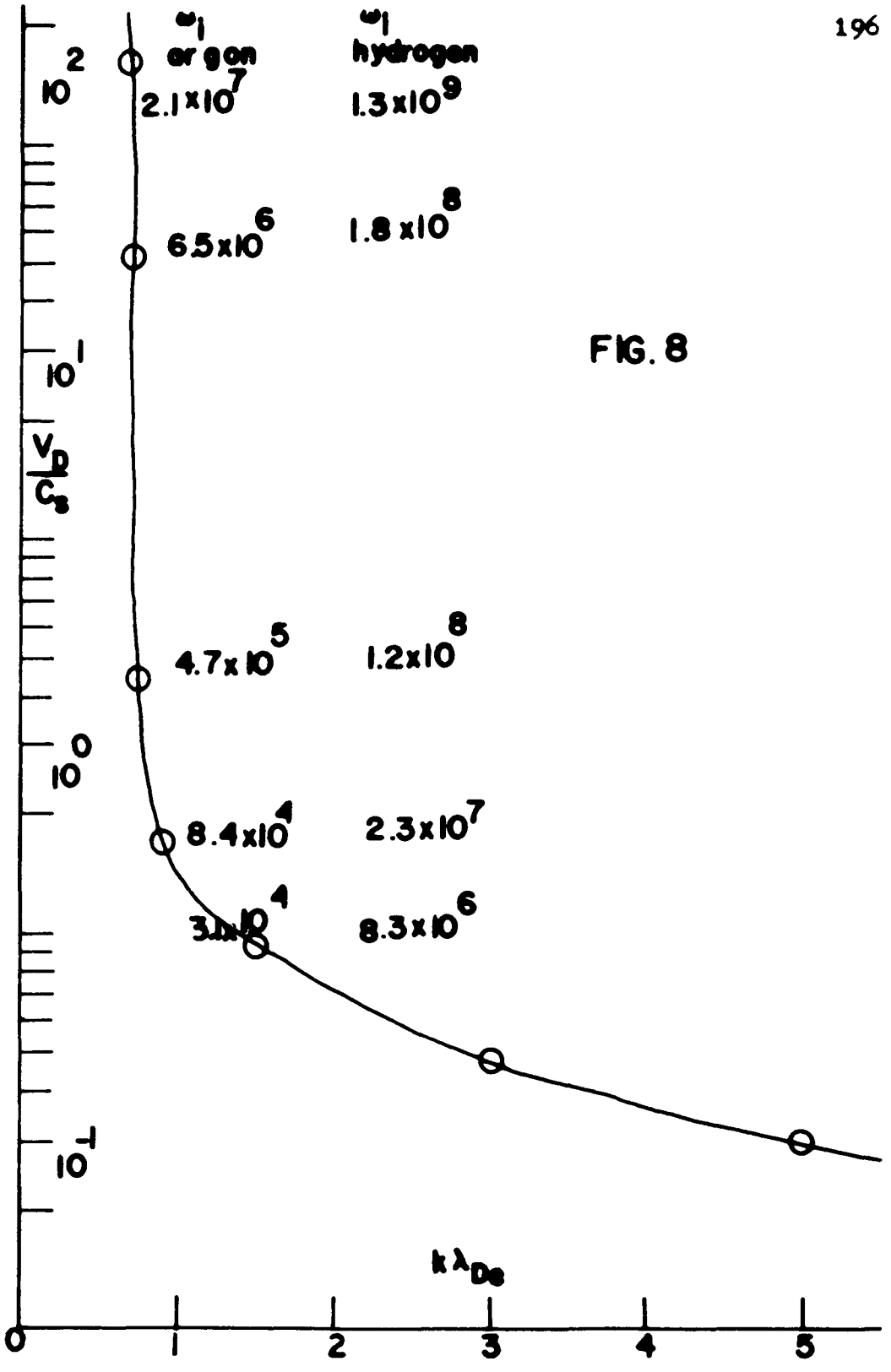
ω_i argon
ω_i hydrogen
10^2
2.1×10^7
1.3×10^9
6.5×10^6
1.8×10^8
10^1
$\frac{V_D}{C_s}$
4.7×10^5
1.2×10^8
10^0
8.4×10^4
2.3×10^7
3.0×10^4
8.3×10^6
10^{-1}
$k\lambda_{De}$
0
1
2
3
4
5

FIG. 8

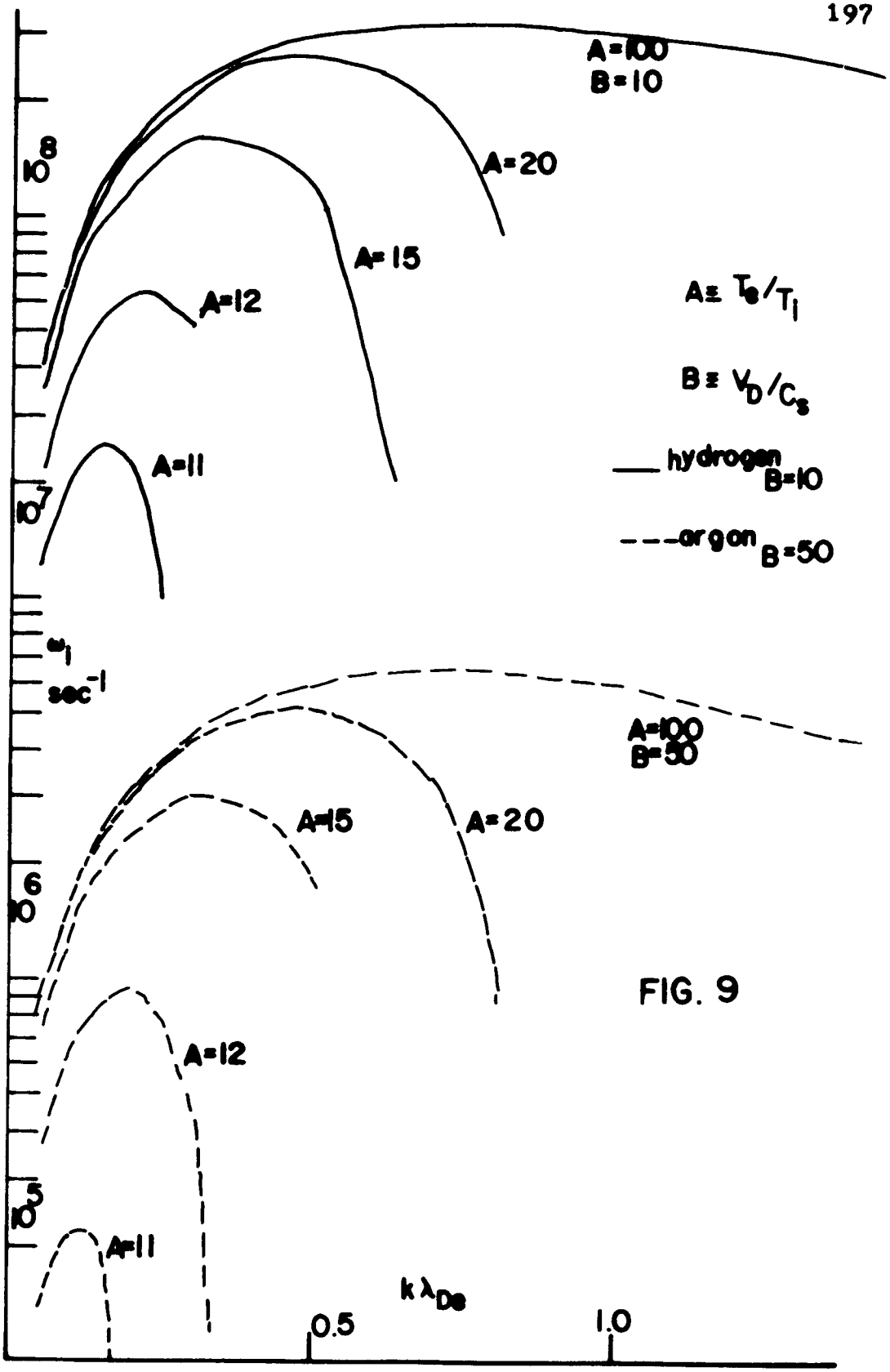
A=100
B=10
A=20
A=15
A=12
A=11
A≡ T_e/T_i
B≡ V_D/C_s
hydrogen B=10
argon B=50
10^8
10^7
ω_i
sec^{-1}
A=100
B=50
A=15
A=20
10^6
A=12
10^5
A=11
$k\lambda_{De}$
0.5
1.0

FIG. 9

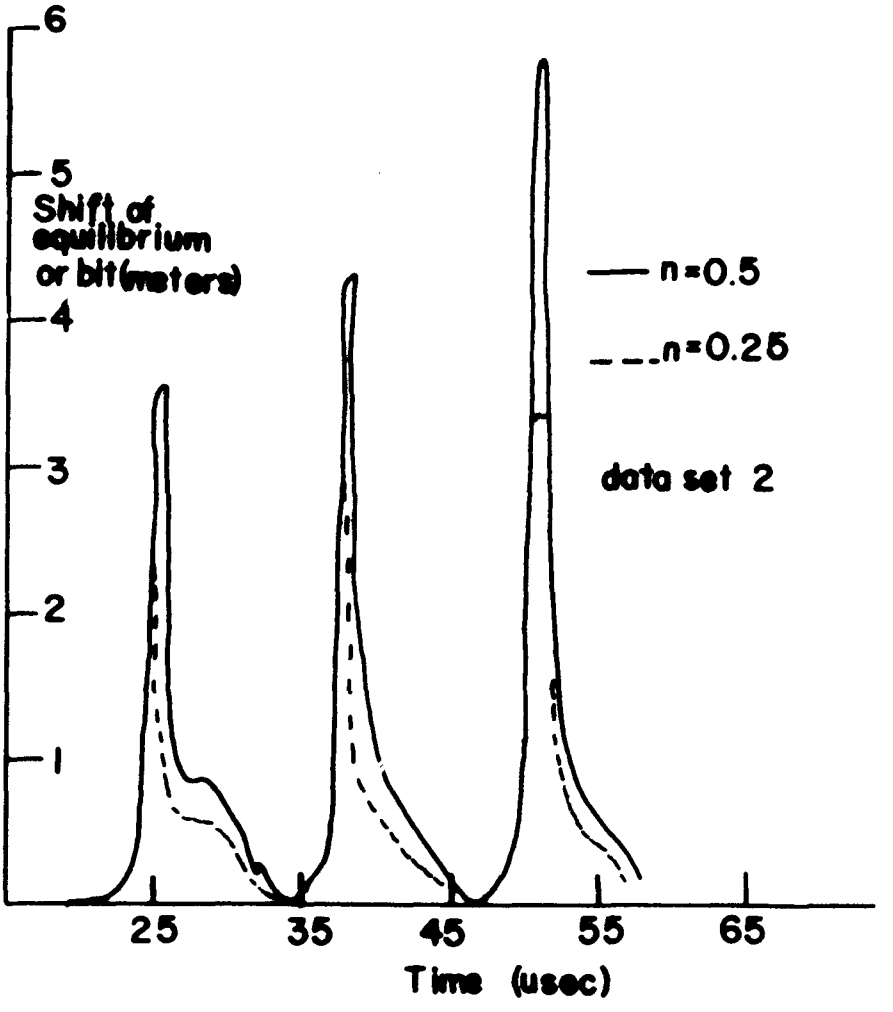
6
5
Shift of equilibrium or bit(meters)
4
3
2
1
n=0.5
n=0.25
data set 2
25
35
45
55
65
Time (usec)

FIG. 10

CHAPTER VIII

REFERENCES

1. K. Nishikawa and C. S. Wu, Physical Review Letters 23, 1020 (1969).
2. G. Bateman, Physical Review Letters 29,1499 (1972).
3. H. Dreicer, Physical Review 117, 343 (1960).
4. S. M. Hamberger and J. Jancarik, The Physics of Fluids 15, 825 (1972).
5. D. W. A. Whitfield and H. M. Skarsgard, The Physics of Fluids 17, 2255 (1974).
6. A. Hirose and I. Alexeff, Physical Review Letters 26, 949 (1971).

CHAPTER IX

CONCLUSION

In conclusion, this thesis has discussed various experimental and theoretical aspects of plasma resistivity and runaway electrons in a magnetized toroidal plasma.

The existence of runaway electrons has been showr by the observed agreement between the measured X-ray energy, 75Kev, and the energy predicted for freely accelerated electrons, 79Kev. These X-rays are produced when the runaway electron beam hits the vacuum wall. The X-ray emission time, t_x , observed in argon discharges during the first acceleration cycle has been found to have the following dependence on the external betatron electric field,

$$t_x = \kappa E_\phi^{-n} \qquad \text{where} \quad n \simeq 1.0 \pm 0.1$$

and independent of B_ϕ .

This is consistent with the dependence predicted by the resistive current instability. The fact that X-rays are not detected in cycles other than the first cycle in argon is also consistant with the resistive current instability. Similarly, detection of X-rays in hydrogen occurs only in cycles other than the first, when the conduction current is small enough. This is also consistent with the resistive

current effect. This follows from the fact that the equilibrium orbit is shifted outside of the vacuum chamber when the current is large enough. The time it takes for the runaway electrons to drift to the vacuum chamber wall is short enough so that the X-ray energy is too low to be detected with our experimental apparatus.

The observed plasma electrical conductivity was found to be two orders of magnitude lower then predicted by the classical $T^{3/2}$ law obtained from a Fokker-Planck calculation. For the measured temperature of 14ev a conductivity of 6.9×10^{14}esu is calculated while in hydrogen a value of about 6×10^{12}esu is measured. For the measured values of the drift velocity and ion acoustic speed a value of $T_e/T_i \geq 10$ the linear theory of ion acoustic wave instability is applicable. For $T_e/T_i \cong 11$ the value of $k\lambda_D = 0.2$ gives the highest growth rate of ion acoustic waves in hydrogen. The growth period is 0.25 usec. Using Dupree's theory of anomalous conductivity gives the measured value of the conductivity. Calculations for argon yield similar results except that the growth time is 28 usec. It is not clear what this discrepency is due to, though the inclusion of electron trapping in the calculations may shorten the growth time for argon.

Using single and multiple coil probes, the plasma column

center was observed to probably have a kink structure. This is consistant with the fact that the measured q value is less than 1 for the particular discharge studied.

The observed conduction current has a characteristic non-linear wave form. This becomes particularly evident at low neutral density, low current discharges in hydrogen. The origin of this effect may be related to particle trapping in the azimuthal magnetic field. Different conduction current models were studied to try to predict this non-linear feature. A linear circuit model of the plasma betatron gave good order of magnitude agreement between the high current hydrogen discharge, which is the most linear in appearance. By matching the measured phase shift between the current maximum and electric field maximum and the measured current amplitude to calculated current forms, the electron temperature and plasma column size could be estimated. For a hydrogen discharge of peak current of 2500 amperes in the third acceleration cycle, the calculated plasma temperature is 11ev and the claculated plasma column diameter is 1.7cm. This is close to what has been measured experimentally (14ev and 1.0to 4.0cm). For the argon and hydrogen wave forms of lower current, and also noticeably greater non-linear appearance, the linear model gives values which are orders of magnitude in disagreement with

measured temperature and column size. A phenomenological model, however, using a non-linear resistance has been used to qualitatively reproduce the observed non-linear wave forms in the discharges observed.

The ionization by freely accelerated electrons has been studied theoretically. It is shown that the ionization is typically rapid for neutral densities of $1 \times 10^{13} cc^{-1}$ and initial runaway densities of 10^{3} cc^{-1} or higher. Using the ionization model the net current produced by the runaways is computed and the observance of current peaks for different values of applied electric field and azimuthal magnetic field is studied. For the parameter range used it was found that the maximum current amplitude is independent of E_ϕ, to within $\pm$ 10 percent, for E_ϕ = 1 to 20 v/cm.

In order to further explore the runaway phenomena, additional measurements, in hydrogen discharges, of the disruption time and X-ray energy are needed. The existence of soft X-rays and the measurement of their energies during high current acceleration cycles would support the idea that the resistive current effect is responsible for beam disruption in these conditions. Measurements of plasma density during these cycles is also important in order to determine the critical field strength during these cycles. A higher frequency microwave interferometer is needed for

this pupose. The effect of changing the vector potential shape is also of interest and can be easily studied by changing the size of the small correction coils on the betatron field coil leads.

The apparant kink structure can be further explored by changing the total current flow such that $q > 1$ and repeating the multiple probe measurements. Also, magnetic field probes at different azimuthal positions can help in distinguishing between a kink structure or motion of the plasma column.